

## TOPICAL REVIEW

## Nuclear rainbow scattering and nucleus-nucleus potential

Dao T Khoa<sup>†§</sup> W von Oertzen<sup>†‡</sup> H G Bohlen<sup>†</sup> and S Ohkubo<sup>¶</sup><sup>†</sup> Hahn-Meitner-Institut Berlin, Glienicker Str.100, D-14109 Berlin, Germany<sup>§</sup> Institute for Nuclear Science and Technique, VAEC, P.O. Box 5T-160, Nghia Do, Hanoi, Vietnam<sup>‡</sup> Freie Universität Berlin, Fachbereich Physik, Berlin, Germany<sup>¶</sup> Department of Applied Science and Environment, Kochi Women's University, Kochi 780-8515, Japan

E-mail: khoa@vaec.gov.vn, oertzen@hmi.de, bohlen@hmi.de, shigeo@cc.kochi-wu.ac.jp

**Abstract.** Elastic scattering of  $\alpha$ -particle and some tightly-bound light nuclei has shown the pattern of *rainbow scattering* at medium energies, which is due to the *refraction* of the incident wave by a strongly attractive nucleus-nucleus potential. This review gives an introduction to the physics of the nuclear rainbow based essentially on the optical model description of the elastic scattering. Since the realistic nucleus-nucleus optical potential (OP) is the key to explore this interesting process, an overview of the main methods used to determine the nucleus-nucleus OP is presented. Given the fact that the absorption in a rainbow system is much weaker than that usually observed in elastic heavy-ion scattering, the observed rainbow patterns were shown to be linked directly to the density overlap of the two nuclei penetrating each other in the elastic channel, with a total density reaching up to twice the nuclear matter saturation density  $\rho_0$ . For the calculation of the nucleus-nucleus OP in the double-folding model, a realistic density dependence has been introduced into the effective M3Y interaction which is based originally on the G-matrix elements of the Reid- and Paris nucleon-nucleon (NN) potentials. Most of the elastic rainbow scattering data were found to be best described by a *deep* real OP like the folded potential given by this density dependent M3Y interaction. Within the Hartree-Fock formalism, the same NN interaction gives consistently a *soft* equation of state of cold nuclear matter which has an incompressibility constant  $K \approx 230 - 260$  MeV. Our folding analysis of numerous rainbow systems has shown that the elastic  $\alpha$ -nucleus and nucleus-nucleus refractive rainbow scattering is indeed a very helpful experiment for the determination of the realistic  $K$  value. The refractive rainbow-like structures observed in other quasi-elastic scattering reactions have also been discussed. Some evidences for the refractive effect in the elastic scattering of unstable nuclei are presented and perspectives for the future studies are discussed.

## 1. Introduction

### 1.1. Atmospheric Rainbow

The commonly known atmospheric rainbow is observed whenever there are water droplets illuminated by the sun light. It can be seen during the rain with the sunshine not completely covered by the clouds (see Fig. 1) or from a fountain, when the sunlight enters from behind the point of observation. Besides the fascinating effect of colour splitting due to the dependence of the refraction on the wavelength, the more interesting physics effect is the *increased* light intensity around the rainbow angle  $\Theta_R$  and the *shadow*-region lying beyond  $\Theta_R$ .

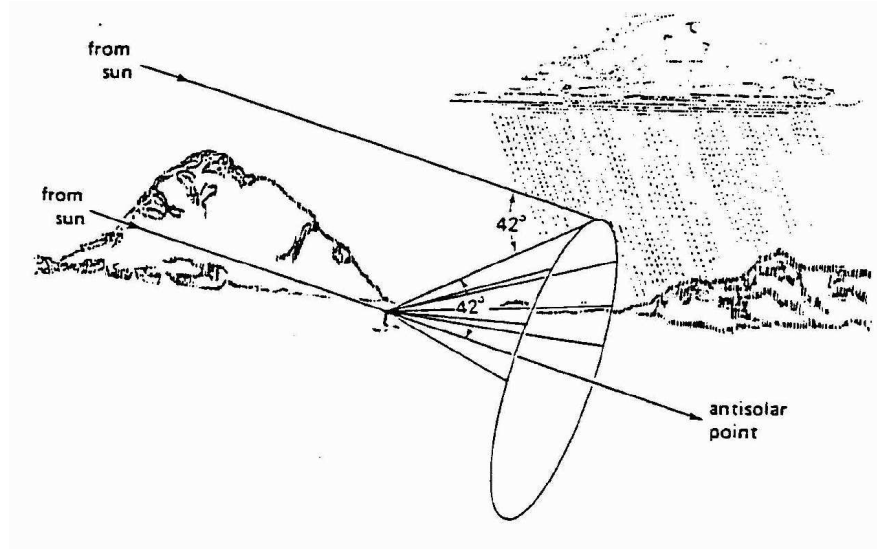


**Figure 1.** Descartes traced the light ray reflected from a uniform rain drop and found a “critical” ray which has a minimal deflection angle of about  $138^\circ$ , whose supplementary  $\Theta_R \simeq 42^\circ$  is the largest and known nowadays as the “rainbow” angle. The atmospheric rainbow is produced by the piling up of the light rays near  $\Theta_R$  which is slightly larger than  $42^\circ$  for red light and smaller for blue, and hence the colour splitting of the “white” sunlight. Illustration taken from Ref. [1].

The first modern explanation of the atmospheric rainbow was given by Descartes in 1637 in his book “Les Meteores”. An illustration of the atmospheric rainbow according to Descartes’ interpretation is shown in Fig. 1. Historically, Noah (Genesis 9:13 “*I have set my rainbow in the clouds, and it will be the sign of convening between me and earth*”), and his family can be identified as the first “recorded” observers of the rainbow, since the person speaking in singular “I” should have known the rainbow well before. Since Descartes’ time up to the present, the physics of the atmospheric rainbow has been described by different models, ranging from a simple classical geometrical ray optics to the quantum mechanical complex angular momentum theory for the scattering of electromagnetic waves [2, 3] with higher and higher mathematical sophistication. For interested readers there exists in the literature a number of excellent monographs

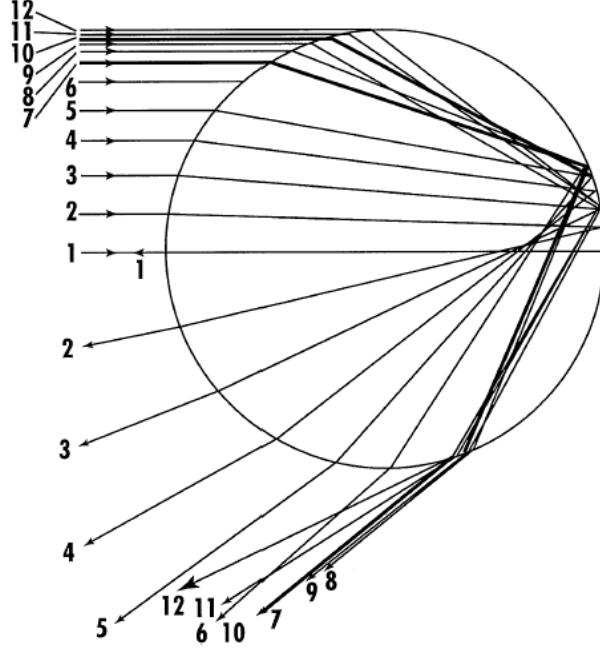


**Figure 2.** The paths of light rays entering a spherical water drop at different impact parameters and leaving it after a refraction - reflection - refraction sequence. The ray numbered 7 is the rainbow ray, at which light is deflected to a maximal (negative) scattering angle of around  $42^\circ$ . Illustration taken from Ref. [3].

and reviews on the physics of the atmospheric rainbow, like the book by Greenler on rainbows, halos and glories [1] or the review articles by Nussenzweig [2] and Adam [3]. Especially, one can learn in the latter about all the main physical and mathematical approaches used so far to study the physics of the atmospheric rainbow. Educational information about the atmospheric rainbow is also available in the internet (see, e.g., <http://www.meteoros.de/rainbow/rainbow.htm>). In our topical review we do not attempt to cover all this development, but will concentrate on the interference pattern of the refractive nucleus-nucleus scattering which gives rise to the nuclear rainbow. Note that the rainbow-like interference pattern has been observed also in molecular and atomic scattering [4].

The light focusing near the rainbow angle, as a result of a refraction - reflection - refraction process by the light rays in a spherical water drop, is illustrated in Fig. 2. The first refraction occurs when the light enters the water drop, the refracted light undergoes then a reflection and is refracted again before leaving the drop. One can see in Fig. 2 an interesting variation of the “deflection angle” as function of the impact parameter  $b$ , from the “head-on” ray with a maximal deflection at  $180^\circ$  to the “rainbow” ray with a minimal deflection at about  $138^\circ$ . For further discussion, it is convenient that we discuss this refraction - reflection process in terms of negative deflection  $\Theta$  of the light ray, i.e., the supplementary of the deflection angle so that the rainbow ray is deflected at  $\Theta_R \simeq 42^\circ$ .

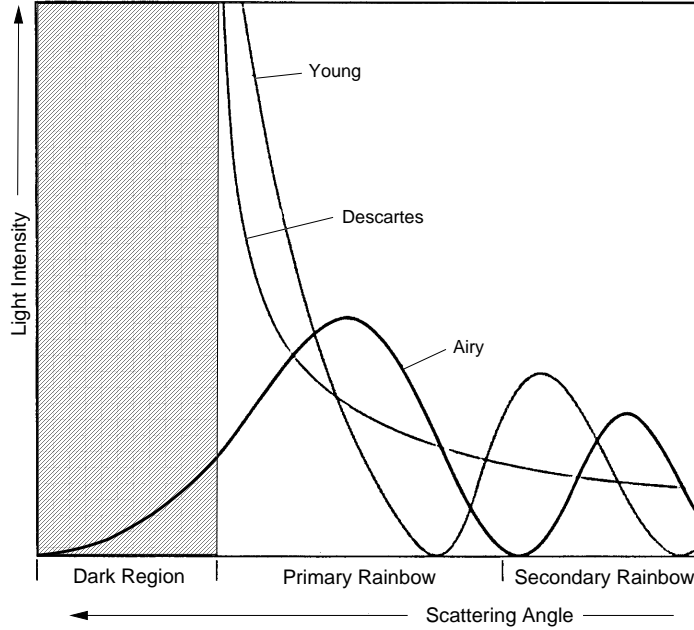


**Figure 3.** Different descriptions of the light intensity of the atmospheric rainbow. While the “classical” solutions by Descartes, Newton and Young give a divergence at the rainbow angle, Airy’s description shows clearly the wave nature of light which penetrates also into the shadow region beyond the rainbow angle. The rainbow structure inside the main rainbow, see Fig. 5, is due to the second order Airy structure.

The interesting physics effect here is the enhanced light intensity (concentration of many light rays, e.g., those numbered 6 to 12 in Fig. 2) near the rainbow angle  $\Theta_R$ , which is followed by a “shadow” region. Classically [5], this shadow is produced by the maximum of the deflection function  $\Theta(b)$  because the intensity (or in our cases: cross section  $\frac{d\sigma}{d\Omega}$ ) of the scattered light is proportional to the inverse of the first derivative of  $\Theta(b)$ , as can be seen in the following expression

$$\frac{d\sigma}{d\Omega} = \sum_b \frac{b}{\sin \Theta(b) |d\Theta(b)/db|}. \quad (1)$$

Here the sum is taken over the light rays entering the water drop at different impact parameters  $b$ , some of them scatter to the same angle  $\Theta$ , like those numbered 7, 8 and 9 in Fig. 2, with the maximal (negative) deflection occurring near the rainbow angle  $\Theta_R$ . This simple expression of light intensity has a *divergence* at  $\Theta_R$  (with  $d\Theta(b)/db=0$ ), which is also known as a caustic in optics. The existence of the divergence of the light intensity at the rainbow angle could not be remedied in both the Descartes’ theory and the more advanced version of ray optics by Newton and Young (see Fig. 3). Moreover, the observation of the supernumerary bows inside the primary rainbow (see Fig. 5 below) persistently pointed to the inadequacy of Descartes’ and Newton’s models which could not explain the origin of the supernumeraries. All this remained a mathematical challenge until Airy, in the 19-th century, provided the first mathematical model of the rainbow based on the light wave diffraction and interference [6].

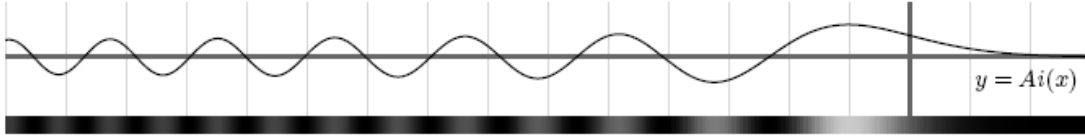


**Figure 4.** Graph of the Airy rainbow integral  $Ai(x)$ . The argument  $x$  is proportional to  $\Theta - \Theta_R$  so that  $x = 0$  corresponds to  $\Theta = \Theta_R$  and positive  $x$  is on the dark side of the rainbow. Below, according to Airy’s theory, illumination is proportional to  $Ai(x)^2$  which gives rise to the *primary* bow along with several *supernumerary* bows. Illustration taken from Ref. [3].

By using the standard Huygens’ concept of the light wavefront rather than the optical light rays, Airy has shown the self-interference of such a wavefront as it becomes folded onto itself during the refraction and reflection within the rain drop. As a result, the primary rainbow is the first interference maximum, the second and third maxima being the first and second supernumerary bows, respectively. Airy described the local intensity of scattered light wave with the help of a “rainbow integral”, which is now known as the Airy function  $Ai(x)$  (see Fig. 4). Airy’s model not only removed the divergence of the light intensity at the rainbow angle as shown in Fig. 3, but also explained successfully the existence of the supernumerary bows which appear naturally as the maxima of  $Ai(x)$ . Although more precise and sophisticated mathematical physics approaches to describe the atmospheric rainbow have been developed later in the 20-th century [2, 3], Airy’s model remains a simple but very realistic approximate description of the rainbow pattern, which has been used widely to identify the rainbow features observed in molecular, atomic and nuclear scattering [4, 5].

### 1.2. Nuclear Rainbow

Nuclei are known to have wave properties and they can be diffracted, refracted and suffer interference just like the sun light. Consequently, the nucleus-nucleus scattering may also display rainbow features depending on the scattering conditions and binding structure of the projectile and target. In terms of the wave scattering theory, if the scattering proceeds only elastically the total flux would remain unchanged. Therefore, the nuclear rainbow should be strongest in the elastic scattering channel if a system with small absorption is chosen. Indeed, the nuclear rainbow pattern has been first observed during the 70’s of the last century in the elastic  $\alpha$ -nucleus scattering [8, 9, 10], and later on in the elastic scattering measured for some strongly bound light heavy-ion systems like  $^{12}\text{C}+^{12}\text{C}$  [11, 12, 13] or  $^{16}\text{O}+^{16}\text{O}$  [14, 15, 16]. For these systems the absorption due to nuclear reactions was sufficiently low for the rainbow effect to appear. The concept of the wave *refraction* implies that the wavelength changes whenever the wave penetrates from one medium into another. In a realistic case of the elastic nucleus-

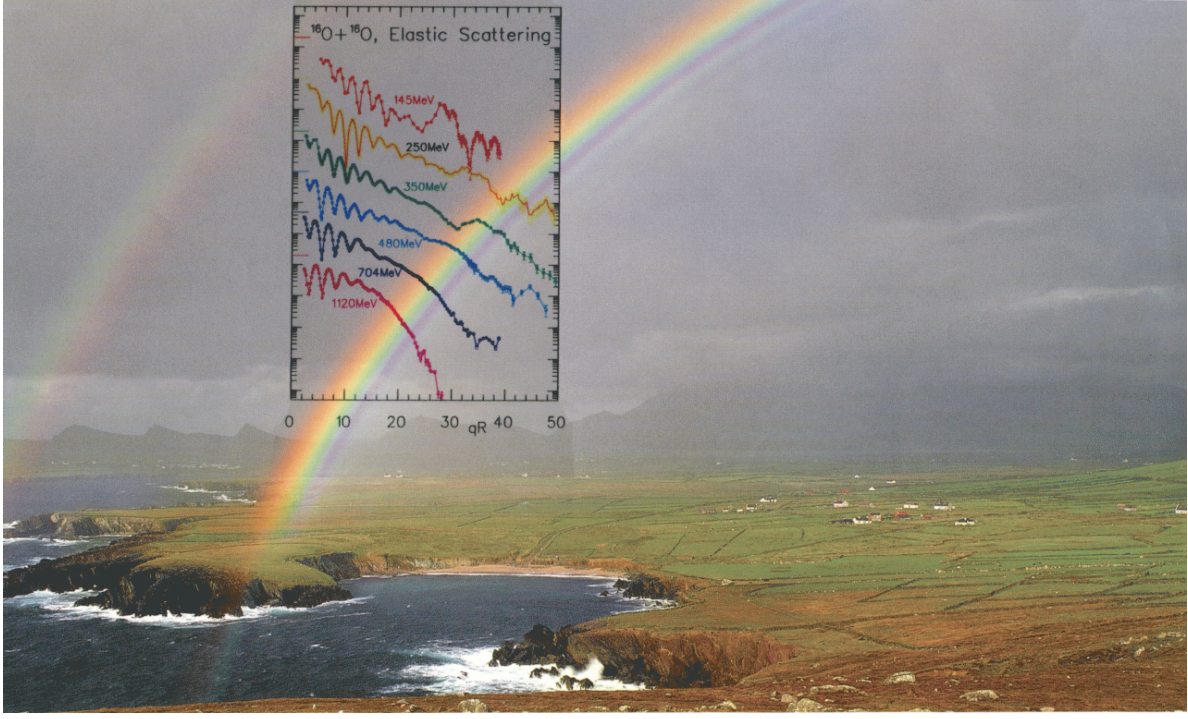


**Figure 5.** Photographic image of the atmospheric rainbow where both the primary and secondary rainbows can be seen. The faint bows located inside the primary rainbow are the supernumeraries which were first explained in 1838 by Airy [6]. The secondary rainbow is formed by light rays undergoing a second reflection in the rain drops and hence is fainter and has a reversed sequence of colours. The inset along the primary bow shows the elastic  $^{16}\text{O} + ^{16}\text{O}$  scattering data (plotted as function of momentum transfer) measured at different laboratory energies, where the most pronounced rainbow pattern associated with the first Airy maximum has been observed at 350 MeV. At lower energies the secondary Airy maximum was also observed. The rainbow angle  $\Theta_R$  found for the elastic  $^{16}\text{O} + ^{16}\text{O}$  scattering, at energies of 250 to 1120 MeV, is located near the maximum of the light intensity in the atmospheric rainbow. Illustration taken from Ref. [7].

nucleus scattering, the de Broglie wavelength  $\lambda_B$  of the scattered wave is changed as the projectile penetrates the target nucleus at the internuclear distance  $R$ . There, the strong projectile-target interaction occurs, due to the local strength  $V(R)$  of the (real) nucleus-nucleus optical potential (OP), and the wavelength  $\lambda_B(R)$  is determined as

$$\lambda_B(R) = h / \sqrt{2\mu[E - V(R)]}, \quad (2)$$

where  $E$  is the centre-of-mass energy of the scattering system,  $\mu$  is the reduced mass. It is obvious that the nuclear OP, used in the optical model (OM) calculation to describe the nucleus-nucleus elastic scattering, is the most important physics input in the study of nuclear rainbow scattering. We further determine the quantal analog of the index of

refraction  $n(R)$  for nuclear scattering in the same way as in the classical optics (ratio of the velocity of the scattered wave to that of free wave) as

$$n(R) = \sqrt{1 - V(R)/E}. \quad (3)$$

The refractive index is larger unity ( $n > 1$ ), because the potentials are attractive ( $V(R) < 0$ ), and can reach values well above 2 at low energies. The big difference between the index of refraction used in the classical optics and its quantal counterpart (3) is that the latter is not uniformly constant but depends on the strength of the OP at given interaction distance  $R$ . This is the main reason, why the nuclear rainbow is much more difficult to observe and to identify. It also becomes clear from Eqs. (2) and (3) that the nuclear rainbow can only be properly analyzed and identified based on a correct choice of the nuclear OP. The nucleus-nucleus OP is, therefore, the key physics quantity being discussed throughout this topical review.

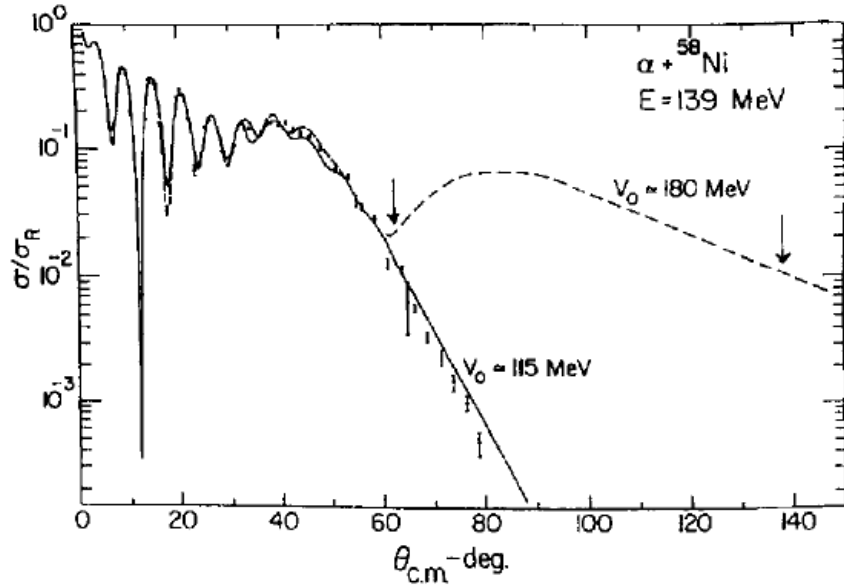


**Figure 6.** Elastic  $\alpha + {}^{58}\text{Ni}$  scattering data at  $E_{\text{lab}} = 139$  MeV [9] and the OM descriptions given by two different choices of the real OP of Woods-Saxon shape (with the depths  $V_0$  indicated) which give the rainbow angle of  $\Theta_R \approx 61^\circ$  and  $139^\circ$ , respectively. Illustration taken from Ref. [5].

As already mentioned, the first observation of nuclear rainbow was made some 30 years ago by Goldberg *et al.* [8, 9, 10] in their experiments on elastic  $\alpha$ -nucleus scattering at  $E_{\text{lab}} \approx 140$  MeV (see Fig. 6). They have found that a strong and broad maximum of the elastic cross section at large scattering angles is of refractive nature, and thus can be identified as a nuclear rainbow [17]. Moreover, the most significant

physics effect established by these first experiments on the nuclear rainbow is that the extension of the elastic scattering data well beyond the rainbow angle  $\Theta_R$  (marked in Fig. 6 by the first arrow) allowed the elimination of discrete ambiguities in the depth of the  $\alpha$ -nucleus OP. In the  $\alpha+^{58}\text{Ni}$  case, the data up to  $\Theta \approx 60^\circ$  could be described by a number of Woods-Saxon (WS) shaped potentials with discretely different central depth parameters  $V_0$  of the real OP. The observation of the exponential fall-off of the rainbow maximum well beyond  $60^\circ$  allowed the unique selection of  $V_0 = 115$  MeV for the depth of the potential as the most appropriate one.

Consequently, extracting important information about the nucleus-nucleus OP at short distances and, hence, testing the validity of different theoretical models of the nucleus-nucleus OP has always been one of the main goals of numerous experimental and theoretical studies of the nuclear rainbow during the last three decades.

## 2. Rainbows in the elastic nucleus-nucleus scattering

### 2.1. Hindrance by a strong absorption

In general, the elastic nucleus-nucleus scattering is associated with a strong absorption, i.e., the partial loss of the incident wave from the elastic scattering channel into various non-elastic reaction channels during the nucleus-nucleus collision. As a result, the nucleus-nucleus or heavy-ion (HI) optical potential always has an imaginary part,  $W$ , which describes the absorption from the elastic channel. This absorption can suppress significantly the refractive structure of the elastic scattering and no rainbow-like effect has been observed in strongly absorbing HI systems. Since the total optical potential (denoted hereafter as  $U$ ) is complex,  $U = V + iW$ , with the real part  $V$  describing elastic scattering and the imaginary part  $W$  describing absorption, we can draw an analogy between the nuclear absorption and the absorption of light by a cloudy crystal ball using a complex index of refraction. It is natural that the stronger the absorption, the smaller the chance to observe the rainbow pattern. Due to the strong absorption, most of the elastic HI scattering is dominated by the surface scattering and the information about the nucleus-nucleus interaction is obtained for peripheral trajectories only. Here, the term “surface” means the region where the nuclear forces begin to act strongly [5]. The location of this surface region can be represented by a strong absorption radius  $R_{\text{sa}}$  which can be identified with the apsidal distance on a Rutherford orbit with the same angular momentum as that for which the transmission coefficient is one-half. In terms of the distance between the centres of the two colliding nuclei with mass numbers  $A_1$  and  $A_2$ ,  $R_{\text{sa}}$  can be parameterized [5] as

$$R_{\text{sa}} = r_0(A_1^{1/3} + A_2^{1/3}) + \Delta. \quad (4)$$

Since  $r_0 \approx 1.1$  fm, the first term represents the sum of the radii of the density distributions of the two nuclei and the second term  $\Delta$  is the separation of their surfaces. Values of  $\Delta$  between 2 and 3 fm are typical separations at energies of 10 to 20 MeV/nucleon. The value of the radius  $R_{\text{sa}}$ , and hence the separation  $\Delta$ , decreases



slowly as the energy increases [19, 20] ( $\Delta$  has reduced to values of 1-2 fm at energies around 100 MeV/nucleon). Thus, a strong absorption usually takes place well before there is any substantial overlap of the two nuclear density distributions. The strong absorption makes it difficult or impossible to gain any information on the nucleus-nucleus OP at short distances, where the two nuclei begin to overlap appreciably. This situation is typical for most of the HI elastic scattering systems [21], especially those involving medium to heavy nuclei.

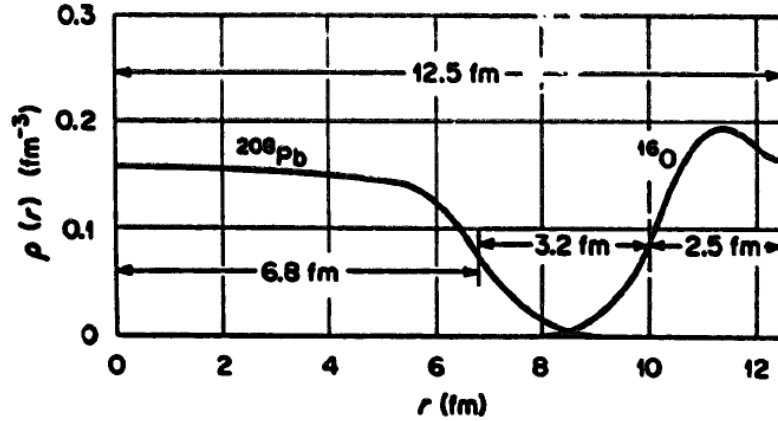


**Figure 7.** The densities of the nuclei  $^{16}\text{O}$  and  $^{208}\text{Pb}$  when their centres are separated by the strong absorption radius  $R_{\text{sa}}$  deduced for the elastic scattering at incident energies of 100 - 200 MeV. Illustration taken from Ref. [21].

In a semiclassical representation, as soon as a nucleus-nucleus collision occurs, the composite projectile will induce various (inelastic) reactions and “dissolve like a piece of salt (or sugar) in water”. The reaction rates depend on the “chemical potentials” of the interacting systems. These non-elastic reaction channels give rise to the imaginary part  $W$  of the nucleus-nucleus OP. The mean free path  $\lambda_{\text{mfp}}$  for the penetration of the projectile into the target can be determined in the WKB approximation [18] as

$$\lambda_{\text{mfp}}(R) = \frac{h}{\sqrt{\mu}} \frac{\sqrt{2[E - V(R)]}}{|W(R)|} = v(R)\tau(R), \quad (5)$$

where  $v(R)$  is the projectile velocity and  $\tau(R)$  is the average life time of the projectile in the nuclear medium (the average time until a nuclear reaction occurs which changes the ground-state structure of the projectile and/or target). As an example,  $\lambda_{\text{mfp}}(R)$  values determined for the elastic  $^{16}\text{O}+^{16}\text{O}$  scattering at 350 MeV are shown in lower part of Fig. 8.

Let us consider now the quantum mechanical expansion of the elastic nucleus-nucleus scattering amplitude into a partial-wave series [22]

$$f(\Theta) = f_{\text{C}}(\Theta) + \frac{i}{2k} \sum_l (2l+1) \exp(2i\sigma_l) (1 - S_l) P_l(\cos \Theta), \quad (6)$$

where  $f_C(\Theta)$  is the amplitude of the Coulomb scattering,  $\sigma_l$  - the Coulomb phase shift,  $k$  - the wave number,  $S_l$  - the scattering matrix element for the  $l$ -th partial wave, and  $P_l(\cos \Theta)$  - the Legendre polynomial. In such a representation, the magnitude of  $|S_l|$  gives us the measure of the absorption strength at a given impact parameter or internuclear distance  $R \approx (l + 1/2)\hbar/k$ . For a strong absorbing HI system one usually has  $|S_l| \leq 10^{-4}$  for  $l < l_g \approx kR_g$ , where  $R_g$  is the critical or grazing distance at which the colliding pair begin to experience the strong nuclear interaction acting between them. Then, the transmission coefficient  $T_l = 1 - |S_l|^2$  is close to zero and represents complete absorption to within  $10^{-8}$  [5].

## 2.2. Incomplete absorption and the rise of the nuclear rainbow

The situation is, however, different for  $\alpha$ -nucleus and light HI systems consisting of strongly bound nuclei, where the refractive or rainbow pattern has been observed. In such a case, due to a weaker absorption in the nucleus-nucleus system, one can observe elastic scattering events occurring at sub-surface distances (with  $l < l_g$ ). The elastic cross section is larger at large scattering angles and carries information on the nucleus-nucleus OP at smaller partial waves or shorter distances. To illustrate this effect, we have plotted in Fig. 8 the mean free path  $\lambda_{\text{mfp}}$  for the  $^{16}\text{O}+^{16}\text{O}$  system, using a best-fit complex OP which reproduces the rainbow pattern observed at  $E_{\text{lab}} = 350$  MeV [14]. One can see that  $\lambda_{\text{mfp}}$  is reduced to its (asymptotic) minimal value at  $R \leq 5$  fm. This distance is significantly smaller than the strong absorption radius  $R_{\text{sa}} \approx 7 - 8$  fm as given by the global systematics (4) from Ref. [5], and the measured elastic  $^{16}\text{O}+^{16}\text{O}$  data [14] at this energy also have one of the most pronounced rainbow pattern ever observed in HI elastic scattering. The elastic  $^{16}\text{O}+^{16}\text{O}$  data at 350 MeV and those at lower energies show consistently a well defined Airy pattern which is very helpful in reducing the ambiguity of the shape and depth of the OP [23, 24].

In the semiclassical representation, a weak absorption allows us to keep the underlying trajectory picture for the scattering system. Fig. 9 illustrates some typical trajectories for the elastic wave scattered by an attractive nuclear potential plus a repulsive Coulomb potential. The scattering angle as a function of impact parameter  $R$ , or angular momentum  $(l + 1/2)\hbar = kR$ , is called the *deflection function*  $\Theta(l)$  and is shown on the right part of Fig. 9. In the semiclassical or WKB approximation, the deflection function is expressed through the real scattering phase shifts  $\delta(l)$  as

$$\Theta(l) = 2 \frac{d\delta(l)}{dl}. \quad (7)$$

The most important contribution by Airy was to show, that the atmospheric rainbow originates from the extremum of the deflection function of the scattered light wave. In a complete (optical) analogy for the nucleus-nucleus scattering, the two extrema of  $\Theta(l)$  shown in Fig. 9 can be identified as the Coulomb and nuclear rainbow angles, respectively. While the Coulomb rainbow is well described by the known nuclear potential at the surface and the Coulomb interaction between the two ions, the nuclear

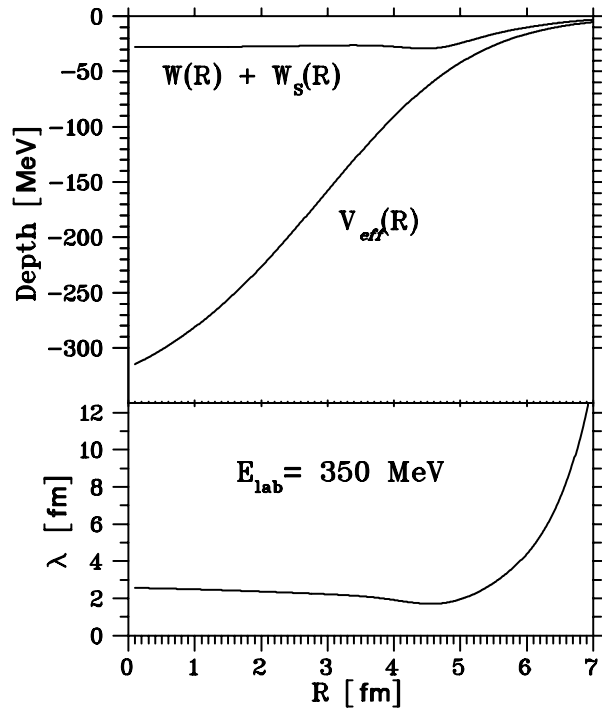


**Figure 8.** Upper part: Real ( $V$ ) and imaginary ( $W$ ) parts of the  $^{16}\text{O}+^{16}\text{O}$  optical potential obtained from the OM fit to the elastic  $^{16}\text{O}+^{16}\text{O}$  scattering at  $E_{\text{lab}} = 350$  MeV. Lower part: The mean free path  $\lambda_{\text{mfp}}$ , obtained from Eq. (5) with this complex OP, versus the distance  $R$  between the centres of the two  $^{16}\text{O}$  nuclei.

rainbow can only be properly identified and described based on a realistic choice for the nuclear part of the nucleus-nucleus OP. Our further consideration is, therefore, concentrated on the nuclear rainbow which can provide us with some information about the hadronic interaction between the two colliding nuclei. In Fig. 9, the peripheral trajectories with positive  $\Theta$ , which are dominated by the Coulomb repulsion, contribute mainly to the *nearside* scattering, while those drawn to negative angles  $\Theta$  (dominated by the attractive nuclear potential) represent the *farside* scattering. Thus, the more pronounced the nuclear rainbow, the stronger the farside scattering and the more information about the nucleus-nucleus OP can be deduced from the OM analysis of the elastic scattering. If the scattering conditions (incident energy, absorption...) are appropriate, the Airy pattern of the supernumeraries shown in Fig. 4 for the atmospheric rainbow can also be present in the pattern of the nuclear rainbow. Namely, the Airy oscillation pattern is observed in the farside scattering cross section as a result of the interference between the two branches (specified below as  $l_<$  and  $l_>$ ) of the deflection function on either side of its minimum at  $\Theta_R$ .

### 2.3. The farside scattering and the Airy oscillation pattern

To understand the structure of the Airy supernumeraries (or Airy oscillations) of the nuclear rainbow pattern, it is necessary to consider explicitly the contributions from the

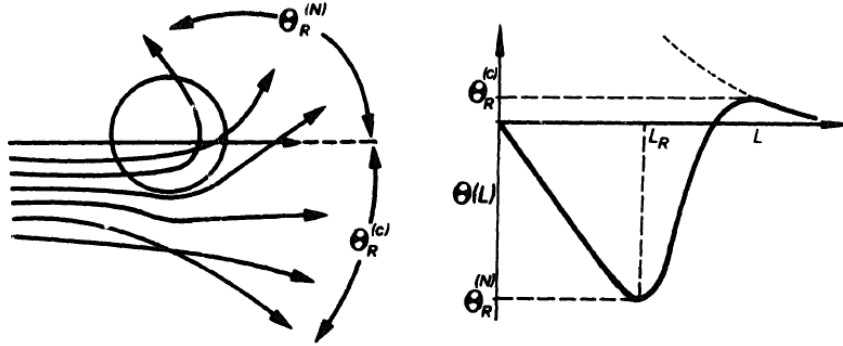


**Figure 9.** Left: Classical trajectories of the nuclear wave scattered elastically by a short-range attractive nuclear potential and a long-range repulsive Coulomb potential which lead to the nuclear (N) and Coulomb (C) rainbows, respectively. Right: The corresponding deflection function. Illustration taken from Ref. [25].

nearside and farside scattering trajectories shown in Fig. 9. For a strongly refractive (weakly absorptive) nucleus-nucleus system, the amplitudes of the nearside and farside scattering can be determined from a nearside/farside decomposition of the elastic scattering amplitude, a method developed by Fuller [26]. Namely, by decomposing the Legendre function  $P_l(\cos \Theta)$  into waves travelling in  $\Theta$  which are running in opposite directions around the scattering centre, the nuclear part of the scattering amplitude (6) can be decomposed into the nearside ( $f_N$ ) and farside ( $f_F$ ) components as

$$f_N(\Theta) + f_F(\Theta) = \frac{i}{2k} \sum_l (2l+1) A_l \left[ \tilde{Q}_l^{(-)}(\cos \Theta) + \tilde{Q}_l^{(+)}(\cos \Theta) \right], \quad (8)$$

$$\text{where } \tilde{Q}_l^{(\mp)}(\cos \Theta) = \frac{1}{2} \left[ P_l(\cos \Theta) \pm \frac{2i}{\pi} Q_l(\cos \Theta) \right], \quad (9)$$

and  $Q_l(\cos \Theta)$  are the Legendre functions of the second kind. The nearside amplitude  $f_N(\Theta)$  represents contributions from waves deflected to the direction of  $\Theta$  on the near side of the scattering centre and the farside amplitude  $f_F(\Theta)$  represents contributions from waves travelling from the opposite (far) side of the scattering centre to the same angle  $\Theta$ . The nearside/farside decomposition of the Rutherford amplitude can be obtained analytically [26] using the explicit form of  $f_C(\Theta)$  (available from, e.g., Ref. [22]). Note that Fuller's method of nearside/farside decomposition has been recently improved by Anni *et al.* [27] to underline the refractive nature of the elastic scattering cross section in the nuclear rainbow cases. In terms of scattering trajectories shown in Fig. 9, the real nucleus-nucleus OP has the refractive effect of a converging lens [28], so that for a 'detector' located at angle  $\Theta$  it pulls the nearside trajectories towards the forward direction and the farside trajectories away from it. The nuclear rainbow pattern is produced exclusively by the farside trajectories which are governed by the strong nuclear

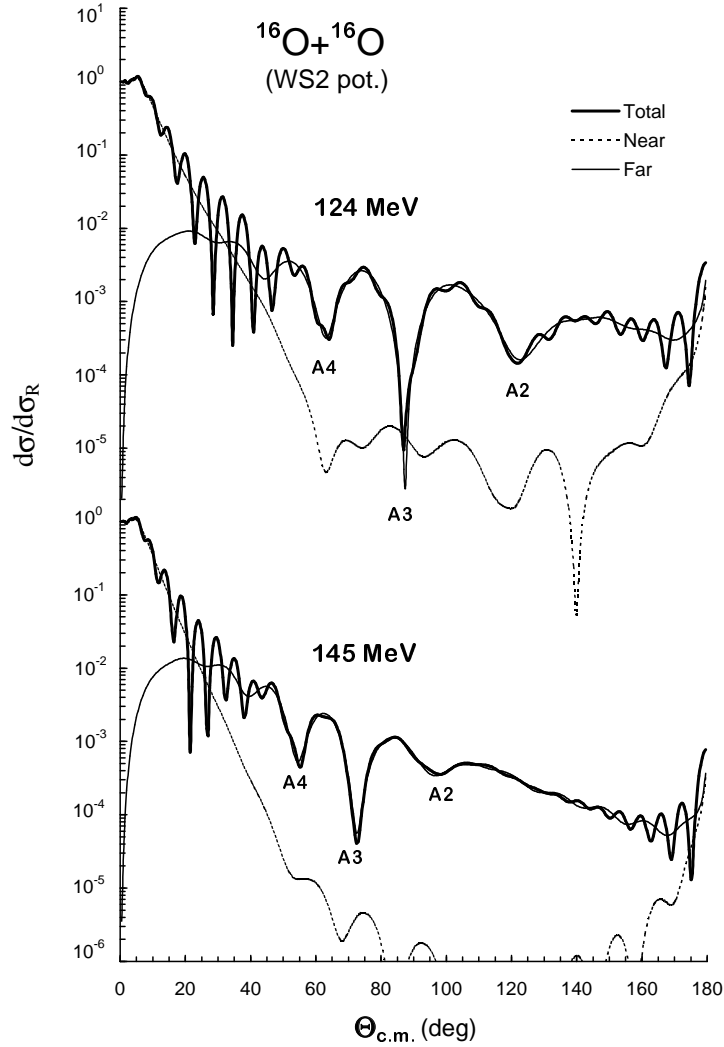


**Figure 10.** Decomposition of the unsymmetrized  $^{16}\text{O}+^{16}\text{O}$  elastic scattering cross section (thick solid curves) at  $E_{\text{lab}} = 124$  and  $145$  MeV into the nearside (dotted curves) and farside (solid curves) components using Fuller's method [26]. The Woods-Saxon squared (WS2) potentials, which give the best fit to the data measured at these energies by Sugiyama *et al.* [29, 30], have been used in the OM calculation.  $Ak$  indicates the  $k$ -th order of the Airy minimum in the farside cross section. Illustration taken from Ref. [24].

interaction (through the attractive nucleus-nucleus OP). Therefore, nuclear rainbows are absent in any scattering that does not involve a strong nuclear interaction, like, e.g., the electron-nucleus scattering. Even for the nucleon-nucleus scattering the real OP turns out to be too weak to produce the Airy pattern [4]. The rainbow pattern can appear only in the refractive  $\alpha$ -nucleus or nucleus-nucleus scattering with a deep, strongly attractive real OP [5, 7].

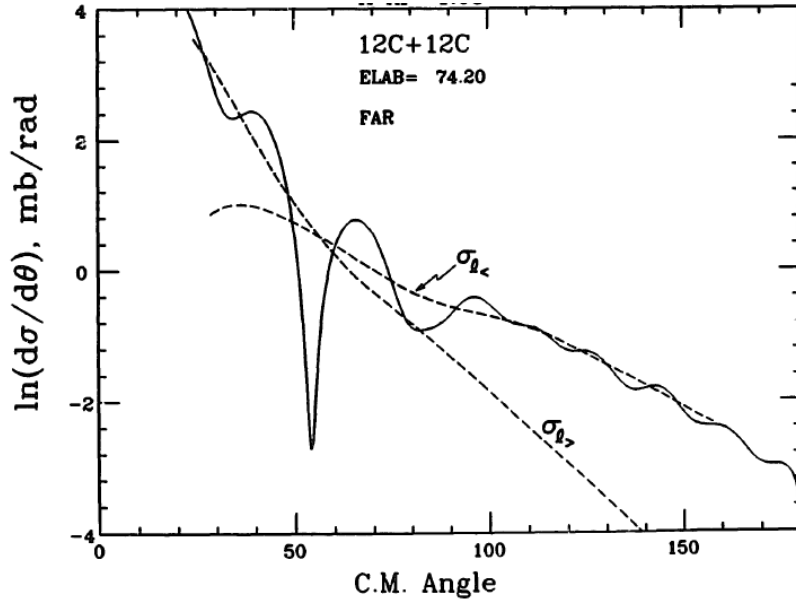


**Figure 11.** The decomposition of the farside cross section of the elastic  $^{12}\text{C}+^{12}\text{C}$  scattering at  $E_{\text{lab}} = 74.2$  MeV into its  $l_{<}$  and  $l_{>}$  components, using an OP of the Woods-Saxon shape which gives the best fit to the data [11]. The two minima at  $\Theta_{\text{c.m.}} \approx 53^\circ$  and  $80^\circ$  were identified by McVoy and Brandan [31] as the fourth (A4) and third (A3) Airy minima, respectively. Illustration taken from Ref. [31].

As an example, the nearside/farside decomposition of the elastic  $^{16}\text{O}+^{16}\text{O}$  scattering amplitude (using Fuller's method [26]) is shown in Fig. 10. It can be seen that the Fraunhofer diffraction pattern observed at small angles is due to an interference between the nearside and farside amplitudes in forward direction. At large angles, the elastic scattering pattern is determined dominantly by the farside amplitude, and the Airy oscillation pattern can be well observed when the absorption is weak (like that found for the  $^{16}\text{O}+^{16}\text{O}$  system). In such a case, if one can measure accurately the scattering cross section down to  $d\sigma/d\sigma_{\text{R}} \approx 10^{-5}$ , very valuable information on the real nucleus-nucleus OP is obtained. The (broad) Airy oscillation pattern seen at large angles in Fig. 10 originates from an interference between the  $l_{<}$  and  $l_{>}$  components of the farside amplitude which correspond to trajectories scattered at the same angle  $\Theta$  with angular momenta  $l < l_{\text{R}}$  and  $l > l_{\text{R}}$ , where  $l_{\text{R}}$  is the angular momentum associated with the rainbow angle  $\Theta_{\text{R}}$ . From the simple relation  $(l + 1/2)\hbar = kR$  one can find that the  $l_{<}$  and  $l_{>}$  trajectories are related to smaller and larger impact parameters, respectively (compared with that given by  $l_{\text{R}}$ ).

The absorption due to all non-elastic processes is always present in the elastic nucleus-nucleus scattering and reduces strongly the  $l_{<}$  amplitudes relative to the  $l_{>}$  ones. Therefore, in a strongly absorbing HI system, the  $l_{<}$  contributions are totally suppressed and the elastic scattering cross section decreases exponentially with increasing scattering

angles, without showing any interference structure. In terms of the complex nucleus-nucleus OP, the imaginary (absorptive) potential must be *weak* enough for the  $l_<$  component of the farside amplitude to survive in the elastic channel and the real OP must be strong enough to deflect trajectories to large 'negative' scattering angles, thus giving rise to the Airy interference between the  $l_<$  and  $l_>$  amplitudes. Based on a realistic choice of the OP for a refractive rainbow system, it is possible to extract from the farside scattering amplitude the explicit contributions from the  $l_<$  and  $l_>$  amplitudes and provide a complete description of the observed Airy interference structure (see, e.g., the decomposition done for the  $^{12}\text{C}+^{12}\text{C}$  system by Brandan and McVoy [31] in Fig. 11). The Airy oscillation arising from the  $l_<$  and  $l_>$  interference is shown schematically in Fig. 12 where one can explain the oscillation pattern in the scattering cross section (shown in Figs. 10 and 11) using a three-slit interference mechanism.

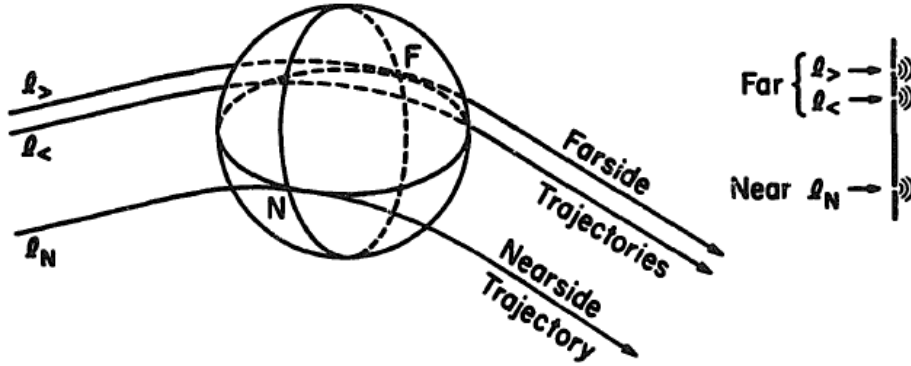


**Figure 12.** Schematic representation of three trajectories being deflected to the same scattering angle. The right-hand part shows the analogy to a three-slit interference pattern. Illustration taken from Ref. [31].

With the proper choice for the OP (and its energy dependence) not only a complete description of the observed Airy interference structure is obtained but also the evolution of the Airy pattern with the incident energies is well explained. For example, the nearside/farside decomposition of the elastic  $^{16}\text{O}+^{16}\text{O}$  scattering amplitude at different energies [24] has revealed a consistent evolution of the Airy interference pattern in the  $^{16}\text{O}+^{16}\text{O}$  system with increasing incident energies. While higher-order Airy minima were identified at low energies (see Fig. 10), the first Airy minimum A1 could be clearly seen only in the elastic  $^{16}\text{O}+^{16}\text{O}$  scattering data at higher energies, with the pronounced primary rainbow maximum following A1 established at  $E_{\text{lab}} = 350$  MeV (see Fig. 13). The observed broad bump of the primary rainbow at  $\Theta_{\text{c.m.}} \approx 50^\circ$  is quite sensitive to the  $^{16}\text{O}+^{16}\text{O}$  optical potential at small distances.

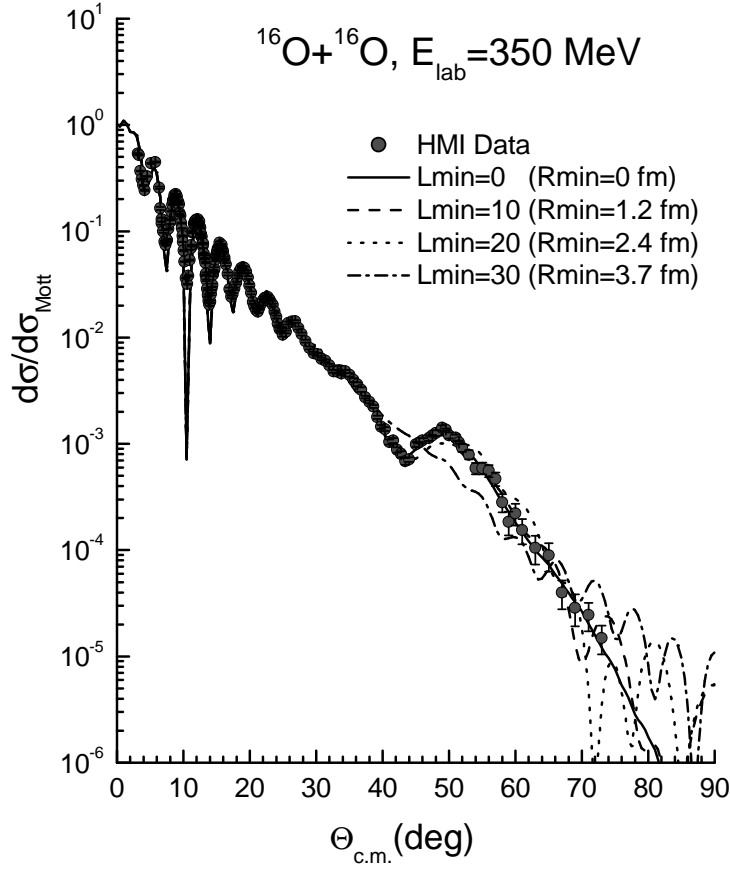


**Figure 13.** Elastic  $^{16}\text{O}+^{16}\text{O}$  scattering data [14, 15] at  $E_{\text{lab}} = 350$  MeV in comparison with OM description using the real folded potential and WS imaginary potential [24], and different cutoffs for the lowest partial wave  $L_{\text{min}}$ ; the corresponding impact parameters are  $R_{\text{min}}$ . The observed minimum at  $\Theta \approx 44^\circ$  has been established [24] as the first Airy minimum (A1) which is followed by a broad bump of the primary rainbow.

In Fig. 13, we show the OM calculations of the elastic  $^{16}\text{O}+^{16}\text{O}$  scattering at  $E_{\text{lab}} = 350$  MeV, using the real OP given by the folding model, with different cutoff values of the lowest partial wave in the expansion (6) of the elastic scattering amplitude. One can see that the data points at large angles are indeed sensitive to very low partial waves which correspond to the distances as small as  $R \approx 2 - 4$  fm. This result shows again that the considered elastic  $^{16}\text{O}+^{16}\text{O}$  data provide us with a valuable test of the nucleus-nucleus interaction at small distances. The role of the weak absorption in observing the rainbow structure is illustrated in Fig. 14, where the secondary Airy minimum (A2) preceding the first bump (lower part of Fig. 14) can be revealed only if the strength of the imaginary part of the OP is reduced in the OM calculation. The energy dependence of the position of the first Airy minimum in the farside cross section of elastic  $^{16}\text{O}+^{16}\text{O}$  scattering [24] shows that the incident energy should be between 300 and 450 MeV for the first Airy minimum A1 to appear in the most favorable angular



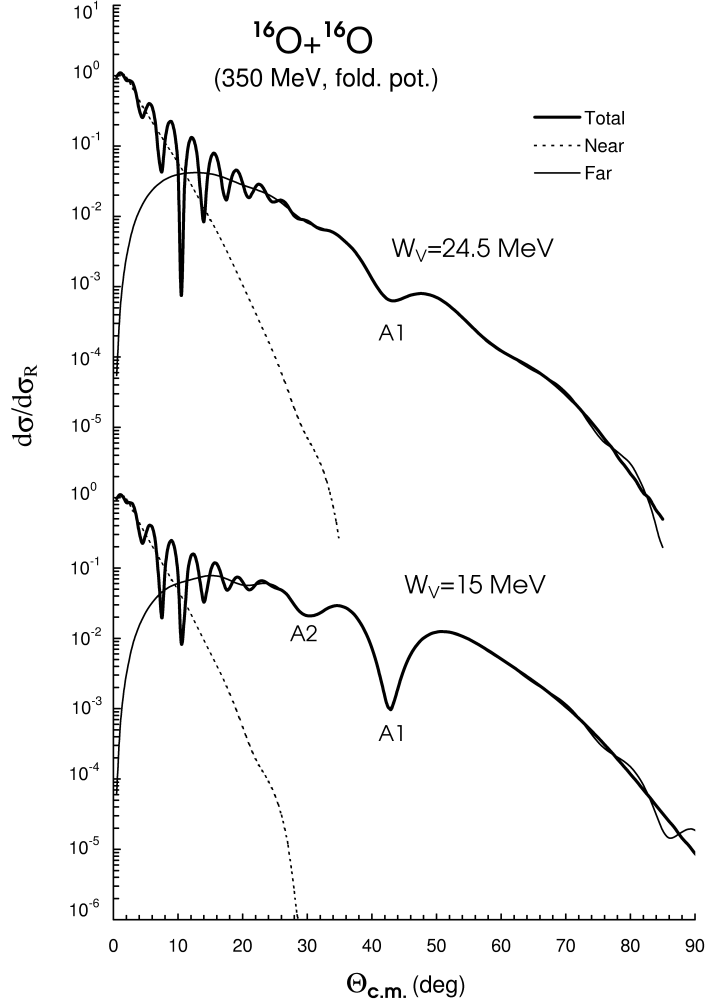


**Figure 14.** Decomposition of the unsymmetrized  $^{16}\text{O}+^{16}\text{O}$  elastic scattering cross section (thick solid curves) at  $E_{\text{lab}} = 350$  MeV into the nearside (dotted curves) and farside (solid curves) components using Fuller's method [26]. Upper part: given by the same real folded and WS imaginary potentials as those used in Fig. 13; lower part: given by the same real folded potential but with a reduced strength of the WS imaginary potential, A1 and A2 are the first and second Airy minima. Illustration taken from Ref. [24].

range ( $\Theta_{\text{c.m.}} \approx 30^\circ - 60^\circ$ ). In this angular region, the distorting effects by the Mott interference in the symmetric  $^{16}\text{O}+^{16}\text{O}$  system are minimal and diffractive structures are absent. Thus, the experiment of elastic  $^{16}\text{O}+^{16}\text{O}$  scattering at 350 MeV [14, 15] turned out to be a perfect choice for the observation of the primary nuclear rainbow.

Only after the evolution of the Airy interference pattern in the  $^{12}\text{C}+^{12}\text{C}$  and  $^{16}\text{O}+^{16}\text{O}$  systems with energy is well understood, one could go further and explain

the shape of the  $90^\circ$  excitation functions of the elastic scattering at energies from the Coulomb barrier up to about 20-30 MeV/nucleon. Such studies of the evolution of the Airy interference pattern in the excitation function of elastic scattering have been done for the  $^{16}\text{O}+^{16}\text{O}$  system by Kondo *et al.* [30] and for the  $^{12}\text{C}+^{12}\text{C}$  system by McVoy and Brandan [31]. In particular, the various deep and shallow minima in the excitation function measured for the  $^{12}\text{C}+^{12}\text{C}$  system, which gave rise to the famous “elephant interpretation” of the excitation function (see Fig. 15 or Fig. 1 in Ref. [31]) have remained an unsolved mystery for some 20 years. This was solved with the most realistic families of the  $^{12}\text{C}+^{12}\text{C}$  optical potential [31] which give the correct and consistent description of the rainbow structure in the elastic scattering cross section at different energies. In terms of the nuclear rainbow scattering, the gross structures of the  $^{12}\text{C}+^{12}\text{C}$  excitation function shown in Fig. 15 are caused by the refractive structures passing through  $90^\circ$ , and the sharp minima between the elephants correspond to the Airy minima of different orders drifting through  $90^\circ$  [5]. Actually, the minima at  $E_{\text{lab}} \approx 102$  and 124 MeV are the second (A2) and first (A1) Airy minima, respectively, so that there will not be a fourth elephant at higher energies.

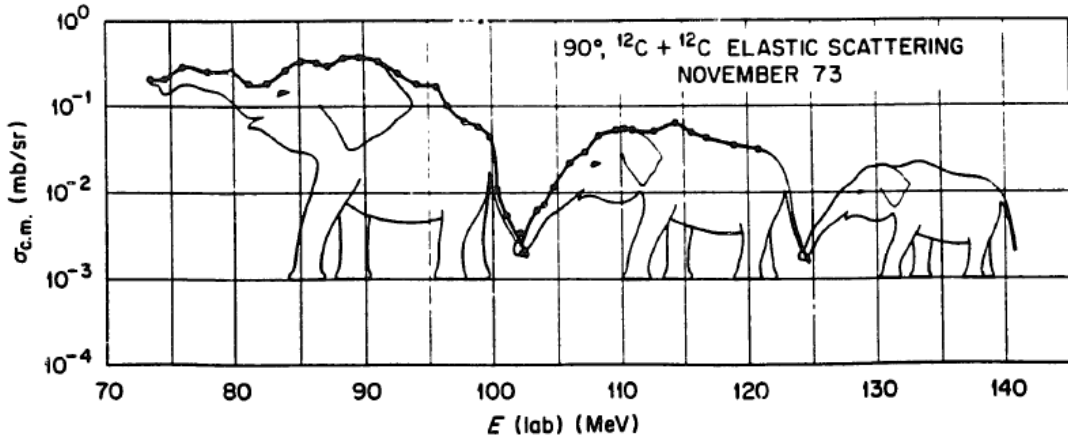


**Figure 15.** The “elephant interpretation” of the shape of the  $90^\circ$  excitation function measured for the  $^{12}\text{C}+^{12}\text{C}$  system. Illustration taken from Ref. [31].

Although the nearside/farside decomposition of the elastic scattering cross section, like those shown in Figs. 10 and 14, can be done *exactly* with the quantal scattering amplitude using Fuller’s method [26], the oscillating interference pattern at small angles can also be given by a semiclassical, but quite illustrative, approach developed by Hussein and McVoy [32] based on the strong absorption model. Namely, the observed oscillating cross sections seen at forward angles, e.g., in Figs. 10 and 14, is caused by the diffractive scattering of the incident wave into the classically forbidden region where both  $f_N(\Theta)$  and  $f_F(\Theta)$  decrease exponentially with  $\Theta$  and can be approximately

expressed [22, 32] as

$$\begin{aligned}\sqrt{2\pi \sin \Theta} f_N(\Theta) &\sim \exp(-i\lambda_g \Theta) \exp(-\gamma_N(\Theta - \Theta_g)), \\ \sqrt{2\pi \sin \Theta} f_F(\Theta) &\sim \exp(i\lambda_g \Theta) \exp(-\gamma_F(\Theta + \Theta_g)).\end{aligned}\quad (10)$$

Here  $\Theta_g$  is the grazing angle associated with the grazing angular momentum  $\hbar\lambda_g = \hbar(l_g + 1/2)$ . The oscillating pattern of the elastic angular distribution at small angles is due to the interference between  $f_N(\Theta)$  and  $f_F(\Theta)$  amplitudes, with a characteristic spacing of  $\Delta\Theta \simeq \pi/\lambda_g$ . It is obvious that the interference pattern depends strongly on the slope parameters of the nearside ( $\gamma_N$ ) and farside ( $\gamma_F$ ) amplitudes. A real *attractive* OP refractively enhances  $f_F(\Theta)$  over  $f_N(\Theta)$  (with  $\gamma_N > \gamma_F$ ) and allows there to be an angle

$$\bar{\Theta} = \Theta_g(\gamma_N + \gamma_F)/(\gamma_N - \gamma_F), \quad (11)$$

known as ‘Fraunhofer crossover’, where  $|f_N(\bar{\Theta})| = |f_F(\bar{\Theta})|$  and the nearside/farside interference oscillation reach its maximum amplitude. At small scattering angles ( $\Theta < \bar{\Theta}$ ) which correspond to peripheral impact parameters, the nearside component is dominant, with positive-angle scattering caused by the *repulsion* from scattering centre. At large scattering angles ( $\Theta > \bar{\Theta}$ ) which correspond to small impact parameters,  $f_F(\Theta)$  becomes stronger than  $f_N(\Theta)$ , with negative-angle scattering caused by the *attraction* toward scattering centre. Thus, an accurate experimental observation of Fraunhofer crossover  $\bar{\Theta}$  would give us a good measure of the refraction and attractive strength of the real OP causing it. The elastic angular distribution is usually characterized by a deep interference minimum in the vicinity of  $\bar{\Theta}$ , while the minima become progressively less marked as  $\Theta$  moves from  $\bar{\Theta}$  on either side as shown in Fig. 14. In the  $^{16}\text{O}+^{16}\text{O}$  case, the measured elastic angular distribution at 350 Mev shows a deep minimum at  $\Theta \approx 10^\circ$  which is in fact associated with the Fraunhofer crossover  $\bar{\Theta}$  given by the realistic OP for this system (see Figs. 13 and 14).

As a complimentary method to the nearside/farside decomposition, Michel *et al.* [33] have pointed out that the observed Airy interference pattern in the elastic  $^{16}\text{O}+^{16}\text{O}$  scattering can also be described by a barrier-wave/internal-wave (B/I) decomposition of the scattering amplitude using the same OP as that used in the nearside/farside decomposition of Ref. [24]. Such a method was first proposed by Brink and Takigawa [34] and has been shown by Michel *et al.* to be a very useful tool to disentangle the scattering trajectories into the surface and internal components. For the farside trajectories which probe the nucleus-nucleus OP at small distances, the B/I decomposition method was shown to give about the same Airy interference pattern as that given by the decomposition of the farside amplitude into the  $l_<$  and  $l_>$  components (compare Fig. 10 and Fig. 16). The B/I decomposition method was also used to study the  $^{12}\text{C}+^{12}\text{C}$  system [35] and the sequence of the Airy minima which made up the “elephants” shown in Fig. 15 has been confirmed. Therefore, the two methods [24, 33] are very complementary to each other and give us a complete physical understanding of the nuclear rainbow scattering phenomenon.

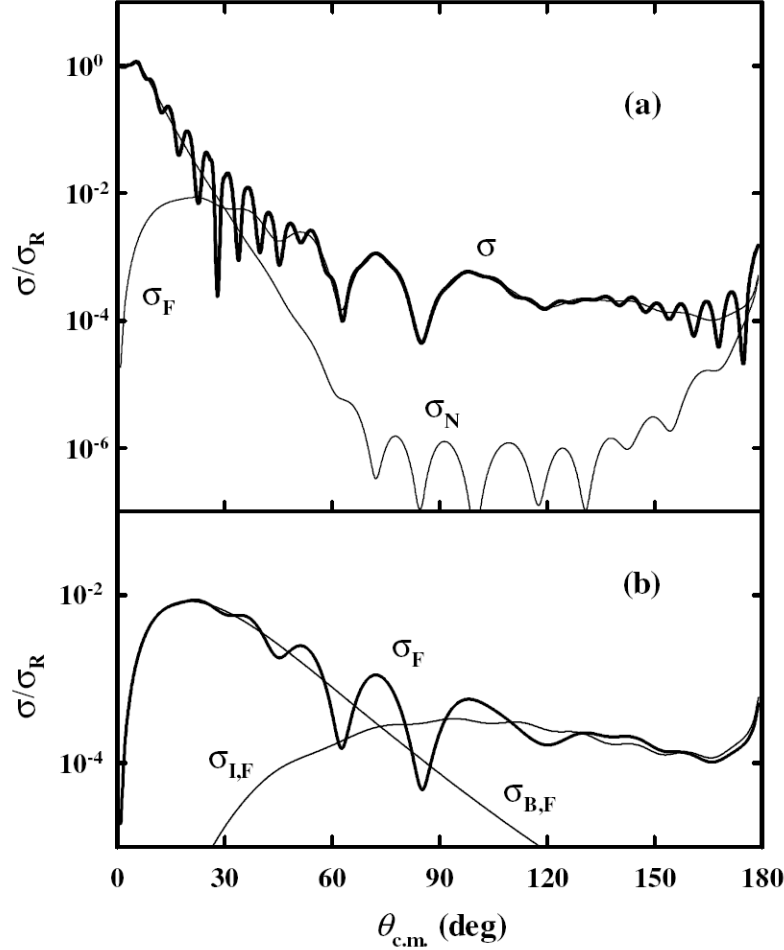


**Figure 16.** Decomposition of the unsymmetrized  $^{16}\text{O}+^{16}\text{O}$  elastic scattering cross section (thick solid curves) at  $E_{\text{lab}} = 124$  MeV [33] into the nearside and farside components (a), and a further decomposition (b) of the farside cross section into the barrier-wave (B,F) and the internal-wave (I,F) components based on a semiclassical method by Brink and Takigawa [34]. Illustration taken from Ref. [33].

### 3. Brief systematics of the nuclear rainbow scattering data

#### 3.1. $^{16}\text{O}+^{16}\text{O}$ system

This is the “heaviest” HI system so far that has shown a prominent rainbow pattern in the elastic scattering cross section. We give here a brief survey of the experimental elastic  $^{16}\text{O}+^{16}\text{O}$  scattering data which show consistently the refractive (rainbow) structure over a wide range of energies. At low energies, the accurate data have been measured (up to sufficiently large angles) at IreS in Strasbourg [36] at  $E_{\text{lab}} = 75 \rightarrow 124$  MeV (see Fig. 17). Although these data show a prominent oscillating Airy structure of the elastic cross section, this Airy pattern is strongly distorted on either side of  $\Theta_{\text{c.m.}} = 90^\circ$  by the Mott

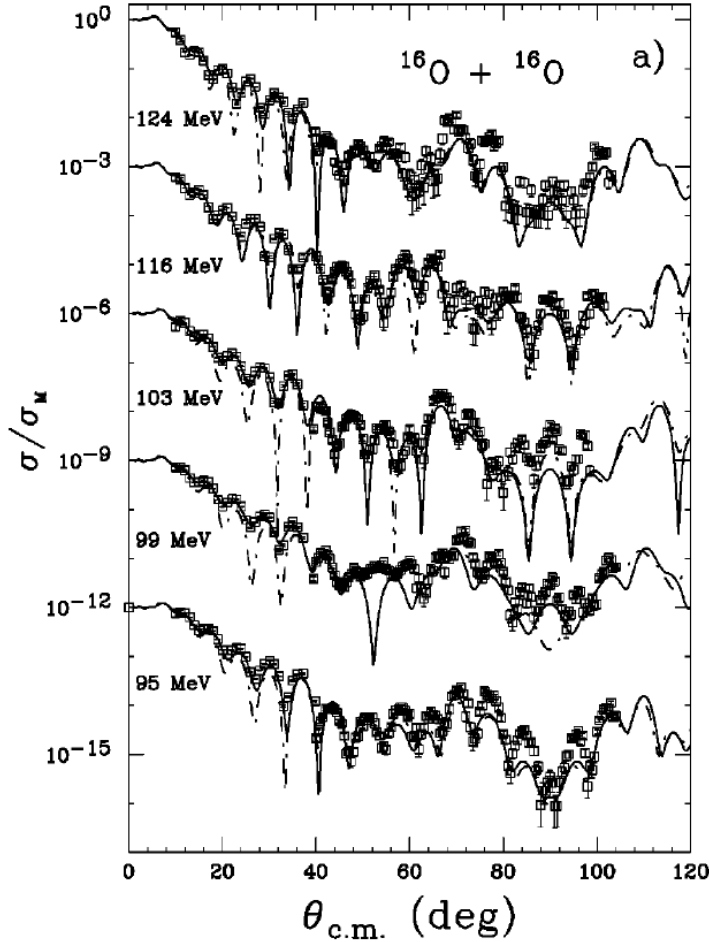


**Figure 17.** Elastic  $^{16}\text{O}+^{16}\text{O}$  scattering data measured at  $E_{\text{lab}} = 95 \rightarrow 124$  MeV in comparison with OM fits using the optical potentials of (quadratic) Woods-Saxon shape (solid curves) and that obtained with the folding model (dotted curves). Illustration taken from Ref. [36].

interference. The elastic scattering data at  $E_{\text{lab}} = 250, 350$  and  $480$  MeV were measured using the Q3D magnetic spectrometer at the cyclotron of the Hahn-Meitner Institute (HMI) in Berlin [14, 15, 16], with the most pronounced primary rainbow maximum observed at  $350$  MeV. The data at higher energies of  $E_{\text{lab}} = 704$  and  $1120$  MeV were measured at GANIL using the SPEG magnetic spectrograph [16, 37] (see also revision of the  $704$  MeV data in Ref. [24]). In addition, the elastic  $^{16}\text{O}+^{16}\text{O}$  data at  $E_{\text{lab}} = 124$  and  $145$  MeV have been measured by Sugiyama *et al.* at JAERI (Tokai) [29, 30]. The JAERI data were used to investigate the evolution of the Airy interference pattern in the excitation function at lower energies [30]. The data sets obtained at JAERI, HMI and GANIL are summarized in Fig. 18.

We emphasize that in order to reveal the rainbow structure, a tremendous experimental effort is needed to measure data points at large angles where the elastic

cross sections become extremely small ( $d\sigma/d\sigma_R \leq 10^{-5}$ ). A remarkable feature in the  $^{16}\text{O}+^{16}\text{O}$  case is that we can follow the evolution of the primary and secondary Airy structures from high energies of  $E_{\text{lab}} = 350$  and 480 MeV, where the first Airy minimum is clearly seen, down to 124 MeV and lower, where the primary rainbow maximum moves beyond the observable angular range of  $\Theta_{\text{c.m.}} = 0^\circ \rightarrow 90^\circ$ . At lower energies, the higher-order Airy oscillation appears in the angular range of  $\Theta_{\text{c.m.}} < 90^\circ$ . It should be made clear that the *secondary* Airy maximum is *not* the analog of the secondary atmospheric rainbow seen in the nature with the reversed colour sequence due to a second reflection inside of the water droplets. The second and higher-order Airy minima observed in the low-energy  $^{16}\text{O}+^{16}\text{O}$  elastic data are, in fact, the analogs of the first and higher-order supernumeraries observed in the atmospheric rainbow (see the faint bows located below the primary bow in Fig. 5). We note that the Mott interference caused by the boson symmetry between the two identical  $^{16}\text{O}$  nuclei leads in addition to a rapidly oscillating elastic cross section at angles around  $\Theta_{\text{c.m.}} = 90^\circ$ , which obscures the Airy structure in this angular region. Therefore, the Airy pattern can best be seen in an OM calculation, where the boson symmetrization is artificially removed, as shown in Figs. 10 and 16 for the case of  $E_{\text{lab}} = 124$  MeV.

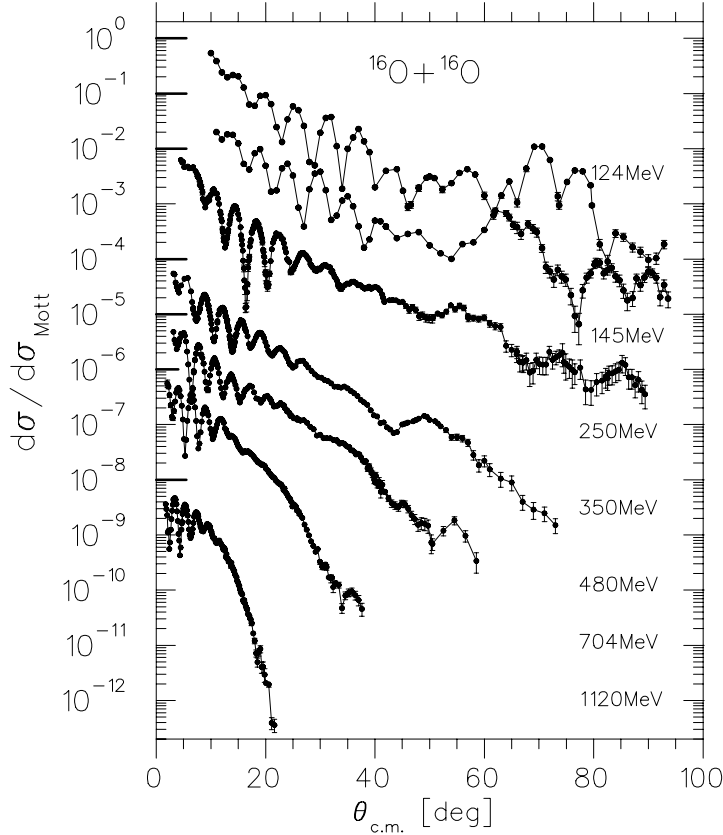


**Figure 18.** Elastic  $^{16}\text{O}+^{16}\text{O}$  scattering data measured at  $E_{\text{lab}} = 124, 145$  MeV [29, 30], 250, 350, 480 MeV [14, 15, 16], 704 and 1120 MeV [16, 24, 37]. The primary rainbow maximum at 350 MeV is located at  $\Theta_{\text{c.m.}} \approx 50^\circ$ . The lines are to guide the eye. Illustration taken from Ref. [38].

### 3.2. Other systems

It should be recalled that the pioneering nuclear scattering experiment that led to the observation of the nuclear rainbow was the study of the elastic  $\alpha$ -nucleus scattering at  $E_{\text{lab}} \approx 140$  MeV by Goldberg *et al.* [9, 10]. Our today's understanding of the nuclear rainbow as a refractive phenomenon has been established based on detailed OM studies of the elastic  $\alpha$ -nucleus scattering. While  $^4\text{He}$  can be considered as the lightest HI, it is a very “robust” projectile (with the nucleon separation energy of 21 MeV) and it can penetrate rather deep into the interior of the target nucleus without being absorbed. If the elastic  $\alpha$ -nucleus scattering data by Goldberg *et al.* [9, 10] remain the best evidence for the nuclear rainbow scattering observed for different targets at a given incident energy, the high-precision  $\alpha+^{90}\text{Zr}$  data measured by Put and Paans [39] several years later (see Fig. 19) present a unique picture of how the primary rainbow pattern associated with the first Airy minimum evolves with the energy. While the farside scattering begins to dominate the large-angle scattering already at the  $\alpha$ -particle energy of 59 MeV, the most pronounced primary rainbow shoulder is observed at the energies of 80 MeV and higher. These data, together with the data of  $\alpha+^{90}\text{Zr}$  measured at 141.7 MeV [10], provide us with a very accurate test ground for theoretical models of the  $\alpha$ -nucleus OP.

The elastic and inelastic  $\alpha$ -nucleus scattering on different targets has been precisely measured at  $E_{\text{lab}} = 104$  MeV by Karlsruhe group (see, e.g., Ref. [40] for an overview). Given the broad bump of the primary rainbow observed at large angles, the Karlsruhe data have been used successfully to probe the nuclear matter distribution and determine the real  $\alpha$ -nucleus OP at 104 MeV by a “model independent” method (see Fig. 21 below). Among light HI systems, the elastic  $^{12}\text{C}+^{12}\text{C}$  scattering has been studied extensively since the 70's of the last century and the nuclear rainbow pattern has been established and investigated based on the elastic  $^{12}\text{C}+^{12}\text{C}$  data measured at energies from about 6 up to 200 MeV/nucleon (see a detailed systematics of the elastic  $^{12}\text{C}+^{12}\text{C}$  data in Ref. [5]). While the  $^{12}\text{C}+^{12}\text{C}$  and  $^{16}\text{O}+^{16}\text{O}$  systems are quite ‘transparent’ for refractive effects to appear, the Mott interference caused by the boson symmetry between the two identical nuclei leads to rapidly oscillating elastic cross sections at angles around  $\Theta_{\text{c.m.}} = 90^\circ$ , which in turn distort the original Airy structures. The  $^{16}\text{O}+^{12}\text{C}$  system does not have the boson symmetry and was suggested as a good candidate for the study of the nuclear rainbow [5]. However, up to the late 90's, the available elastic data for this system covered only limited angular intervals and did not allow to reveal any feature of refractive scattering. This has motivated several high-precision experiments on the elastic  $^{16}\text{O}+^{12}\text{C}$  scattering by Ogloblin *et al.* [41, 42] where the elastic  $^{16}\text{O}+^{12}\text{C}$  cross sections have been measured accurately, to cover a large angular region, at  $E_{\text{lab}} = 132, 170, 200, 230$  and 260 MeV. These data show clearly the diffractive and refractive scattering patterns at small and large scattering angles, respectively. The nearside/farside decomposition of the elastic  $^{16}\text{O}+^{12}\text{C}$  scattering amplitudes at these energies [42] has led to about the same pronounced Airy interference pattern as those observed in the symmetric  $^{12}\text{C}+^{12}\text{C}$

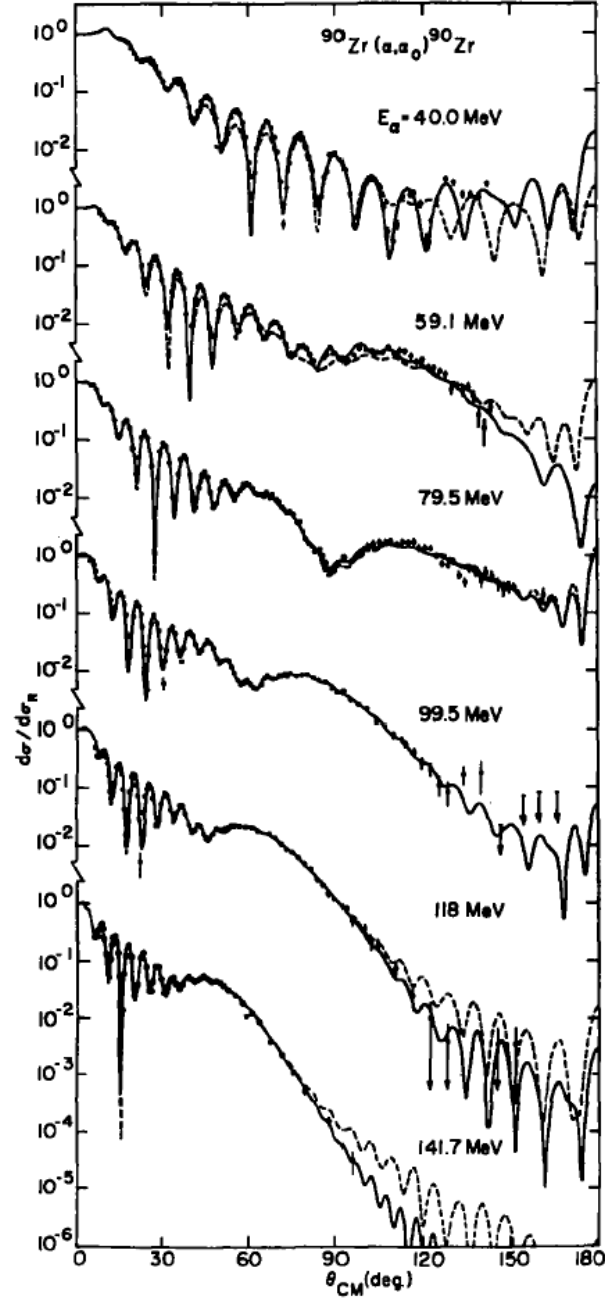


**Figure 19.** Elastic  $\alpha + {}^{90}\text{Zr}$  scattering data measured at  $E_{\text{lab}} = 40 - 118$  MeV by Put and Paans [39] and at the higher energy of 141.7 MeV by Goldberg *et al.* [10] in comparison with the OM results given by the set of deep real optical potentials. Illustration taken from Ref. [39].

and  ${}^{16}\text{O} + {}^{16}\text{O}$  systems (see Fig. 20). Although not distorted by the Mott interference, the observed backward rise of the elastic cross section towards  $\Theta_{\text{c.m.}} = 180^\circ$  has been shown [44] to partially originate from the elastic  $\alpha$ -particle transfer between the projectile and target, and this gives again some additional interference structures. Elastic  ${}^{16}\text{O} + {}^{12}\text{C}$



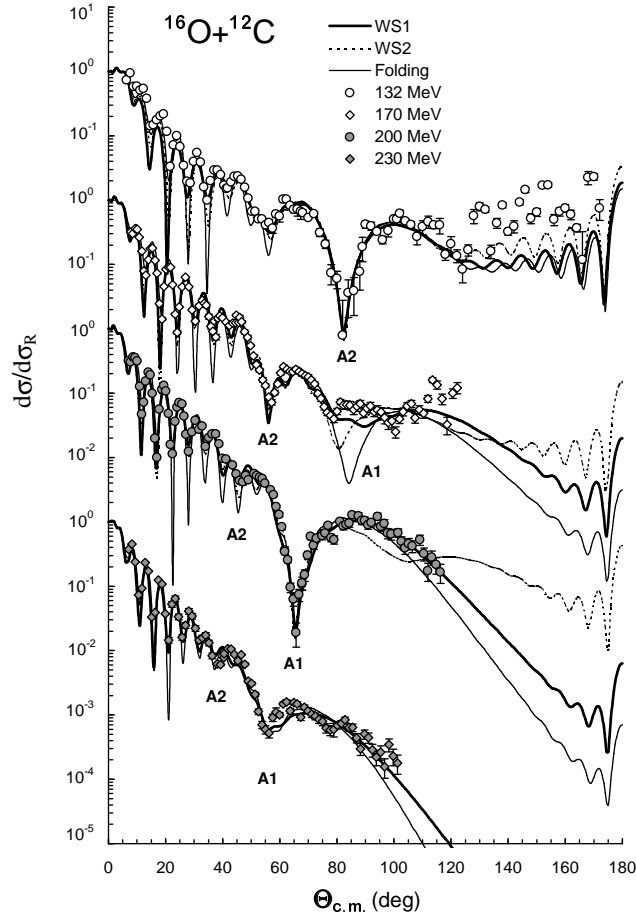


**Figure 20.** The elastic  $^{16}\text{O}+^{12}\text{C}$  scattering data at  $E_{\text{lab}} = 132, 170, 200$  and  $230$  MeV in comparison with the OM fits given by the folding potential and two different families of the Woods-Saxon potential. A1 and A2 are the first and second Airy minima generated by the folding potential. Illustration taken from Ref. [42].

scattering at lower energies were measured by the Strasbourg group and the higher-order Airy oscillatory pattern has been established [43] which is similar to that observed in the  $^{16}\text{O}+^{16}\text{O}$  and  $^{12}\text{C}+^{12}\text{C}$  systems. With a rather weak absorption in the  $^{16}\text{O}+^{12}\text{C}$  system, the evolution of the Airy minima in the elastic  $^{16}\text{O}+^{12}\text{C}$  scattering at medium [42] and low [43] energies can be consistently described by the energy dependent real OP given by the folding model.

We finally note that the rainbow pattern has also been observed in the elastic scattering of  $^6,^7\text{Li}$  at energies up to around 50 MeV/nucleon [45, 46, 47] and  $^9\text{Be}$  at 18 MeV/nucleon [48]. For example, the elastic  $^6\text{Li}$  scattering on the light targets has shown a broad exponential falloff in the cross section at large angles which was identified as the “shoulder” of the primary rainbow maximum. The OM analysis [48] of the elastic  $^9\text{Be}$  scattering from  $^{12}\text{C}$  and  $^{16}\text{O}$  targets has found a rather weak primary Airy minimum

in the cross section at large angles. Since this Airy structure was strongly damped and scarcely visible, it was referred to as the rainbow “ghost” [48]. The less pronounced rainbow structure observed in these cases compared to those observed earlier in the elastic  $\alpha$ -nucleus scattering at about the same energies is due to a stronger absorption caused, in particular, by the breakup of these ( $\alpha$ -clustered) projectiles [49, 50]. See more discussions on the refractive  ${}^6\text{Li}$  scattering in the Sec. 8 below.

#### 4. Theoretical basis of the nucleus-nucleus OP

As discussed above, the nuclear rainbow can only be properly identified and studied based on a *realistic* choice of the nucleus-nucleus optical potential. In general, the optical potential is an effective interaction  $U(R)$  between the two colliding nuclei (whose centres of mass are separated by the distance  $R$ ) which is used in the following (one-body) Schrödinger equation for elastic scattering

$$\left[ -\frac{\hbar^2}{2\mu} \nabla^2 + U(R) + V_C(R) - E \right] \chi(\mathbf{R}) = 0. \quad (12)$$

Here  $E$  is the energy of relative motion in the centre-of-mass (c.m.) system,  $\mu$  is the reduced mass of the two colliding nuclei, and  $V_C(R)$  is the Coulomb potential. The spin and isospin dependence of  $U(R)$  is neglected for the simplicity of discussions. It is assumed in the OM calculation that the two nuclei remain in their ground states during the elastic scattering and higher-order effects due to the coupling to other non-elastic reaction channels are taken into account by the imaginary part  $W$  of the OP which describes the loss of incident flux (*absorption*) into the open non-elastic channels. The elastic scattering cross section is then obtained [22] using the solution  $\chi(\mathbf{R})$  of Eq. (12), with appropriate boundary conditions. One can see from Eq. (3) that the use of a complex OP in Eq. (12) is analogous to the introduction of a complex index of refraction (used in the optics to describe the propagation of light through an absorbing medium), so that the “rainbow” interpretation of the elastic nucleus-nucleus scattering can well be justified based on the solution of Eq. (12).

The simplest procedure of an OM analysis is to adopt a phenomenological functional form for  $U(R)$  and adjust its parameters until the calculated elastic cross section agrees with the measurement. The most widely used functional form for the OP is that based on the Woods-Saxon form factor [22] which is a default option in all the available OM codes for the nucleus-nucleus and nucleon-nucleus scattering. For some weakly absorbing, refractive  $\alpha$ -nucleus and light HI systems, it was possible to determine the phenomenological WS parameters of the OP without discrete ambiguity. Actually, after decades of the use of WS shapes for the nucleus-nucleus OP, it became certain that the squared WS shape (WS2) is the physically more preferable one. This WS2 shape is also close to the shape of the microscopic real OP given by the folding model. Therefore, if one uses the folding model to calculate the nucleus-nucleus OP for the study of elastic *refractive* nucleus-nucleus scattering, valuable information on the effective

nucleon-nucleon (NN) interaction can be obtained if realistic nuclear wave functions of the projectile and target nuclei are available.

#### 4.1. Feshbach's reaction theory for the nucleus-nucleus OP

A microscopic theory for the nuclear OP, as usually discussed in the literature, is just an approach to predict the nucleon-nucleus or nucleus-nucleus OP starting essentially from the NN interaction between the nucleons in the system and realistic nuclear wave functions for the projectile and target nuclei. In such a formulation, the rigorous microscopic foundation can be established only for the nucleon-nucleus OP based on the G-matrix studies of nuclear matter [51]. In particular, the G-matrix method has been used to construct the effective in-medium NN interaction for the microscopic folding calculation [52, 53] of the nucleon-nucleus OP at low and medium energies. The interaction between two composite nuclei is a much more complicated many-body problem due to the HI collision dynamics, and there is no truly microscopic theory for the nucleus-nucleus OP like that for the nucleon-nucleus OP which is based on the G-matrix only. However, an approximate approach to the microscopic understanding of the nucleus-nucleus OP can be formulated [5] within the framework of the reaction theory by Feshbach [54].

Let us expand the total wave function for the two colliding nuclei in terms of the complete set of internal wave functions of the projectile ( $a$ ) and target ( $A$ ) nuclei as

$$\Psi = \sum_{mn} \chi_{mn}(\mathbf{R}) \psi_m^{(a)}(\xi_a) \psi_n^{(A)}(\xi_A), \quad (13)$$

where  $\chi_{mn}(\mathbf{R})$  describes the relative motion of the colliding system when projectile and target are in states labelled by  $m$  and  $n$ , respectively. With the ground states labelled by  $m = 0$  and  $n = 0$ , elastic scattering is described by  $\chi_{00}(\mathbf{R})$ . Within the OM frame, the nucleus-nucleus OP should generate  $\chi_{00}(\mathbf{R})$  when used in Eq. (12). In general, the expansion (13) must be inserted into the many-body Schrödinger equation which gives an infinite set of coupled equations for  $\chi_{mn}(\mathbf{R})$  after the integration over internal coordinates  $\xi_a$  and  $\xi_A$ . By using Feshbach's projection operator [22, 54], we obtain the equivalent effective interaction between the two nuclei  $U$  which acts in the elastic channel only and, hence, can be used in Eq. (12) to determine  $\chi_{00}(\mathbf{R})$ .

$$U = V_{00} + \lim_{\epsilon \rightarrow 0} \sum_{\alpha\alpha'}' V_{0\alpha} \left( \frac{1}{E - H + i\epsilon} \right)_{\alpha\alpha'} V_{\alpha'0}. \quad (14)$$

Here  $V_{\alpha\alpha'}$  is the first-order interaction between the two nuclei, where  $\alpha = mn$  stands for a pair of internal states of the projectile and target. The primed sum runs over all the pair states excluding  $\alpha = 0 \equiv 00$ . The first term of (14) is real and can be evaluated within the double-folding approach [21, 24, 55]

$$V_{00} = V_F \equiv (\psi_0^{(a)} \psi_0^{(A)} | V | \psi_0^{(a)} \psi_0^{(A)}), \quad (15)$$

where the round brackets denote integration over the internal coordinates  $\xi_a$  and  $\xi_A$  of the two nuclei being in their ground states  $\psi_0^{(a)}$  and  $\psi_0^{(A)}$ , respectively. We can rewrite

Eq. (14) now as

$$U = V_F + \Delta U. \quad (16)$$

Here,  $\Delta U$  is often referred to as the *dynamic polarization potential* (DPP) which arises from couplings to all the open non-elastic channels. Depending on the energy and the binding structures of the two colliding nuclei, the ‘polarizing’ contribution by the energy-dependent and complex  $\Delta U$  to the total nucleus-nucleus optical potential  $U$  can be quite substantial [5, 22, 49].  $\text{Im}\Delta U$  is the main source of the absorption (the imaginary part of the OP) due to transitions to the open non-elastic channels.  $\Delta U$  also contributes to the real part of the OP but  $\text{Re}\Delta U$ , which originates from virtual excitations of the two nuclei, is at least one order of magnitude smaller than  $V_F$  [5, 49]. Furthermore,  $\Delta U$  is nonlocal because the system that is excited into a non-elastic channel at position  $\mathbf{R}$  returns, in general, to the elastic channel at another position  $\mathbf{R}' \neq \mathbf{R}$ . Since the direct (one-step) elastic scattering occurs via the first-order folded potential  $V_F$ , the weaker the absorption caused by the DPP the stronger the refractive scattering which can lead to the appearance of the rainbow pattern at appropriate incident energies.

#### 4.2. The double-folding model

It is clear from the discussion above that  $V_{00}$ , the first term in Eq. (14), is the key quantity for our understanding of the nucleus-nucleus interaction when elastic scattering proceeds directly in one step. Among various models for the nucleus-nucleus OP, the double-folding model (see Refs. [5, 21, 55] and references therein) has been used most widely as a simple microscopic method to calculate  $V_F$  starting from an appropriately chosen effective NN interaction between nucleons in the system. Further input for the folding calculation are the realistic nuclear density distributions of the projectile and target nuclei which are deduced either directly from electron scattering data or from an appropriate nuclear structure model (See Fig. 33 below for an illustrative overview of the folding model analysis). The success of the double-folding model (DFM) in describing the observed elastic scattering of many HI systems suggests that it indeed produces the dominant part of the real nucleus-nucleus OP. Let us now briefly discuss the main features of a recent version of the DFM that has been used in our OM analyses of the refractive  $\alpha$ -nucleus and nucleus-nucleus scattering [56, 57, 58] and generalized for a consistent folding description of the elastic and inelastic nucleus-nucleus scattering [55].

In the folding approach, the real nucleus-nucleus interaction  $V$  is based on a sum of effective (two-body) NN interactions  $v_{ij}$  between nucleon  $i$  in the projectile  $a$  and nucleon  $j$  in the target  $A$

$$V = \sum_{i \in a, j \in A} v_{ij}. \quad (17)$$

Although the individual internal ground state (g.s.) wave functions  $\psi_0^{(a)}(\xi_a)$  and  $\psi_0^{(A)}(\xi_A)$  in Eq. (13) are each taken to be antisymmetrized, the Pauli principle still requires the total wave function  $\Psi$  also to be antisymmetric under interchange of nucleons between

the two nuclei. If we restrict this exchange of projectile and target nucleons to the one-nucleon exchange process known as the single-nucleon knock-on exchange (SNKE), then the effective NN interaction  $v_{ij}$  in Eq. (17) should be replaced by

$$v_{ij}(1 - P_{ij}) = v_D + v_{\text{EX}}P_{ij}^x, \quad (18)$$

$$\text{where } v_D \equiv v_{ij}^{(\text{D})} = v_{ij} \text{ and } v_{\text{EX}} \equiv v_{ij}^{(\text{EX})} = -v_{ij}P_{ij}^\sigma P_{ij}^\tau. \quad (19)$$

Here  $P_{ij}^x$ ,  $P_{ij}^\sigma$  and  $P_{ij}^\tau$  represent the operators for the exchange of spatial, spin and isospin coordinates of the nucleon pair, respectively. Due to the exchange of the spatial coordinates, the first term of Eq. (14) now consists of two components: the local direct part and *nonlocal* exchange part

$$V_{00} = V_F \equiv \left( \psi_0^{(a)} \psi_0^{(A)} \right) \left| \sum_{i \in a, j \in A} v_{ij}(1 - P_{ij}) \right| \psi_0^{(a)} \psi_0^{(A)} = V_F^{(\text{D})} + V_F^{(\text{EX})}. \quad (20)$$

As can be seen from Eq. (14) the imaginary part of the OP should be constructed from an appropriate theory for the dynamical polarization potential  $\Delta U$ . This is, however, a complicated task and lies well beyond the framework of the DFM. In many cases of elastic HI scattering, it was found sufficient to simply treat the effective NN interaction as having a complex strength determined from the analysis of elastic scattering data and the real and imaginary parts of the nucleus-nucleus OP have essentially the same radial shape. However, it has been found from the analyses of refractive  $\alpha$ -nucleus scattering [59] and of light HI scattering [5, 60] that the imaginary potential is definitely required to have a different shape, and the ratio of the imaginary to the real potential tends to peak near the nuclear surface but becomes relatively weak in the interior. Therefore, it is common to resort to a hybrid approach by using the DFM to generate the real part of the OP but to use a phenomenological (local) Woods-Saxon form factor  $W(R)$  for the imaginary part [55, 56, 57, 58]. Sometimes, like in the case of refractive  $^{16}\text{O} + ^{16}\text{O}$  scattering, the WS imaginary potential needs to be composed of two terms (volume + surface potentials) in order to match independently the absorption at small  $R$  and that at large  $R$ , in the surface region [24, 57, 58].

In general, the real folded potential (20) supplemented by a local WS imaginary potential should be inserted into Eq. (12) and, given a nonlocal exchange potential  $V_F^{(\text{EX})}$ , one needs to solve an integro-differential equation for the scattering wave function [61]. However, from a practical point of view a reliable local approximation for  $V_F^{(\text{EX})}$  is highly desirable. In this case, not only the OM calculation is much simpler, but also the comparison with the (local) phenomenological OP is much more direct which is particularly essential in the study of the nuclear rainbow scattering. The direct part of the folded potential is local and obtained from a double-folding integral over  $v_D$  and the g.s. densities of the two nuclei as

$$V_F^{(\text{D})}(R) = \int \rho_a(\mathbf{r}_a) \rho_A(\mathbf{r}_A) v_D(s) d^3r_a d^3r_A, \quad \mathbf{s} = \mathbf{r}_A - \mathbf{r}_a + \mathbf{R}. \quad (21)$$

We use a local WKB approximation [22] for the change in the relative motion wave function induced by the exchange of spatial coordinates of each interacting nucleon pair

$$\chi_{00}(\mathbf{R} + \mathbf{s}) \approx \exp\left(\frac{i\mathbf{K}(R)\mathbf{s}}{M}\right) \chi_{00}(\mathbf{R}), \quad (22)$$

where the recoil factor is  $M = aA/(a + A)$ , with  $a$  and  $A$  being the mass numbers of the projectile and target, respectively, and  $\mathbf{K}(R)$  is the local momentum of relative motion at the internuclear distance  $R$ . Then, the following local expression for the exchange folded potential can be obtained [53, 62, 63, 64]

$$V_F^{(\text{EX})}(R) = \int \rho_a(\mathbf{r}_a, \mathbf{r}_a + \mathbf{s}) \rho_A(\mathbf{r}_A, \mathbf{r}_A - \mathbf{s}) v_{\text{EX}}(s) \exp\left(\frac{i\mathbf{K}(R)\mathbf{s}}{M}\right) d^3r_a d^3r_A. \quad (23)$$

The local momentum of relative motion must be determined self-consistently through the total *real* OP as

$$K^2(R) = \frac{2\mu}{\hbar^2} [E - V_F^{(\text{D})}(R) - V_F^{(\text{EX})}(R) - V_C(R)]. \quad (24)$$

The calculation of  $V_F^{(\text{EX})}(R)$  still contains a self-consistency problem and involves an explicit integration over the *nonlocal* nuclear density matrices of the projectile and target. In practice, the nuclear g.s. densities are usually available in the local form. Therefore, the DFM calculation of the exchange potential has been done [55, 56, 57, 58] using a realistic approximation for the nonlocal density matrix [65, 66] that has been adopted earlier in the folding calculations of the nucleon-nucleus OP [53, 62]. This local approximation for the density matrix was shown [66] to be of around 1% accuracy in the DFM results for the  $\alpha$ -nucleus OP.

We note that a much simpler zero-range approximation for the SNKE has been used in numerous double-folding calculations. In this approach [21, 67], the knock-on exchange potential is included by adding a zero-range pseudo-potential to the interaction  $v_{ij}$  in Eq. (17). Namely,

$$v_{ij}(1 - P_{ij}) \rightarrow v_{ij}(s) + \hat{J}(E)\delta(\mathbf{s}), \quad (25)$$

which immediately makes the exchange potential  $V_F^{(\text{EX})}$  local. Here, the strength  $\hat{J}(E)$  of the pseudo-potential has been obtained by calibrating against “exact” calculations of the exchange potential for the nucleon-nucleus scattering [67]. Although this zero-range approximation has been used with some success in DFM calculations of the HI optical potential at low energies [21] where the data are sensitive only to the OP at the surface (near the strong absorption radius), it has been shown to be inadequate [64] in the case of rainbow scattering where the data are sensitive to the real OP over a wider radial domain. A very recent study by Hagino *et al.* [68] has also shown that the finite-range treatment of the localized exchange potential (23) gives the OM results very close to those obtained from the exact solution of integro-differential equation [61] using the explicit nonlocal  $V_F^{(\text{EX})}$ , while the zero-range prescription (25) gives a large discrepancy with the exact results.

We also note here a simpler folding approach (see, e.g., Ref [69]) to evaluate the nucleus-nucleus OP by the direct folding integration (21) only, using the so-called JLM

effective interaction. Since the complex JLM interaction was deduced (in a local density approximation) from the strengths of both the direct and exchange components of the G-matrix for infinite nuclear matter obtained by Jeukenne, Lejeune and Mahaux [52], the exchange term (23) of the folding potential is not explicitly treated in this approach.

Another approximate treatment of the exchange effects has been developed recently by the Sao Paulo group [70, 71] where the exchange non-locality is effectively taken into account by an exponential dependence of the potential strength on the local relative-motion momentum (24), as suggested some 40 years ago by Perey and Buck [72] for the nucleon-nucleus OP. In this case, the nucleus-nucleus OP is also evaluated by the direct folding integration (21) only, using an effective NN interaction fitted empirically to a global systematics of HI elastic data [71].

#### 4.3. Other microscopic approaches

Besides the double-folding model, there are at least two other important microscopic approaches developed in the past to study the nucleus-nucleus OP, which are the resonating group method (RGM) (see, e.g., Refs. [73, 74, 75]) and the nuclear matter approach by the Tübingen group [76, 77].

For the nucleus-nucleus elastic channel, the RGM freezes the two nuclei in their ground states, like the DFM, but takes full account of the exchange of projectile and target nucleons. A Schrödinger equation for the relative-motion wave function  $\chi_{00}(\mathbf{R})$  is then obtained with a highly nonlocal RGM “kernel”. Besides a local direct term which is just the double-folded potential  $V_F^{(D)}$ , the full antisymmetrization results in a hierarchy of nonlocal exchange terms, according to the number of nucleons exchanged. In practical calculations, an accurate localization procedure has been used to yield local potentials equivalent to these exchange terms [75]. After localization, the RGM approach predicts a deep real OP which becomes shallower with the increasing energy as the attractive exchange term becomes weaker, in the same manner as that given by the DFM calculation [24, 56]. These RGM studies also show that the SNKE contribution is the largest of the exchange terms and dominates for peripheral collisions due to the long range of single-nucleon exchange. In this sense, the more rigorous RGM method provides a solid theoretical justification for the DFM which only takes into account the SNKE for the exchange effects. The full antisymmetrization makes the RGM quite complicated and it can be used to estimate the real OP for very light systems only. Moreover, the inclusion of a realistic density dependence into the effective NN interaction (a very important ingredient in the folding calculation as explained below) is also a technical difficulty in the RGM due to its rigorous treatment of the exchange.

The basic physical picture of the nuclear matter (NM) approach [76, 77] is that the nucleus-nucleus collision is locally represented by the collision of two pieces of the NM whose densities are the local densities of the target and projectile. The momentum distribution of the colliding system with densities  $\rho_a$  and  $\rho_A$  is represented by two Fermi spheres with radii  $k_{Fa} = (1.5\pi^2\rho_a)^{1/3}$  and  $k_{FA} = (1.5\pi^2\rho_A)^{1/3}$  whose centres are separated

by the *asymptotic* momentum of the (nucleon) relative motion  $\hbar k = \sqrt{2mE/M}$ , where  $m$  is the nucleon mass and  $M$  is the recoil factor used in Eq. (22). It is easy to see that  $k = K_\infty/M$ , where  $K_\infty$  is derived from Eq. (24) at  $R \rightarrow \infty$  where one can neglect the OP. The exchange effects imposed by the Pauli principle, known as Pauli blocking in the G-matrix study of the NM, lead to a modification of the shape of two Fermi spheres [76] when they overlap, i.e., when  $k < k_{Fa} + k_{FA}$ . The OP between two nuclei separated by a distance  $R$  is then defined as the difference of the total energy of the system at  $R$  from that at infinity

$$U(R, k) = E(R, k) - E(\infty, k), \quad (26)$$

with the potential energy calculated from the G-matrix given by the Bethe-Goldstone equation for two Fermi spheres colliding in momentum space [76]. Although the nuclear matter approach can give some estimates for both the real and imaginary OP based on the complex Bethe-Goldstone G-matrix, the ansatz (26) remains questionable [5, 75] because the total energy  $E(R, k)$  does not determine just the relative motion while the two nuclei remain in their ground states and includes, in general, a wide range of excited states so that  $U(R, k)$  cannot be used in Eq. (12) to describe elastic scattering. The OP obtained by this method has also properties that conflict with the global systematics of nucleus-nucleus OP. Namely, its real part is quite shallow at low incident energies and becomes deeper as the energy increases [76, 77], while empirically the real nucleus-nucleus OP has been found to be deep at low energies and to become shallower as the energy increases [5]. A possible reason for this inadequacy is given below.

## 5. Nuclear rainbow and preference of a deep real OP

If the depth of the real nucleon-nucleus OP at low and medium incident energies is known to be around 40-50 MeV for a wide range of target masses, based on both the microscopic G-matrix calculations and the phenomenological OM analyses of nucleon-nucleus elastic scattering, the depth of HI optical potential has been uncertain for years. The question “Is the HI optical potential deep or shallow?” has often been one of the basic questions posed in the studies of HI scattering [5]. As discussed above in Sec. 2, the main reason that hindered our knowledge about the shape of the OP is the strong absorption which is typical for most HI systems [21], especially, those involving medium to heavy nuclei. However, the careful OM studies of rainbow scattering observed in the  $\alpha$ -nucleus [8, 10, 39] and light HI systems [5, 60] seem to show unambiguously that the physically realistic real OP must be “deep”.

Typically, the OM analyses of the elastic (refractive)  $\alpha$ -nucleus scattering data using various forms of the OP such as the standard Woods-Saxon potential [9, 10], spline functions [39] or that deduced from a model-independent analysis (MIA) of the elastic  $\alpha$ -nucleus data [78, 79], have always resulted in a weakly absorbing imaginary potential and a deep real potential which is close to that predicted by the folding model. As an illustration, Fig. 21 shows the real OP for the  $\alpha + {}^{40}\text{Ca}$  system at 104 MeV given by the



MIA using a series of Fourier-Bessel functions [78] in comparison with that predicted by the DFM using different inputs for the effective, density dependent NN interaction. It turned out that the MIA potential agrees best with the double-folded potentials given by the most realistic choice of the density dependent NN interaction (CDM3Y6 and BDM3Y1 in Table 1). This kind of comparison is very helpful for the justification of the folding model as a reliable tool to predict the real nucleus-nucleus OP. We note further that, in contrast to many cases of the elastic HI scattering, the real  $\alpha$ -nucleus OP has no “family” problem (the existence of different potential families which give nearly the same OM fit to the elastic data), especially, when the systematic behavior of the volume integral of the OP is taken into account [79].

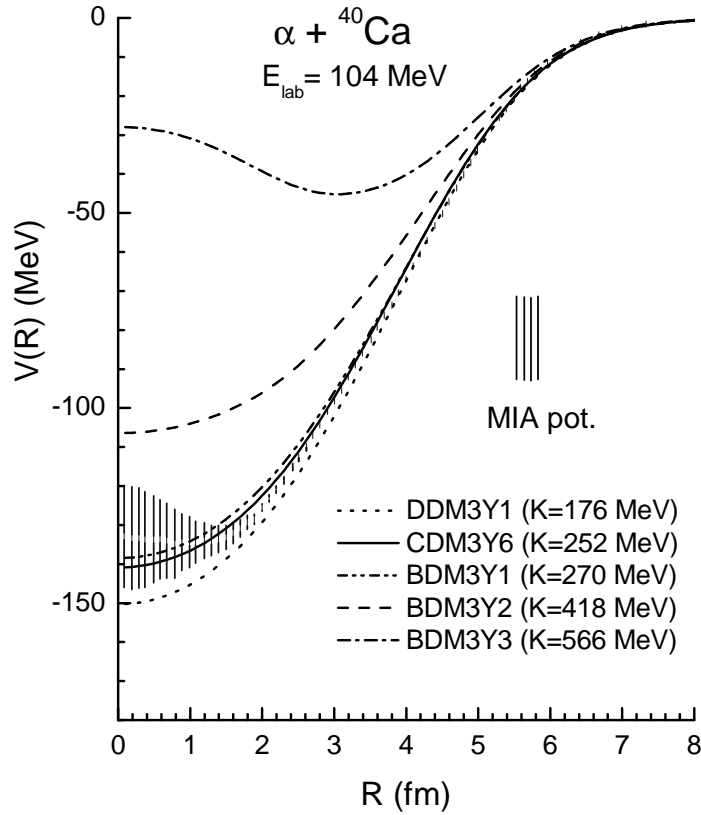


**Figure 21.** Radial shapes of the real OP for the  $\alpha+^{40}\text{Ca}$  system at 104 MeV given by a model-independent analysis (hatched area) [78] and the double-folded potentials obtained with different density dependent NN interactions (which give the corresponding values of the nuclear incompressibility  $K$  in the HF calculation of nuclear matter [58]).

Although there still exist ambiguities in the depth of HI optical potential for heavy systems due to the strong absorption, numerous OM studies of the nuclear rainbow scattering patterns observed in light HI systems like  $^{12}\text{C}+^{12}\text{C}$ ,  $^{16}\text{O}+^{12}\text{C}$  and

$^{16}\text{O}+^{16}\text{O}$  have lead to a rather unique OP systematics for these systems [4, 60]. In particular, Brandan and McVoy [60] have shown that in the “rainbow” energy range of 6 - 100 MeV/nucleon, the central depth of the real OP for light HI systems is  $V(R = 0) \approx 100 - 300$  MeV, and the ratio of the imaginary to the real parts of the OP was found to be  $W(R)/V(R) \ll 1$ , for both small and large distances  $R$  (which reflects the internal and far-tail transparency of the OP), and  $W(R)/V(R) \approx 1$  in the surface region. Such a “deep” real OP agrees closely with that predicted by the double-folding calculation [56, 57, 58]. The double-folded potential has been shown [24, 36] to give the correct order of the Airy oscillation in the observed rainbow patterns of the elastic  $^{16}\text{O}+^{16}\text{O}$  cross section. The use of a deep real OP was also found necessary to explain consistently the shape of the low-energy resonances as well as the bound  $^{12}\text{C}+^{12}\text{C}$  cluster states in  $^{24}\text{Mg}$  [80] and the  $^{16}\text{O}+^{16}\text{O}$  cluster states in  $^{32}\text{S}$  [81]. Here only the deep potential can generate the correct number of nodes for the total (antisymmetrized) wave function of the cluster state that is *not* Pauli-forbidden. Thus, a consistent description of the low-energy resonances as well as the bound cluster states has been achieved only with a deep real OP which is a continuation of the deep real OP found necessary to explain the nuclear rainbow scattering at higher energies. As a result, one can ascribe this deep potential to a *mean-field* potential [80] which is similar to the nucleon mean-field potential used in a consistent study of low-energy nucleon-nucleus elastic scattering and single-nucleon bound states [51].

The preference of a deep mean-field potential for the real nucleus-nucleus OP, whose depth and radial shape are consistent with the folding results [4, 60], has been confirmed by a detailed study of the Pauli blocking effects in the double-folding formalism by Soubbotin *et al.* [82]. The main concept of this “Pauli distorted double-folding model” (PDDFM) [82] is illustrated in upper part of Fig. 22. Namely, the overlapping of the two nuclear densities at short distances in the coordinate space is treated self-consistently by a Pauli distortion of the two corresponding Fermi spheres in the momentum space which are separated by the local relative-motion momentum. Such a treatment of the Pauli distortion of the two Fermi spheres (to prevent them from overlapping with each other) has been developed in the past by Tuebingen group [76, 77] in their study of HI collision. The only difference is that in the PDDFM the two Fermi spheres are separated by the local nucleon relative momentum  $k = K(R)/M$ , determined self-consistently by the local real OP at a given radial distance  $R$  using Eq. (24). In the nuclear matter approach [76, 77] this distance in momentum space is equal the asymptotic relative momentum at infinity  $k = K_\infty/M$ . In the spirit of the local density approximation (widely used in the NM studies of the nucleon-nucleus OP) the use of the asymptotic relative momentum for the separation between the two Fermi spheres is not appropriate and leads to a strong repulsion between the two Fermi spheres at low energies. As a result, the real nucleus-nucleus OP obtained in the NM approach is quite shallow at low energies and becomes deeper as the energy increases [76, 77], in a contradiction with the established systematics [5]. The consistent use of the local nucleon relative momentum  $k = K(R)/M$  in the PDDFM calculation of the exchange potential has confirmed [82]

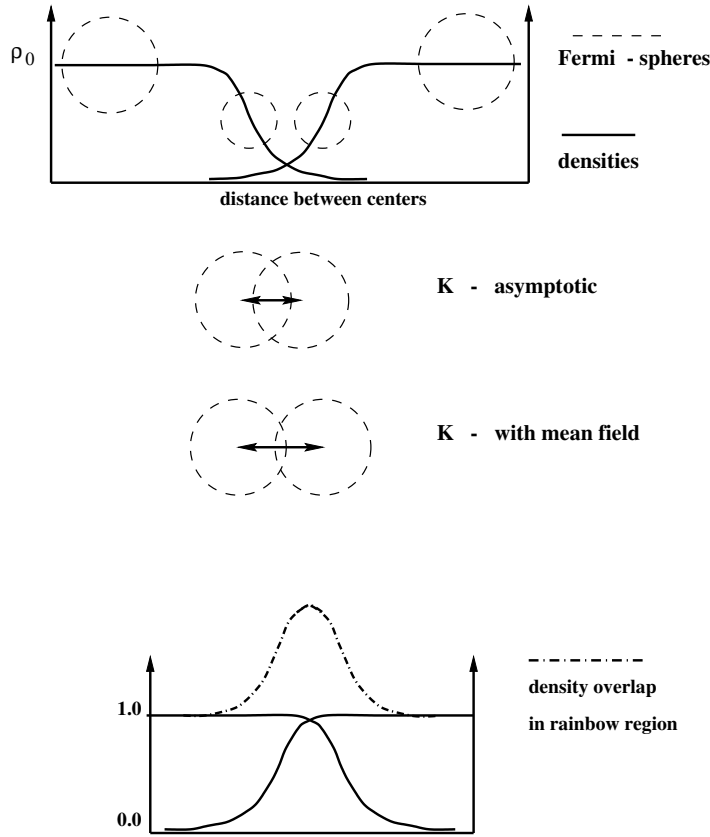


**Figure 22.** Nuclear densities of the two colliding nuclei and two corresponding Fermi spheres (dashed circles) separated by the relative-motion momentum  $K$ . If  $K$  is taken to be the local relative momentum (24) determined self-consistently by a mean-field attractive potential then it becomes larger as the potential gets deeper at low energies and, thus, suppresses the Pauli distortion of the two Fermi spheres in the momentum space [82].

the earlier prediction of the DFM [56, 57, 58] of the *mean-field* type real OP which is deep at low energies and becomes shallower with the increasing energy, as shown in Fig. 23. An attractive real OP, which is deep at small impact parameters  $R$ , generates correspondingly a large local momentum  $K(R)$  that suppresses the Pauli distortion of the two Fermi spheres in a *boot-strap* manner (see upper part of Fig. 22). Soubbotin *et al.* [82] also found that the maximal effect by the Pauli distortion appears at the sub-surface distances of 3-5 fm and it accounts, in part, for the renormalization factor of the real folded potential required by the OM fit to the elastic nucleus-nucleus scattering data. In general, the Pauli distortion [82] can lead also to the excitation of the two colliding nuclei which induces a loss of flux from the elastic channel to other channels. However, the transformation of the Pauli distortion in the momentum space into the real excitation of the two nuclei depends strongly on their internal structure, and such a Pauli excitation is expected to be less significant for a system of two strongly bound (closed-shell) nuclei. This explains again why the refractive elastic nucleus-nucleus scattering

with pronounced rainbow pattern has been observed only in the elastic scattering of the “robust”  $\alpha$ -particle and of the light HI systems involving strongly bound nuclei like  $^{12}\text{C}$  and  $^{16}\text{O}$ .

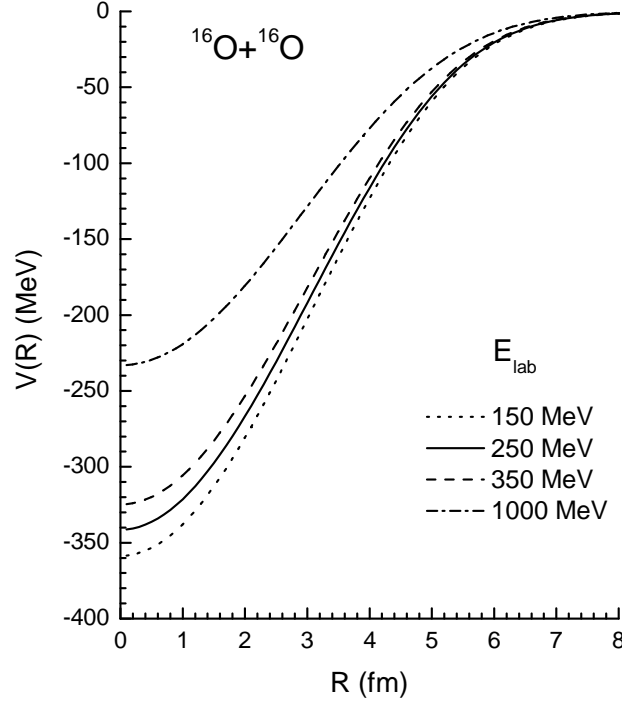


**Figure 23.** Radial shapes of the real OP for the  $^{16}\text{O}+^{16}\text{O}$  system at incident energies of 150, 250, 350 and 1000 MeV predicted by the DFM using the CDM3Y6 version (see Table 1) of the density dependent M3Y-Paris interaction [58].

Thus, the agreement of the DFM results with the global systematics for the real nucleus-nucleus OP has been shown to have a solid physical origin, which further justifies the use of the DFM to probe the effective NN interaction as well as the wave functions (or nuclear densities) of the two colliding nuclei in the folding analysis of the refractive, nuclear rainbow scattering data.

## 6. Rainbow scattering as a probe for the density dependence of in-medium NN interaction

Given correct nuclear densities as inputs for the folding calculation, it remains necessary to have an appropriate in-medium NN interaction for a reliable prediction of the (real) nucleus-nucleus OP. To evaluate an in-medium NN interaction starting from the free NN interaction still remains a challenge for the nuclear many-body theory. For example, the sophisticated Brueckner-Hartree-Fock calculations which include the two- and three-nucleon correlations cannot describe simultaneously the equilibrium density and the

binding energy of normal nuclear matter, unless the higher-order correlations as well as relativistic effects are taken into account [83]. Therefore, most of the “microscopic” nuclear reaction calculations so far still use different kinds of the effective NN interaction. Such interactions can be roughly divided into two groups. In the first group one parameterizes the effective interaction directly as a whole, like the Skyrme forces, leaving out any connection with the realistic free NN interaction. In the second group one parameterizes the effective NN interaction in a functional form, amendable to the folding calculation, based on the results of a nuclear many-body calculation using the realistic free NN potential. Very popular choices in the second group have been the so-called M3Y interactions which were designed by the MSU group to reproduce the G-matrix elements of the Reid [84] and Paris [85] free NN potentials in an oscillator basis (further referred to as M3Y-Reid and M3Y-Paris interaction, respectively). The original (spin- and isospin independent) M3Y interaction is density independent and given in terms of Yukawa functions as follows

$$\begin{aligned} \text{M3Y-Reid:} \quad v_D(s) &= 7999.0 \frac{\exp(-4s)}{4s} - 2134.25 \frac{\exp(-2.5s)}{2.5s}, \\ v_{\text{EX}}(s) &= 4631.38 \frac{\exp(-4s)}{4s} - 1787.13 \frac{\exp(-2.5s)}{2.5s} - 7.8474 \frac{\exp(-0.7072s)}{0.7072s}; \end{aligned} \quad (27)$$

$$\begin{aligned} \text{M3Y-Paris:} \quad v_D(s) &= 11061.625 \frac{\exp(-4s)}{4s} - 2537.5 \frac{\exp(-2.5s)}{2.5s}, \\ v_{\text{EX}}(s) &= -1524.25 \frac{\exp(-4s)}{4s} - 518.75 \frac{\exp(-2.5s)}{2.5s} - 7.8474 \frac{\exp(-0.7072s)}{0.7072s}. \end{aligned} \quad (28)$$

The Yukawa strengths in Eqs. (27) and (28) are given in MeV, and  $s$  is the distance between the two interacting nucleons. These interactions, especially, the M3Y-Reid version have been used with some success in the DFM calculation of the HI optical potential at low energies [21], with the elastic data usually limited to the forward scattering angles and, thus, sensitive to the OP only at the surface. However, in cases of refractive (rainbow) nucleus-nucleus scattering where the elastic data are sensitive to the nucleus-nucleus OP over a much wider radial domain as discussed above in Sect. 3, the density independent M3Y interactions failed to give a good description of the data. Namely, the folded potential is too deep at small distances  $R$  to reproduce the elastic cross sections at the large angles. A typical example is shown in Fig. 24 where the inclusion of a density dependence into the effective NN interaction was found essential to describe the rainbow “shoulder” observed in the elastic  $\alpha + {}^{58}\text{Ni}$  scattering at 139 MeV [9]. In terms of medium effects, the inclusion of an explicit density dependence was needed to account for a reduction in the strength of the nucleus-nucleus interaction that occurs at small  $R$  where the overlap density of the nuclear collision increases. An early version of the density dependence of the M3Y-Reid interaction was constructed by Kobos *et al.* [86] based upon the G-matrix results obtained by Jeukenne, Lejeune and Mahaux [52]. It was dubbed the DDM3Y interaction and has been used to improve the folding model description of the elastic  $\alpha$ -nucleus [86, 87] and light HI [88] scattering.

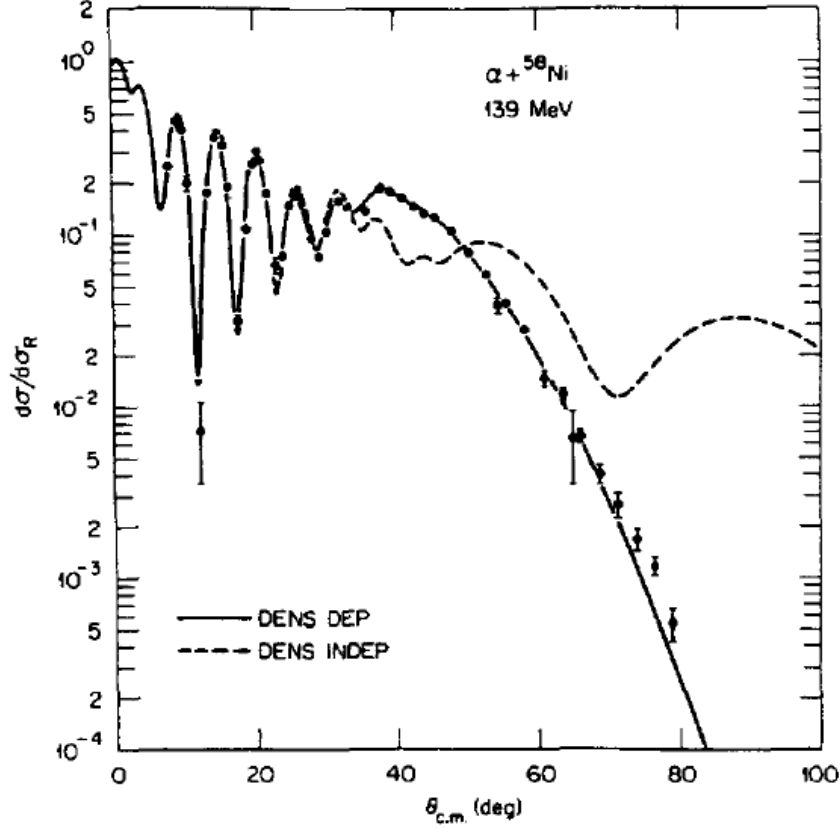


**Figure 24.** OM fits to the elastic  $\alpha + {}^{58}\text{Ni}$  scattering data at 139 MeV [9] given by the folded potential obtained with (solid curve) and without (dashed curve) density dependence of the effective NN interaction. The density dependence was empirically introduced [22] to reduce the depth of the folded potential at small distances while leaving the potential at the surface nearly unchanged. Illustration taken from Ref. [22].

### 6.1. Density dependent M3Y interaction in the Hartree-Fock calculation of nuclear matter

The physical origin of the density dependence of effective NN interaction can be very well illustrated [89] in a Hartree-Fock (HF) calculation of nuclear matter. Namely, given the direct  $v_D$  and exchange  $v_{EX}$  parts of the effective in-medium NN interaction one can easily calculate [90] the total NM binding energy

$$E = E_{kin.} + \frac{1}{2} \sum_{k\sigma\tau} \sum_{k'\sigma'\tau'} [ \langle k\sigma\tau, k'\sigma'\tau' | v_D | k\sigma\tau, k'\sigma'\tau' \rangle + \langle k\sigma\tau, k'\sigma'\tau' | v_{EX} | k'\sigma\tau, k\sigma'\tau' \rangle ] \quad (29)$$

using plane waves for  $|k\sigma\tau\rangle$ . Our HF calculation [89] of the NM energy (29) has shown that the original density independent M3Y interaction (27)-(28) failed to saturate NM,

**Table 1.** Parameters of different density dependences  $F(\rho)$ , Eq. (32), associated with the M3Y-Reid (27) and M3Y-Paris (28) interactions [84, 85]. The values of the nuclear incompressibility  $K$  were obtained from the NM binding energy using Eq. (31).

Interaction	$v_{D(\text{EX})}(s)$	$C$	$\alpha$	$\beta$ (fm <sup>3</sup> )	$\gamma$ (fm <sup>3n</sup> )	$n$	$K$ (MeV)	Ref.
DDM3Y1	Eq. (27)	0.2845	3.6391	2.9605	0.0	0	171	[89]
DDM3Y1	Eq. (28)	0.2963	3.7231	3.7384	0.0	0	176	[91]
CDM3Y1	Eq. (28)	0.3429	3.0232	3.5512	0.5	1	188	[58]
CDM3Y2	Eq. (28)	0.3346	3.0357	3.0685	1.0	1	204	[58]
CDM3Y3	Eq. (28)	0.2985	3.4528	2.6388	1.5	1	217	[58]
CDM3Y4	Eq. (28)	0.3052	3.2998	2.3180	2.0	1	228	[58]
BDM3Y1	Eq. (27)	1.2253	0.0	0.0	1.5124	1	232	[89]
CDM3Y5	Eq. (28)	0.2728	3.7367	1.8294	3.0	1	241	[58]
CDM3Y6	Eq. (28)	0.2658	3.8033	1.4099	4.0	1	252	[58]
BDM3Y1	Eq. (28)	1.2521	0.0	0.0	1.7452	1	270	[91]
BDM3Y2	Eq. (27)	1.0678	0.0	0.0	5.1069	2	354	[89]
BDM3Y2	Eq. (28)	1.0664	0.0	0.0	6.0296	2	418	[91]
BDM3Y3	Eq. (27)	1.0153	0.0	0.0	21.073	3	475	[89]
BDM3Y3	Eq. (28)	1.0045	0.0	0.0	25.115	3	566	[91]

leading to a collapse. The HF method is the first order of nuclear many-body calculation and the introduction of a density dependence into the original M3Y interaction accounts, therefore, for higher-order NN correlations which lead to the NM saturation. The earlier DDM3Y version of the density dependent M3Y-Reid interaction [86] resulted in a correct NM binding energy of around 16 MeV but at the wrong density ( $\rho_0 \simeq 0.07$  fm<sup>-3</sup> compared to the empirical saturation density of about 0.17 fm<sup>-3</sup> as shown in Fig. 1 of Ref. [89]). We have further introduced several versions of the density dependence of the M3Y-Reid and M3Y-Paris interactions [57, 89, 91] by scaling them with an explicit density dependent function  $F(\rho)$

$$v_{D(\text{EX})}(\rho, s) = F(\rho)v_{D(\text{EX})}(s), \quad (30)$$

where  $v_{D(\text{EX})}$  are the direct and exchange components of the M3Y interactions defined in Eqs. (27)-(28) and  $\rho$  is the NM density.  $F(\rho)$  was taken to be either the exponential dependence [86] or the power-law density dependence [92], and the parameters were adjusted to reproduce the observed NM saturation properties in the HF calculation (29). Although different versions of the density dependence give the same NM saturation properties, they do result in different curvatures of the NM binding energy curve near the saturation point (see Fig. 25), i.e., they are associated with different values of the NM incompressibility  $K$  which is determined as

$$K = 9\rho^2 \left. \frac{d^2[E/A]}{d\rho^2} \right|_{\rho = \rho_0}. \quad (31)$$

To have different  $K$  values in finer steps, we have introduced a hybrid of the exponential and power-law forms for  $F(\rho)$  [58] and the different density dependences of the M3Y-Reid and M3Y-Paris [58, 89, 91] can all be written in the following form

$$F(\rho) = C[1 + \alpha \exp(-\beta\rho) - \gamma\rho^n]. \quad (32)$$

The parameters  $C, \alpha, \beta, \gamma$  and  $n$  were chosen in each case to reproduce the NM saturation properties in the HF calculation (29) and they are given in Table 1. The HF results for the total NM energy obtained with several versions of the density dependent M3Y-Paris interaction are shown in Fig. 25, and one can see that different density dependences (resulting in different  $K$  values) lead to different slopes of the NM binding energy curve at high NM density, i.e., different nuclear equations of state (EOS). We note that  $F(\rho)$ , when used in the folding calculation of the real OP, needs to be scaled by an energy dependent factor,  $g(E) \approx 1 - 0.003\varepsilon$  and  $1 - 0.002\varepsilon$  for the M3Y-Paris and M3Y-Reid interaction, respectively, where  $\varepsilon$  is the bombarding energy per nucleon (in MeV). The inclusion of  $g(E)$  was found [89] necessary to account for the empirical energy dependence of the nucleon-nucleus OP.

## 6.2. Probing the nuclear EOS in the folding model analysis of refractive nucleus-nucleus scattering

One of the main goals of the study of HI collisions remains the determination of the nuclear EOS, which is important in both nuclear physics and astrophysics. Different types of the EOS are usually distinguished by different values of the nuclear incompressibility  $K$ . Many attempts in this direction have been made in the study of high-energy central HI collisions where one hopes to deduce from the measured transverse flows and particle spectra (nuclear fragments) some information on the incompressibility  $K$  of high density matter formed in the compression stage of such a reaction. Various transport models have been successfully used in reproducing such data, but in many cases the results still remain inconclusive concerning the EOS.

In general, we need a well-defined (and sensitive to  $K$ ) quantity which can be measured with high precision. We need further an effective NN interaction which reproduces, on one hand, the basic NM properties, and on the other hand, can be used as a basic input in the description of the considered experimental quantity. With this interaction one should be able to generate different  $K$  values by varying parameters of its density dependence, so that one can directly test the sensitivity of the considered quantity to the nuclear incompressibility  $K$ . It turned out that the folding model analysis of high-precision nuclear rainbow scattering data can be used as an independent method to determine the nuclear incompressibility  $K$ . This is the reason why we have parameterized several density dependences of the M3Y interaction as summarized in Table 1. In the early 80's, a very soft EOS (with  $K$  around 160 - 180 MeV) was thought to be sufficient to allow a prompt explosion in supernovae [93], but more recent numerical hydrodynamical studies indicate that this is not the case and the constraint by the observed neutron star mass requires [94, 95] higher  $K$  values around 240 MeV.



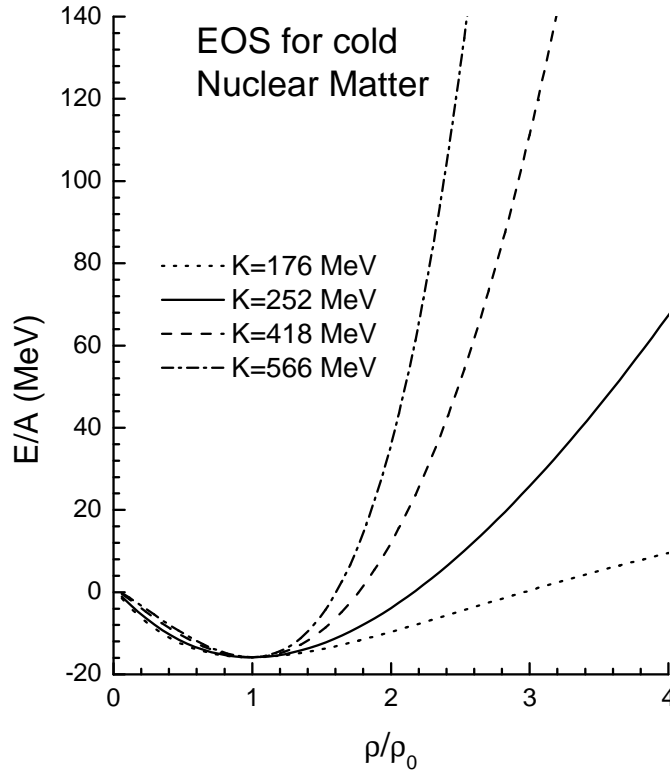


**Figure 25.** Nuclear matter binding energy as function of the NM density given by the HF calculation (29) using 4 choices of the density dependent M3Y-Paris interaction (named as DDM3Y1, CDM3Y6, BDM3Y2 and BDM3Y3 in Table 1).  $\rho_0 \approx 0.17 \text{ fm}^{-3}$  is the NM saturation density. These density dependent interactions are associated with the nuclear incompressibility  $K$  ranging from 176 to 566 MeV [57, 58].

Fig. 26 shows the mass-radius relation given by three model calculations of the neutron star which are distinguished by different values of the nuclear incompressibility  $K$  of the symmetric NM [95]. Since the neutron star mass is well constrained to around 1.5 solar mass by the observed radio pulsar masses, the realistic  $K$  values should lie within the range of 210-300 MeV as shown in Fig. 26. Some studies of high-energy central HI collisions suggest quite high  $K$  values, e.g., the determination of  $K$  based upon the production of hard photons in HI collisions has led to an estimate of  $K \approx 290 \pm 50$  MeV [96]. All this has motivated us to study in more detail the sensitivity of refractive nucleus-nucleus scattering data to the  $K$  value and, thus, to determine it with more precision by using different density dependent M3Y interactions (given in Table 1).

A typical example is presented in Fig. 27, where different density dependent M3Y-Paris interactions (which give different EOS's shown in Fig. 25) are used in the DFM to calculate the real  $^{16}\text{O}+^{16}\text{O}$  optical potential at 350 MeV. One can see that the difference in the double-folded potentials is strongest at small distances where the overlap density

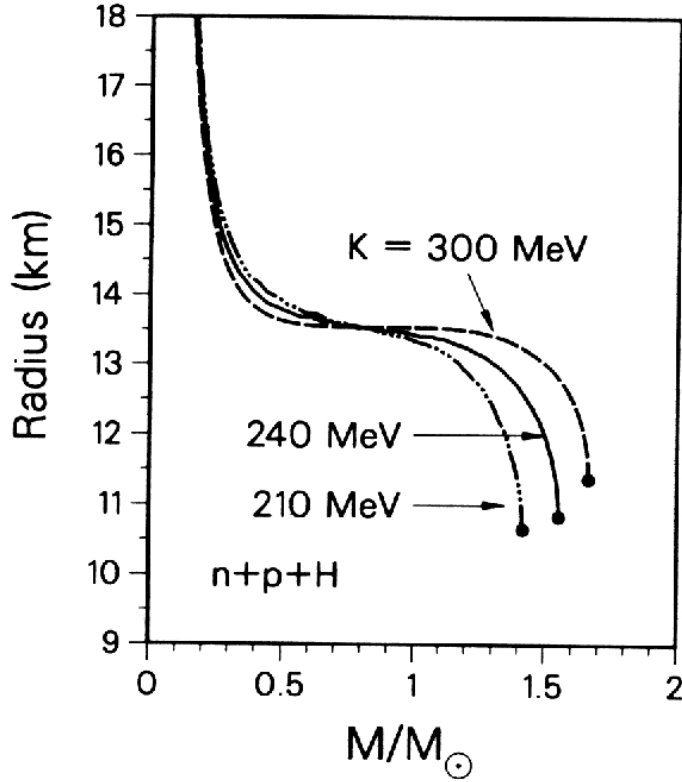


**Figure 26.** Relation between the radius and mass of the neutron star given by the EOS's corresponding to different nuclear incompressibilities  $K$ . In all cases the neutron star matter is in equilibrium between neutrons, protons, hyperons and leptons. The end point of each curve marks the final value for the neutron star radius. Illustration taken from Ref. [95].

of the  $^{16}\text{O}+^{16}\text{O}$  system is large. Since the primary rainbow pattern of the elastic  $^{16}\text{O}+^{16}\text{O}$  data at 350 MeV is quite sensitive to small partial waves, as shown in Fig. 13, these data can be used to probe the  $K$  value by using a realistic imaginary WS potential obtained from the OM systematics [24] and the real double-folded potentials given by different density dependent M3Y interactions. The corresponding OM results are shown in Fig. 28 where the CDM3Y6 interaction [58] has been found as the most favorable interaction. This version of the density dependent M3Y-Paris interaction gives  $K \approx 252$  MeV in the HF calculation of symmetric NM.

A similar (and quite unambiguous) conclusion about the realistic value of the nuclear incompressibility  $K$  has been reached in our folding analysis [58, 91] of the refractive elastic  $\alpha$ -nucleus scattering data. The weak absorption observed in the refractive  $\alpha$ -nucleus scattering at medium energies, with the appearance of the nuclear rainbow pattern, offers a unique opportunity to probe the density dependence of the effective NN interaction. A crucial point in this connection is the very high and compact density profile of the  $\alpha$  particle. Given a density as high as  $\rho \simeq 2\rho_0$  in the centre of the

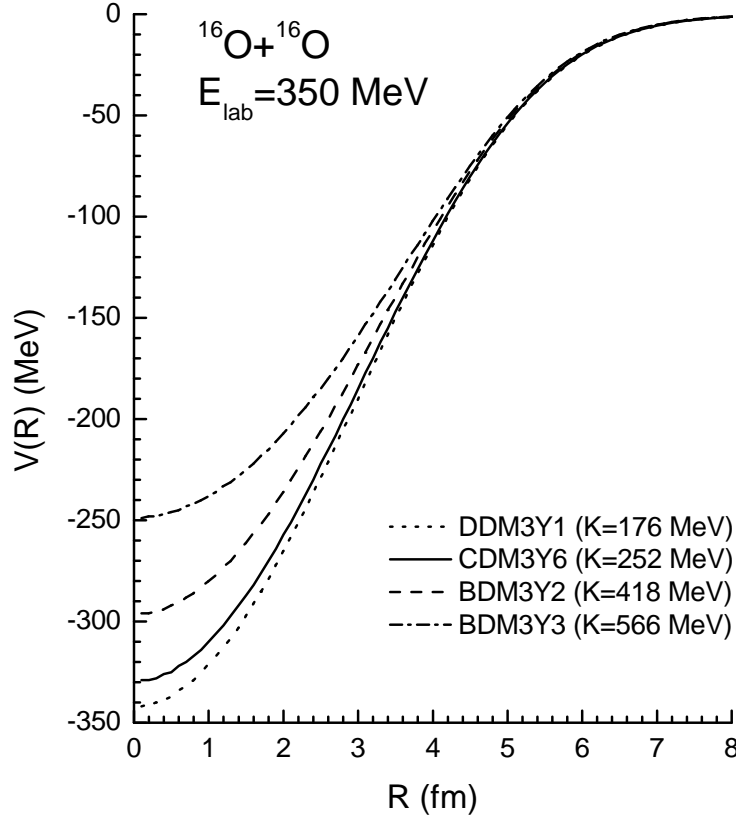


**Figure 27.** Radial shapes of the real OP for the  $^{16}\text{O}+^{16}\text{O}$  system at  $E_{\text{lab}} = 350$  MeV predicted by the DFM using the same versions of the density dependent M3Y-Paris interaction as those used in the HF calculation of NM shown in Fig. 25.

$^4\text{He}$  nucleus [97], the total density for the  $\alpha$  particle overlapping a target nucleus may reach as much as  $3\rho_0$  (as shown in Fig. 29). From Fig. 21 one can see that such a high  $\alpha+^{40}\text{Ca}$  overlap density results in a significant difference in the double-folded potential already at a separation distance of  $R = 4$  fm. The real  $\alpha$ -nucleus OP can be very well determined at such a radius if the bombarding energy is sufficiently high for the appearance of the primary rainbow maximum in the elastic cross section. The results of our folding analysis of the elastic  $\alpha+^{40}\text{Ca}$  scattering data at  $E_{\text{lab}} = 104$  [98] and 147 MeV [10] are shown in Fig. 30 where one can easily deduce the most appropriate density dependence of the M3Y-Paris interaction. The double folded  $\alpha+^{40}\text{Ca}$  potentials are compared with the real OP deduced from a model-independent Fourier-Bessel analysis in Fig. 21. One can see that the shape of the real OP is determined rather well for  $R$  down to about 2 fm. At this distance the difference between different folded potentials is so obvious that one can exclude immediately the BDM3Y2 and BDM3Y3 interactions (which give rather high  $K$  values in the HF calculation) as unrealistic ones.

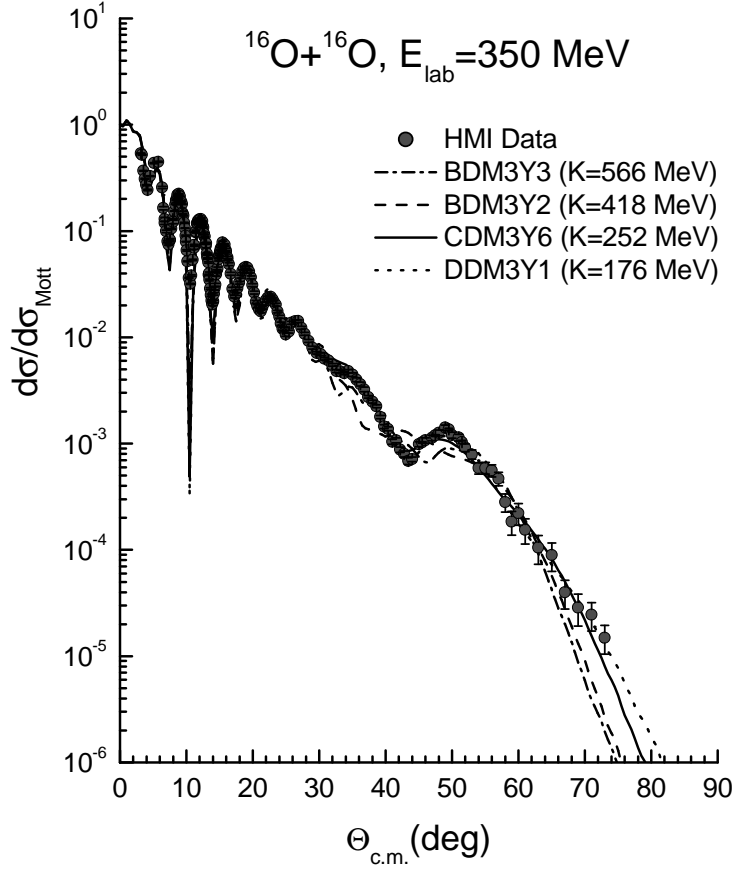


**Figure 28.** OM description of the elastic  $^{16}\text{O}+^{16}\text{O}$  scattering data at  $E_{\text{lab}} = 350$  MeV [14] given by the real folded potentials shown in Fig. 27 and an absorptive WS imaginary potential taken from Ref. [24]. The best-fit version is CDM3Y6 which gives  $K \approx 252$  MeV in the HF calculation of NM.

To validate the results presented above, it is important to discuss the approximation for the overlap density in the DFM calculation. We recall that the folding model generates the first-order term of the Feshbach optical potential (15) which is further used in the OM equation (12) to obtain the relative-motion wave function of the two nuclei remaining in their ground states. Given the antisymmetrization of the dinuclear system accurately taken into account, a reasonable approximation for the total density  $\rho$  of the two overlapping nuclei is the sum of the two g.s. densities. For example, in the calculation of the direct folded potential (21) the overlap density  $\rho$  in  $F(\rho)$  is taken as the sum of the two g.s. densities at the position of each nucleon

$$\rho_{a+A} = \rho_a(\mathbf{r}_a) + \rho_A(\mathbf{r}_A). \quad (33)$$

Such an assumption, dubbed as Frozen Density Approximation (FDA), gives naturally the overlap density  $\rho_{a+A}$  reaching up to twice the NM saturation density  $\rho_0$  at small internuclear distances. The FDA has been widely used in the folding calculations with

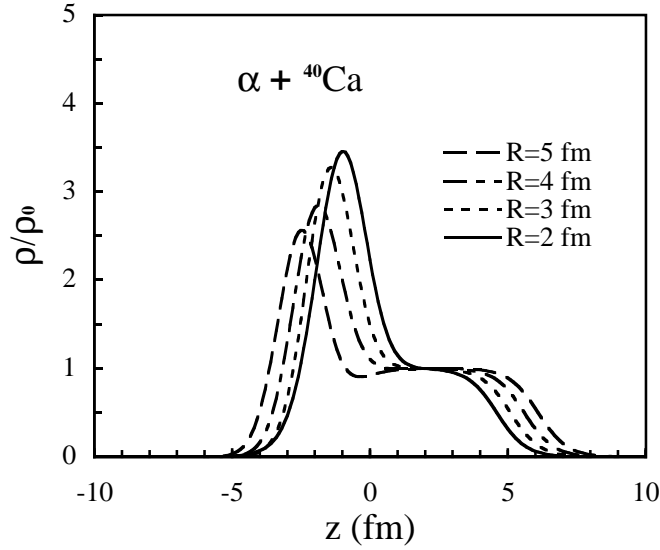


**Figure 29.** The overlap density of the  $\alpha + {}^{40}\text{Ca}$  system at different internuclear distances  $R$ . The  $z$  axis is directed along the line connecting the centres of the two nuclei. Illustration taken from Ref. [58].

density dependent NN interaction [21, 55, 86, 87, 88] for the elastic nucleus-nucleus scattering when the energy is not too low. Any density rearrangement that might happen during the collision would lead to the nuclear states different from the ground states, and thus contribute to the higher-order dynamic polarization potential  $\Delta U$  of Eq. (16). In general, the FDA reproduces very well the observed reduction of the attractive strength of the real OP at small distances, like example shown in Fig. 24. The use of FDA is, therefore, crucial for the probe of the density dependence of the effective NN interaction in the folding model analysis of refractive nucleus-nucleus scattering. We note that other approximations for  $\rho_{a+A}$ , based on the geometric or arithmetic averages of the two local densities, have also been used in the folding calculation. For example, in the JLM double-folding calculation [69] one has adopted the arithmetic average of the two densities for  $\rho_{a+A}$  to prevent it from becoming larger than  $\rho_0$ , because the JLM parameters [52] were determined for  $\rho \leq \rho_0$  only. Such an Average Density Approximation (ADA) has been carefully compared with the FDA in Ref. [66] using the density-dependent CDM3Y6 interaction, and the ADA was found not appropriate to account for the observed reduction of the real  $\alpha$ -nucleus OP at small distances. Since the ADA gives a much smaller overlap density compare to the FDA, the folding potential calculated using the ADA is more attractive and significantly deeper than that given by FDA (see Fig. 13 in Ref. [66]). One can see in Fig. 31 that the excessive depth of the double-folded potential given by the ADA results in the failure of this potential to describe the observed rainbow pattern in the elastic  $\alpha + {}^{90}\text{Zr}$  data at large angles. The use of the ADA in the JLM double-folding calculation is also the most likely reason why

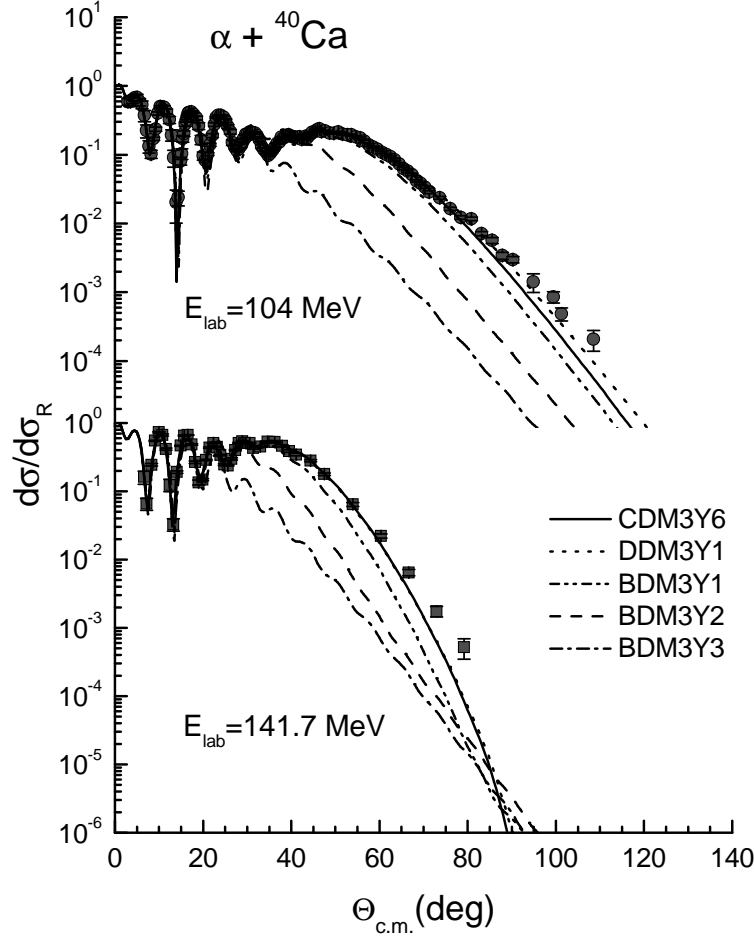


**Figure 30.** OM description of the elastic  $\alpha + {}^{40}\text{Ca}$  scattering data at  $E_{\text{lab}} = 104$  [98] and 147 MeV [10] given by the different real folded potentials shown in Fig. 21 and an imaginary WS potential determined from the OM systematics [40, 78].

the JLM folding potential fails to correctly describe the rainbow “shoulder” seen in the  ${}^6,{}^7\text{Li} + {}^{12,13}\text{C}$  elastic data at large angles (see Fig. 6 of Ref. [69]). Thus, at the “rainbow” energies, the FDA should be more appropriate for the overlap density in the double-folding calculation (21)-(23), where the exchange term is explicitly treated. A very recent double-folding analysis of the elastic  $\alpha$ -nucleus scattering using the JLM interaction by Furumoto and Sakuragi [99] has shown consistently that the renormalization factor of the real folded potential is around 0.7, a value normally observed only for a loosely bound projectile, such as  ${}^6\text{Li}$  or  ${}^{11}\text{Li}$ , but *not* for the robust  $\alpha$  particle. The geometric average used by these authors for the local density gives  $\rho_{a+A} = \sqrt{\rho_a \rho_A}$  so that the overlap density does not exceed  $\rho_0$ . As a result, the double-folded  $\alpha$ -nucleus potential is also too deep in such a “factorizing” treatment of the di-nuclear density and, hence, needs a renormalization factor significantly smaller than unity. The authors of Ref. [99] have concluded that an improvement of the parametrization for the density dependence

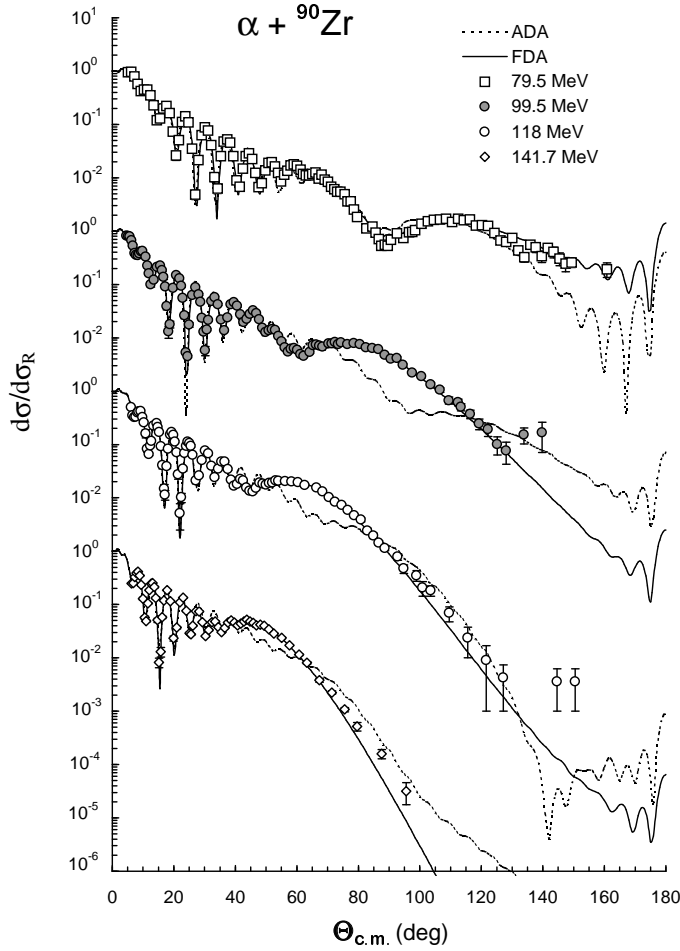


**Figure 31.** Elastic  $\alpha+^{90}\text{Zr}$  scattering data at  $E_{\text{lab}} = 79.5, 99.5, 118$  MeV [39] and 141.7 MeV [10] in comparison with the OM fits given by the CDM3Y6 double-folded potentials obtained with two different approximations for the overlap density: Average Density Approximation (dotted curves) and Frozen Density Approximation (solid curves). Illustration taken from Ref. [66].

of the JLM interaction is necessary to resolve the substantial renormalization problem in the folding analysis of the  $\alpha$ -nucleus scattering.

From a detailed folding analysis [58] of the strongly refractive  $\alpha+^{90}\text{Zr}$  rainbow scattering data [10, 39] shown in Fig. 19, we have established a systematic behavior of the  $\chi^2$  value (of the OM fit) which reaches a clear minimum with the CDM3Y5 or CDM3Y6 versions of the M3Y-Paris interaction (see Fig. 32). These density dependent M3Y-Paris interactions give values of the nuclear incompressibility with  $K \approx 241$  and 252 MeV, respectively. This result clearly indicates that a very soft EOS (with  $K$  around 180 MeV) is less realistic than a slightly stiffer EOS (with  $K \simeq 250$  MeV). To conclude this discussion, an overview of the method used to probe the nuclear incompressibility  $K$  in the folding model analysis of the refractive elastic nucleus-nucleus scattering is

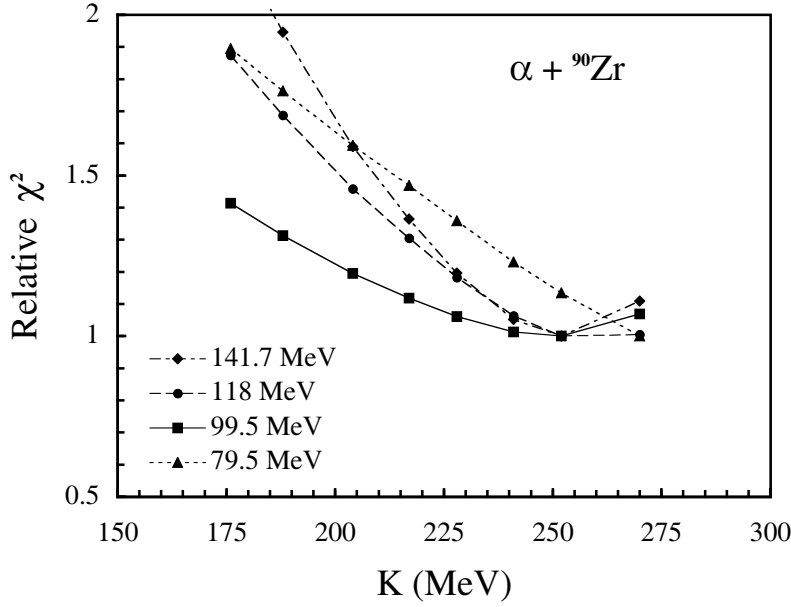


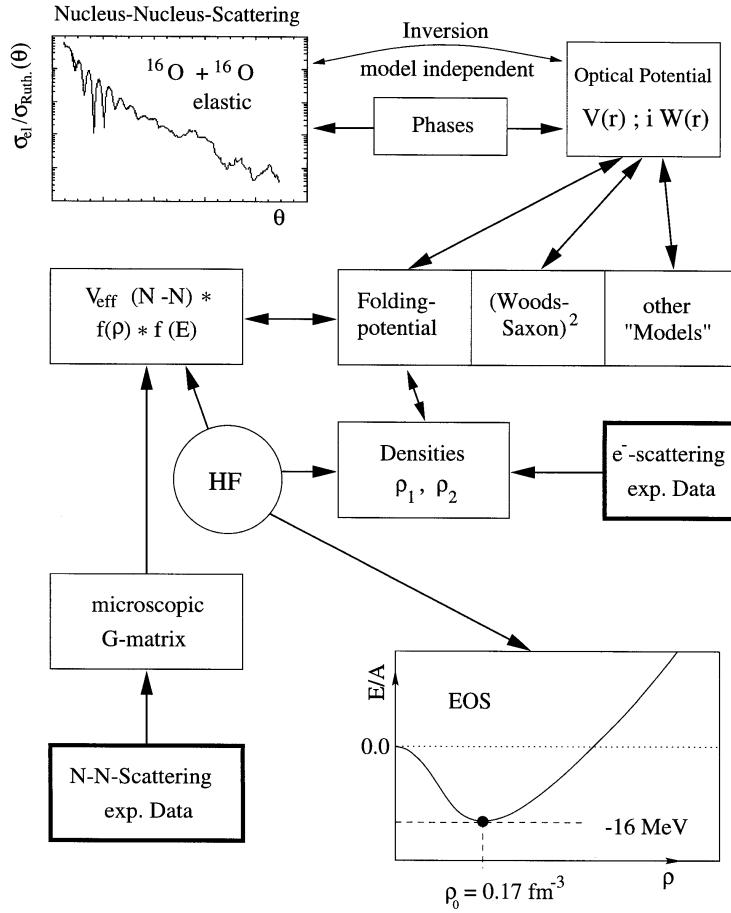
**Figure 32.** Relative  $\chi^2$  values (in ratio to the lowest  $\chi^2$  value obtained in each case) of the OM fits to the elastic  $\alpha + {}^{90}\text{Zr}$  scattering data [10, 39], versus the corresponding  $K$  values associated with the different density dependent M3Y-Paris interactions (see Table 1) used in the DFM calculation. The lines are only to guide the eye. Illustration taken from Ref. [58].

schematically illustrated in Fig. 33.

Finally, it is complementary to make a brief comment on the method to deduce the  $K$  value from the study of isoscalar giant monopole resonance (ISGMR) in medium-mass nuclei. The most recent experimental development has made it possible to measure the ISGMR energies  $E_0$  with high precision ( $\Delta E_0 \sim 0.1 - 0.3$  MeV) [100]. However, in order to deduce a realistic  $K$  value, one needs to compare the measured  $E_0$  with the ISGMR energy and strength predicted by a nuclear structure model. Due to the approximations usually made in structure calculations, one has an additional uncertainty in the calculated  $K$  value, which must be added quadratically to the experimental error [101]. Therefore, even if one uses the accurately measured  $E_0 \approx 13.96 \pm 0.20$  MeV for the ISGMR in  ${}^{208}\text{Pb}$  [100], the uncertainty in the extracted  $K$  value remains significant ( $K \approx 200 - 300$  MeV). Although a clear correlation between the ISGMR energy and  $K$  value has been well established since the original work by Blaizot *et al.* [102], until a few years ago, the extraction of  $K$  value was plagued by a critical dependence on nuclear models. Namely, the correlations between  $E_0$  and  $K$  were different for different families of functionals used in the structure calculations, like RPA based on the Skyrme or Gogny forces or the Relativistic Mean Field (RMF) calculations. Recently, it has been shown by Colò *et al.* [101] that the discrepancy between the RPA results obtained with Skyrme forces and those obtained with Gogny forces disappears if the selfconsistency



## Experimental Data



## Equation of State

**Figure 33.** The schematic link between the experimental data of elastic nucleus-nucleus scattering, nucleus-nucleus OP, nuclear densities and the effective NN interaction used in the folding calculation. Given parameters of the density dependence chosen to reproduce the NM saturation properties in the HF calculation (29), the nuclear incompressibility  $K$  (a key to specify the nuclear EOS) can be probed in the folding analysis of the *refractive* nucleus-nucleus scattering.

violation (the neglect of Coulomb and spin-orbit residual terms) is properly corrected. Then, the fully self-consistent RPA calculations based on Skyrme forces do not give  $K \approx 210 \text{ MeV}$  as quoted in Ref. [102], but predict  $K \approx 235 \text{ MeV}$  which agrees well with the RPA result obtained with Gogny forces. The  $K$  value given by the RPA calculations is slightly lower than that given by the relativistic RMF calculations [103], which predict  $K \approx 250 - 270 \text{ MeV}$ . Such a difference is now also understood as caused by different behaviors of the symmetry energy within these models [104, 105, 106]. Guided by realistic physics inputs, one can deduce from these structure calculation, that  $K \approx 240 \pm 20 \text{ MeV}$ , which is very close to that deduced from the folding model

studies of the  $\alpha$ -nucleus and nucleus-nucleus rainbow scattering (see Fig. 32).

## 7. Rainbow features in other quasi-elastic scattering channels

Although the nuclear rainbow pattern has been observed mainly in the elastic, refractive nucleus-nucleus scattering, it was natural to expect that rainbow features appear also in other quasi-elastic reactions like the inelastic scattering, nucleon transfer and charge exchange channels. In general, due to a stronger absorption, these non-elastic rainbow

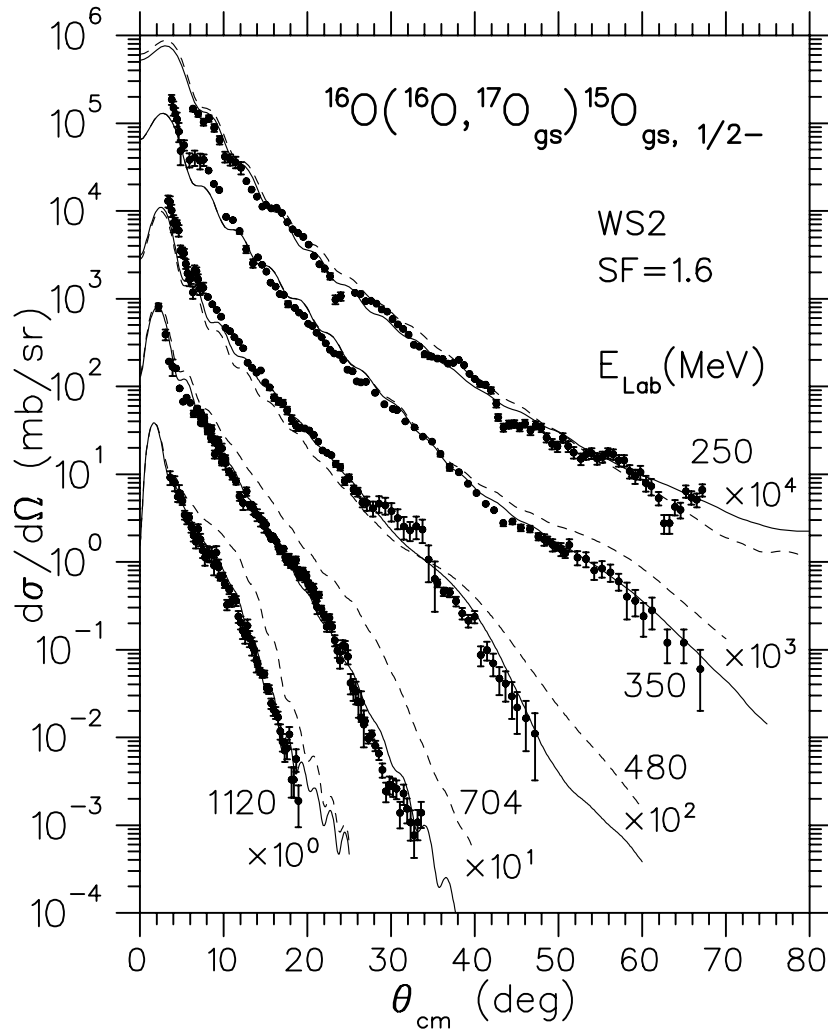


**Figure 34.** Results of the DWBA calculation for the  $^{16}\text{O}(^{16}\text{O}, ^{17}\text{O})^{15}\text{O}_{\text{gs}, 1/2-}$  one-neutron transfer reaction to the  $^{15}\text{O}_{1/2-}$  ground state at  $E_{\text{lab}} = 250 \rightarrow 1120$  MeV in comparison with the data [108]. The dashed curves were obtained with the same complex OP for the entrance  $^{16}\text{O}+^{16}\text{O}$  channel as that used for the entrance  $^{16}\text{O}+^{16}\text{O}$  channel. The solid curves were obtained with a more absorptive OP in the  $^{17}\text{O}+^{15}\text{O}$  exit channel. Illustration taken from Ref. [108]

patterns (which have no counterparts in the optical rainbow) should be less pronounced and harder to observe experimentally. The rainbow effects have been investigated, e.g.,

in the inelastic scattering and one-neutron transfer reactions measured with  $^{12,13}\text{C}+^{12}\text{C}$  systems at the energy of 20 MeV/nucleon [13]. While the refractive effects were found much weaker in the inelastic  $^{12,13}\text{C}+^{12}\text{C}$  scattering, some remnant of the nuclear rainbow has been identified in the one-neutron transfer  $^{12}\text{C}(^{12}\text{C},^{13}\text{C})^{11}\text{C}$  channel [13]. These

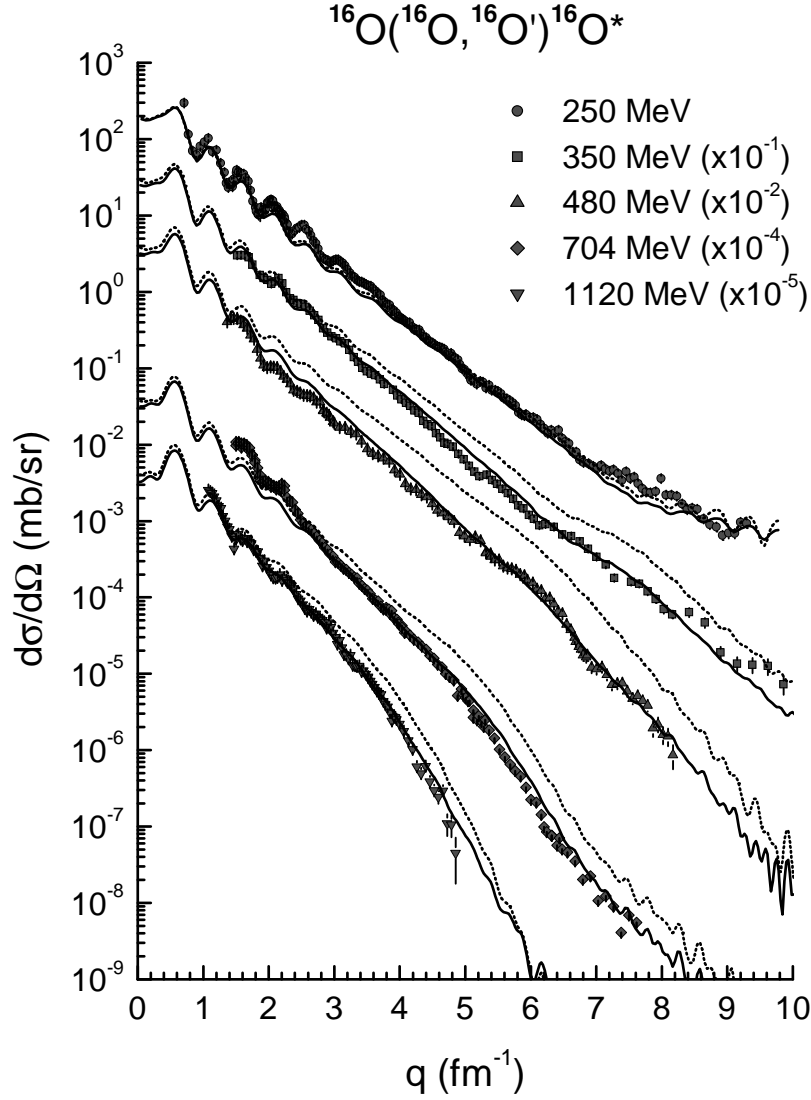


**Figure 35.** The DWBA description of the total ( $2^+ + 3^-$ ) inelastic  $^{16}\text{O}(^{16}\text{O}, ^{16}\text{O}')^{16}\text{O}^*$  scattering data at  $E_{\text{lab}} = 250 - 1120$  MeV given by the real folded form factors [109]. The dotted curves were obtained with the same complex OP for the entrance and exit channels, and the solid curves were obtained with a more absorptive OP in the exit channels. The cross sections are plotted versus the momentum transfer  $q = 2k \sin(\Theta_{\text{c.m.}}/2)$ , where  $k$  is the wave number of the projectile. Illustration taken from Ref. [109]

refractive one-neutron transfer data were shown by Satchler [107] to be rather sensitive to the shape of OP used in the transfer calculation and could be used, therefore, to

reduce the OP ambiguities for the  $^{12}\text{C}+^{12}\text{C}$  system.

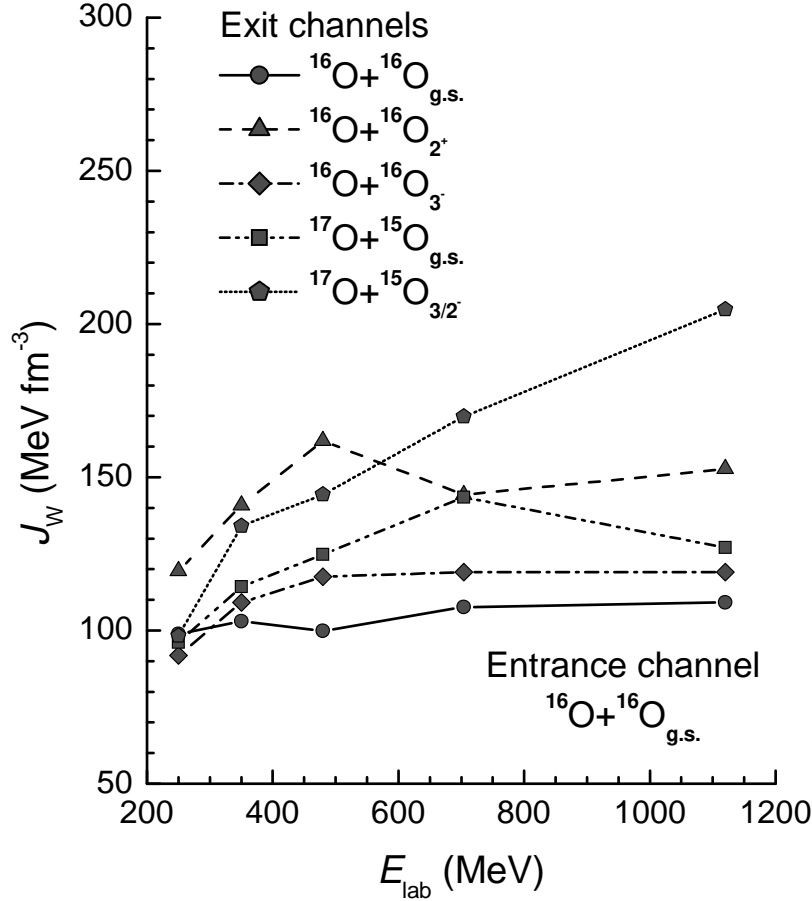


**Figure 36.** Energy dependence of the volume integral  $J_W$  per interacting nucleon pair (see Eq. (17) in Ref. [24]) of the best-fit WS imaginary OP for the entrance channel  $^{16}\text{O}+^{16}\text{O}$  and exit channels of inelastic scattering  $^{16}\text{O}+^{16}\text{O}_{2^+}$  and  $^{16}\text{O}+^{16}\text{O}_{3^-}$  and of one-neutron transfer to the ground state  $^{15}\text{O}_{\text{g.s.}}$  and excited state  $^{15}\text{O}_{3/2^-}$ . The lines are only to guide the eye. Illustration taken from Ref. [109]

With the strong nuclear rainbow pattern observed in the elastic  $^{16}\text{O}+^{16}\text{O}$  scattering [24], the one-neutron pickup  $\phi 17\text{o}15$  reaction has been measured, in parallel with the elastic  $^{16}\text{O}+^{16}\text{O}$  scattering, at the energies  $E_{\text{lab}} = 250 \rightarrow 1120$  MeV [14, 15, 16, 37]. These data were obtained for the transitions to  $^{15}\text{O}$  in the  $1p_{1/2}$  ground state and in the  $1p_{3/2}$  excited state at 6.176 MeV, with  $^{17}\text{O}$  remaining in the  $1d_{5/2}$  ground state in both cases. A detailed analysis [108] of the  $\phi 17\text{o}15$  data based on the full finite-range distorted wave Born approximation (DWBA) has found a clear remnant of the nuclear rainbow in the  $\phi 17\text{o}15$  transfer channel to the g.s. state  $^{15}\text{O}_{1/2^-}$ , especially at the rainbow energy of 350 MeV (see Fig. 34). This rainbow remnant is, however, suppressed in the transfer channel to the excited state  $^{15}\text{O}_{3/2^-}^*$  due to a much stronger absorption

in the  $^{17}\text{O}+^{15}\text{O}^*$  exit channel. Beside the elastic scattering and transfer channels, the inelastic  $^{16}\text{O}(^{16}\text{O}, ^{16}\text{O}')^{16}\text{O}^*$  scattering has also been measured at  $E_{\text{lab}} = 250 \rightarrow 1120$  MeV and the data were analyzed [109] in the DWBA using the OP and inelastic form factor given by the folding model [55]. Although the refractive pattern of the inelastic  $^{16}\text{O}(^{16}\text{O}, ^{16}\text{O}')^{16}\text{O}^*$  scattering was found to be much weaker compared to that observed in the elastic scattering channel, the remnant of the rainbow could still be traced in the inelastic scattering cross section up to  $E_{\text{lab}} = 704$  MeV (see Fig. 35).

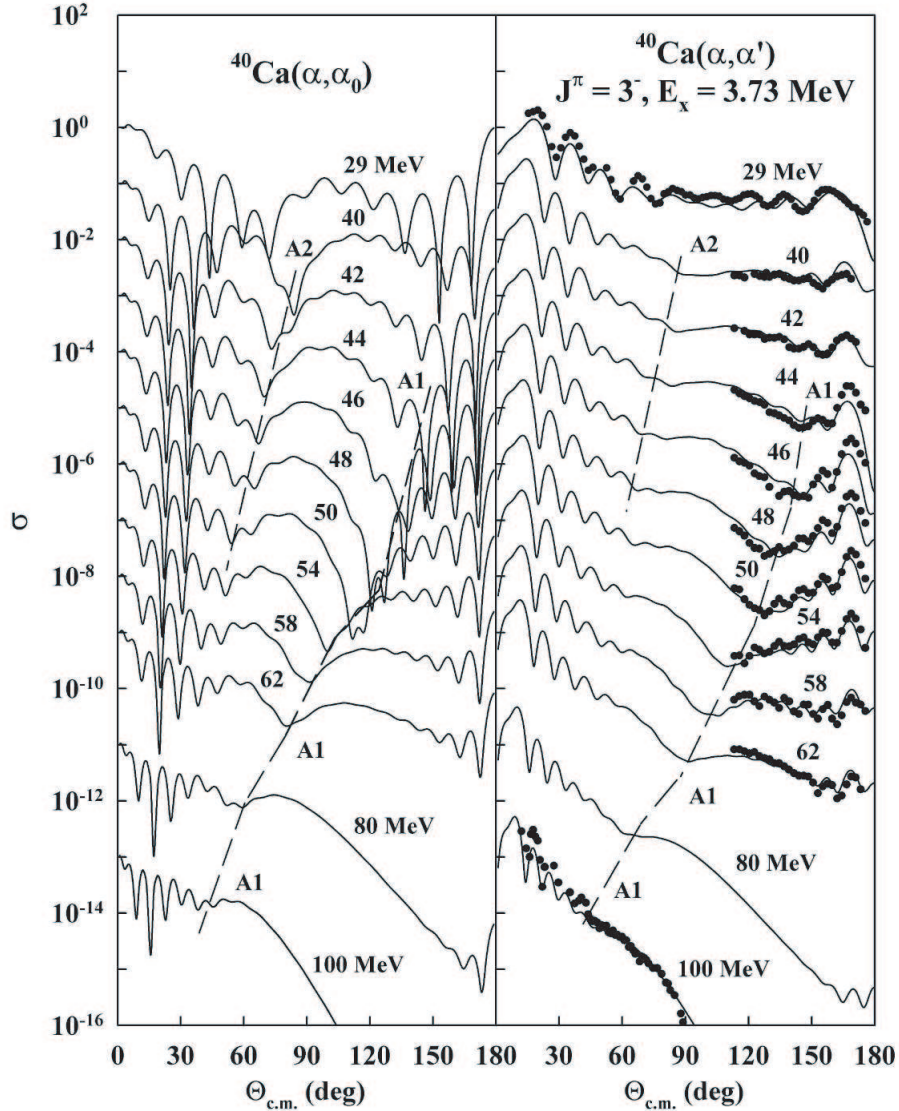


**Figure 37.** The OM and DWBA results for the elastic (left) and inelastic ( $J^\pi = 3^-, E_x = 3.73$  MeV, right)  $\alpha+^{40}\text{Ca}$  scattering, respectively, at the incident energies between 28 MeV and 100 MeV. The dashed lines show the evolution of first (A1) and second (A2) Airy minima. Illustration taken from Ref. [111].

The weaker rainbow pattern found in the inelastic  $^{16}\text{O}+^{16}\text{O}$  scattering and  $\phi^{17}\text{O}15$  transfer reaction is due to the enhanced absorptions in the exit channels [109]. Namely,

the DWBA description of the inelastic data covering a large angular range and about 6 orders of the cross-section magnitude required consistently an increased absorption in the exit channels of the inelastic scattering and transfer reaction (see Fig. 36). This important result indicates the need to have a realistic choice for the OP not only in the entrance but also in the exit channel. The use of the same complex OP in both the entrance and exit channels might lead to a large uncertainty in the deduced transition strength if one follows the standard method of scaling the inelastic FF to match the DWBA results to the measured angular distributions. This effect should be essential in the study of the quasi-elastic nucleus-nucleus scattering induced by unstable nuclei, where the partitions in the entrance and exit channels are very differently bound.

Given the broad rainbow “shoulder” clearly observed in the elastic  $\alpha$ -nucleus scattering at refractive energies as discussed in Sec. 3, its remnant was seen also in the inelastic  $\alpha$ -nucleus scattering at similar energies [110]. Recently, it has been shown by Michel and Ohkubo [111, 112] that the Airy structure of the nuclear rainbow in the inelastic  $\alpha$ -nucleus scattering is caused by the same interference mechanism as that established for the elastic  $\alpha$ -nucleus scattering. For example, from the OM and DWBA results for the elastic and inelastic  $\alpha+^{40}\text{Ca}$  scattering at different energies shown in Fig. 37, one can see the evolution of the first Airy minimum (A1) in the measured inelastic scattering cross sections at 44 to 50 MeV. As in the elastic case, the inelastic scattering amplitude can also be decomposed into the internal-wave and the barrier-wave components which lead essentially to the same Airy interference pattern as that found in the elastic scattering. Note that at each energy, the inelastic Airy minimum shows up at a slightly larger angle than its elastic counterpart, due to the energy loss to the excitation of the target state (compare locations of the Airy minima in the left and right panels of Fig. 37).

Inelastic  $\alpha$ -nucleus rainbow scattering can also be used to study the  $\alpha$ -particle condensation of nuclei. For example, the  $0^+$  (7.65 MeV) state of  $^{12}\text{C}$ , the famous Hoyle state in the nucleosynthesis of Carbon, has a dilute three- $\alpha$  cluster structure which has been discussed to be an  $\alpha$ -condensate state [113, 114]. This dilute structure has been shown to lead to a more pronounced Airy structure (with a higher-order Airy minimum) in the cross section of inelastic  $\alpha+^{12}\text{C}$  scattering at  $E_{\text{lab}} = 140$  to 240 MeV [115] compared to that in the elastic  $\alpha+^{12}\text{C}$  scattering at the same energies. Such effect is a strong indication that the refraction caused by a big volume of the dilute  $0^+$  state is stronger than that caused by the compact ground state of  $^{12}\text{C}$ , as illustrated in Fig. 38.

Finally, we note that the rainbow-like structure has also been observed in the charge exchange reactions, like  $(^6\text{Li}, ^6\text{He})$  at  $E_{\text{lab}} = 93$  MeV [116],  $(^3\text{He}, t)$  at  $E_{\text{lab}} = 38$  and 60 MeV [117, 118]. However, there has been no systematic study of the evolution of the rainbow pattern with the incident energies as was done for the elastic, inelastic scattering and one-neutron transfer reaction measured with the  $^{16}\text{O}+^{16}\text{O}$  system as discussed above. It is, therefore, highly desirable to have more measurements of the charge exchange reactions at refractive energies in order to have a complete understanding

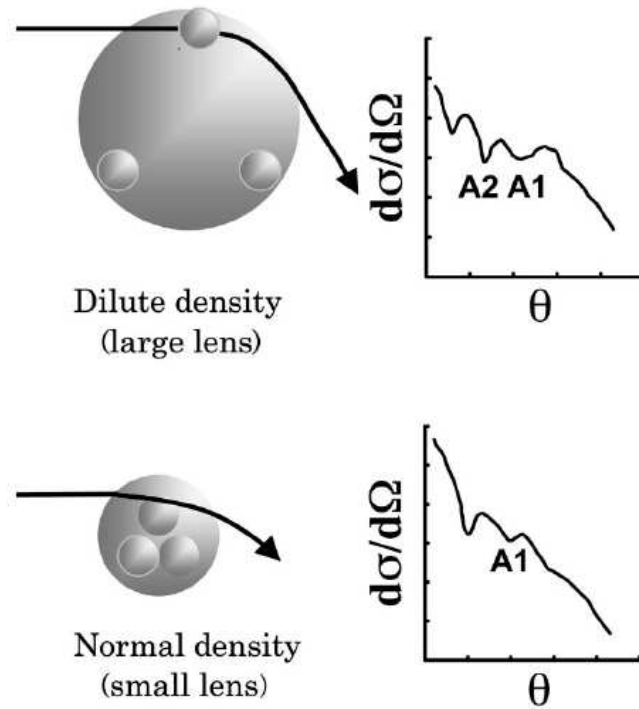


**Figure 38.** Refraction in the  $\alpha + {}^{12}\text{C}$  rainbow scattering from the ground state (small lens) and the  $0^+$  (7.65 MeV) state (large lens) and the resulting Airy structures in the angular distributions. Illustration taken from Ref. [115].

of the nuclear rainbow structure in the quasi-elastic nuclear scattering.

## 8. Nuclear rainbow scattering studies with the loosely-bound and/or unstable nuclei

In general, the absorption becomes stronger for the loosely bound and/or unstable nuclei and the rainbow-like structure is suppressed and harder to observe. There are, however, interesting exceptions observed for the loosely bound  ${}^6,7\text{Li}$  and  ${}^9\text{Be}$  nuclei for which the rainbow pattern (or its remnant) has been observed in the elastic scattering as discussed in Sec. 3. It has been shown for the  ${}^6\text{Li} + {}^{12}\text{C}$  system [50] that even after the contribution of the dynamic polarization potential caused by the breakup of  ${}^6\text{Li}$  [49] is taken into account (which significantly reduced the attractive strength of the real OP at the surface) the total  ${}^6\text{Li} + {}^{12}\text{C}$  optical potential still remains strongly refractive and can give rise to the nuclear rainbow pattern in the elastic scattering. One can see from the nearside/farside decomposition of the elastic  ${}^6\text{Li} + {}^{12}\text{C}$  scattering amplitude [50] shown in Fig. 39 that the  ${}^6\text{Li} + {}^{12}\text{C}$  system is indeed strongly refractive, with a dominant farside (rainbow) scattering contribution at the large angles.

Recently, the elastic  ${}^6,7\text{Li}$  scattering has been shown to have the Airy structure

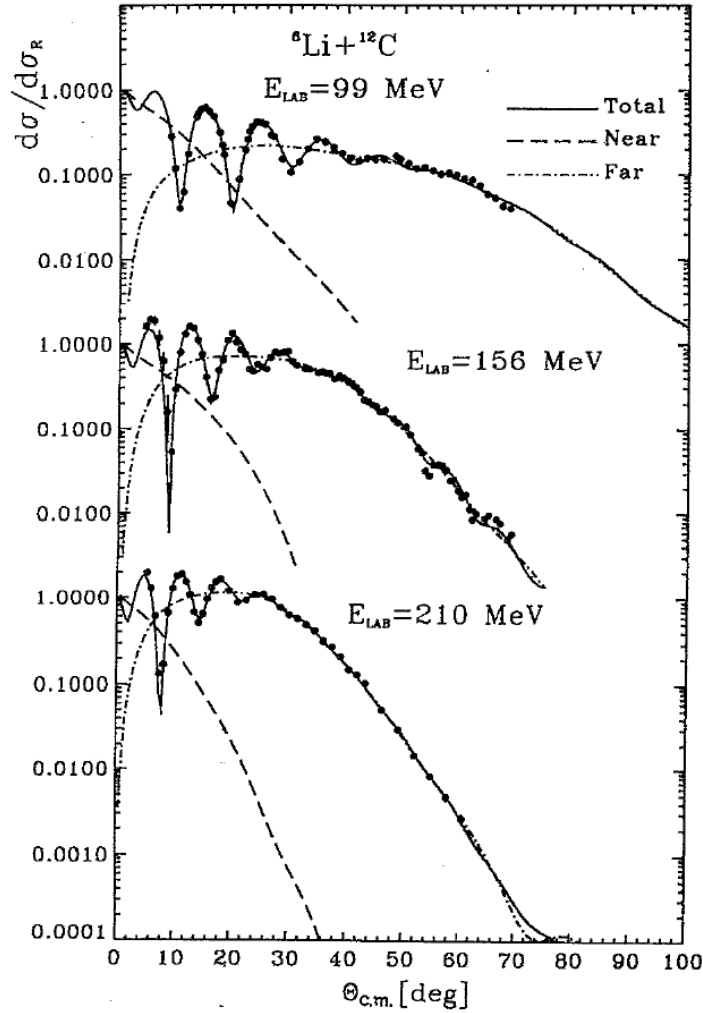


**Figure 39.** Decomposition of the elastic  ${}^6\text{Li}+{}^{12}\text{C}$  scattering cross section (solid curves) at  $E_{\text{lab}} = 99, 156$  and  $210$  MeV [50] into the nearside (dashed curves) and farside (dash-dotted curves) components using Fuller's method [26]. The dynamic polarization contribution from the breakup of  ${}^6\text{Li}$  projectile to the OP was explicitly taken into account by a spline potential. Illustration taken from Ref. [50].

very similar to that observed in the  $\alpha+{}^{40}\text{Ca}$  and  ${}^{16}\text{O}+{}^{16}\text{O}$  elastic scattering [119]. In Fig. 40 the angular locations of the Airy minima in the elastic  ${}^6\text{Li}+{}^{12}\text{C}$  scattering at different energies is compared with those found in the elastic  $\alpha+{}^{16}\text{O}$  scattering. One can see that these two systems have rather similar behaviors of the Airy minima, although for the former the DPP caused by the breakup has reduced significantly the attractive strength of the real OP at the surface and sub-surface distances [50]. A strong refractive behavior has also been established by Carstoiu *et al.* [120] in the large-angle elastic  ${}^{6,7}\text{Li}$  scattering from  ${}^9\text{Be}$  and  ${}^{12,13}\text{C}$  targets. All this suggests that the refractive effect seen in elastic  ${}^{6,7}\text{Li}$  scattering is not accidental and the most likely explanation is that these projectiles have a well established  $\alpha$ -cluster structure ( $\alpha + d$  and  $\alpha + t$  for  ${}^6\text{Li}$  and  ${}^7\text{Li}$ ,



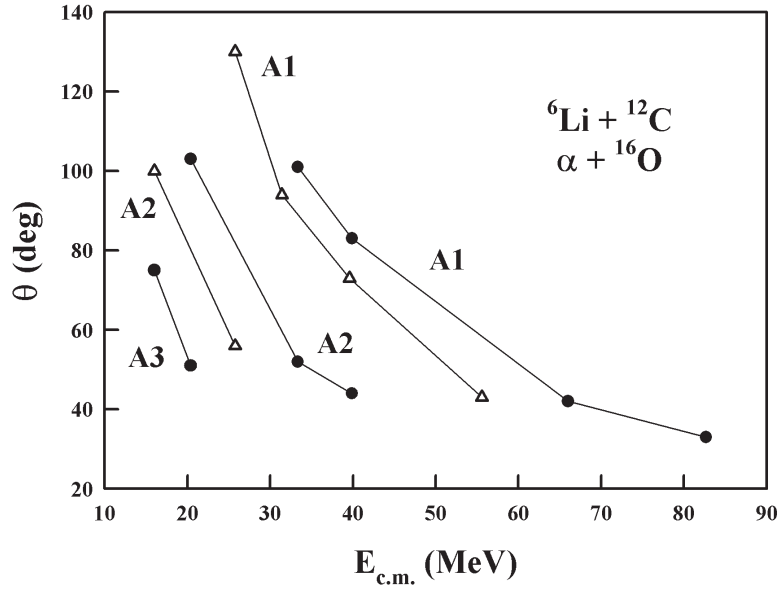


**Figure 40.** Energy dependence of the Airy minima location found in the  ${}^6\text{Li}+{}^{12}\text{C}$  (dots) and  $\alpha+{}^{16}\text{O}$  (triangles) elastic angular distributions. A1, A2 and A3 are the first, second and third Airy minima, respectively. Illustration taken from Ref. [119].

respectively). The observed refractive pattern is probably due to a strong contribution by the  $\alpha$ -core during the scattering process, and an explicit three-body solution for the elastic  ${}^6,{}^7\text{Li}$  scattering should give a more definitive conclusion on the role of the  $\alpha$ -core.

${}^6\text{He}$  is one of the most studied unstable nuclei and it also has a well established  $\alpha$ -cluster structure ( $\alpha$ -core +  $2n$ -halo). Therefore, the similarity between the recently measured elastic  ${}^6\text{He}+{}^{12}\text{C}$  scattering data at  $E_{\text{lab}} = 18$  MeV by Milin *et al.* [121] and elastic  ${}^6\text{Li}+{}^{12}\text{C}$  scattering data at about the same energy is very interesting (see Fig. 41). The fact that the same nuclear OP gives reasonable description to both the  ${}^6\text{He}+{}^{12}\text{C}$  and  ${}^6\text{Li}+{}^{12}\text{C}$  elastic scattering indicates that the contribution by the  $\alpha$  core is nearly the same in both cases with a small shift in the elastic cross section (obviously caused by the difference between the  $2n$ -halo and deuteron state, and that between the two Coulomb potentials). The elastic  ${}^6\text{He}+{}^{12}\text{C}$  scattering at 38.3 MeV/nucleon has also been measured at GANIL by Lapoux *et al.* [122], but the data cover mainly the forward angles. Nevertheless, a similarity between the  ${}^6\text{He}+{}^{12}\text{C}$  and  ${}^6\text{Li}+{}^{12}\text{C}$  elastic scattering at this medium energy was found and the same realistic  $\alpha+{}^{12}\text{C}$  potential has been used successfully in both cases to estimate the DPP caused by the breakup of  ${}^6\text{He}$  and  ${}^6\text{Li}$  [122]. All this suggests that the  ${}^6\text{He}+{}^{12}\text{C}$  system should be also strongly refractive with a significant farside (or internal-wave) contribution at large scattering angles. The future measurement to find the rainbow structure in the elastic  ${}^6\text{He}+{}^{12}\text{C}$  and/or  ${}^6\text{He}+{}^{16}\text{O}$  scattering would be very helpful, not only to give more information on the nuclear rainbow but also provide valuable scattering data to further probe the

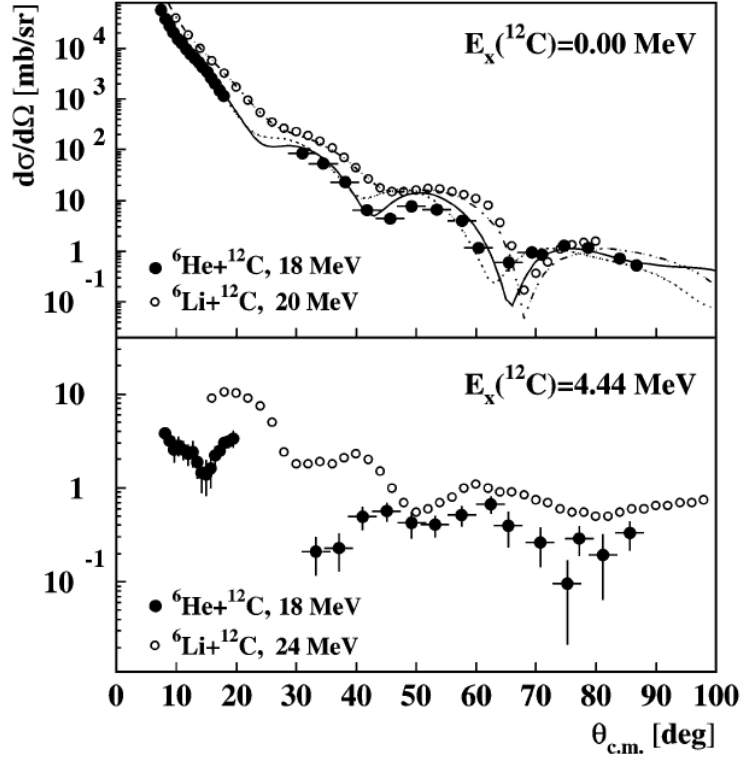


**Figure 41.** The  ${}^6\text{He}+{}^{12}\text{C}$  elastic and inelastic angular distributions measured at  $E_{\text{lab}} = 18$  MeV [121] compared to the  ${}^6\text{Li}+{}^{12}\text{C}$  elastic data at 20 MeV and inelastic data at 24 MeV. The dash-dotted curve shows the OM description of the elastic  ${}^6\text{Li}+{}^{12}\text{C}$  scattering using the same nuclear OP as that used for the  ${}^6\text{He}+{}^{12}\text{C}$  system (full curve). Illustration taken from Ref. [121].

$2n$ -halo wave function of this Borromean nucleus.

The unstable  ${}^{11}\text{Li}$  nucleus has also been studied extensively during the last two decades. Given the fact that light HI systems like  ${}^{12}\text{C}+{}^{12}\text{C}$  or  ${}^{16}\text{O}+{}^{16}\text{O}$  show strong refractive effects as discussed above, the  ${}^6\text{Li}+{}^{12}\text{C}$  system was considered as the most likely case where the refractive rainbow pattern might show up in the elastic scattering. Such refractive scattering data, if measured accurately, could allow one to probe the halo structure ( ${}^9\text{Li}$ -core +  $2n$ -halo) of  ${}^{11}\text{Li}$  in details. Short after some exploratory, theoretical studies were made for the  ${}^{11}\text{Li}+{}^{12}\text{C}$  elastic scattering [123, 124], the measurement of quasi-elastic scattering of  ${}^{11}\text{Li}$  and  ${}^{11}\text{C}$  from the  ${}^{12}\text{C}$  target at  $E_{\text{lab}} = 637$  and 620 MeV, respectively, has been performed by Kolata *et al.* [125]. Although the enhanced refraction predicted by Satchler *et al.* [123] for the  ${}^{11}\text{Li}+{}^{12}\text{C}$  system has been confirmed, no evidence was found for an Airy minimum in the farside scattering [125]. These interesting data have inspired number of OM analyses [126, 127, 128, 129, 130] as well as the few-body calculations [131, 132] which treated explicitly the projectile breakup  ${}^{11}\text{Li} \rightarrow {}^9\text{Li}+2n$ . Since the experimental energy resolution [125] did not allow for the separation of the true elastic scattering from inelastic scattering to the low-lying excited

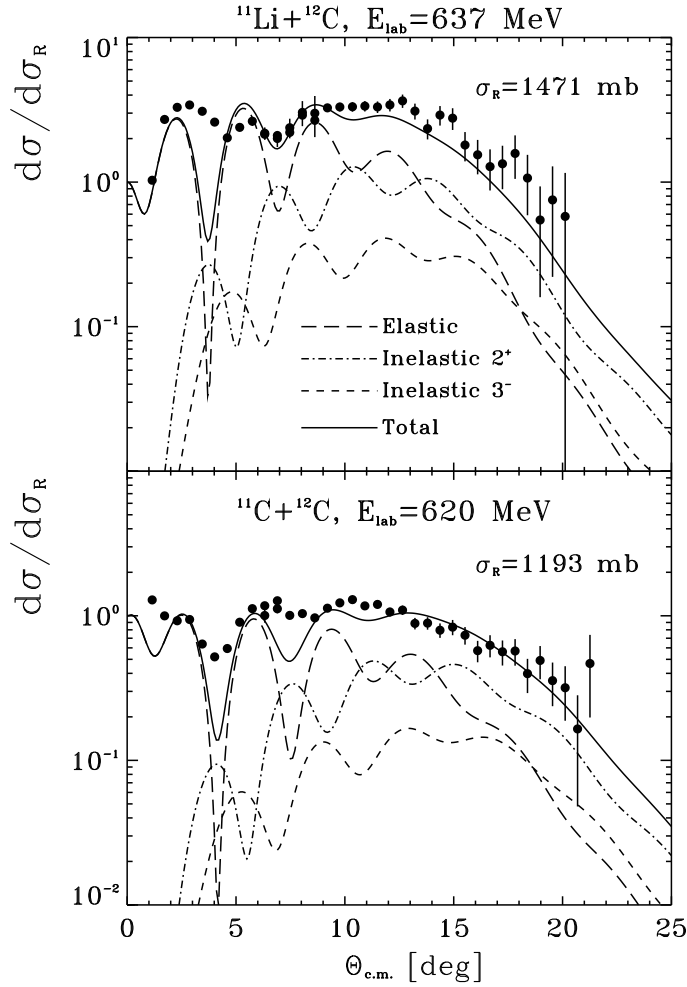


**Figure 42.** Total, elastic and inelastic scattering cross sections given by the semi-microscopic DWBA calculation [127] compared with the quasi-elastic data [125] for the  $^{11}\text{Li}+^{12}\text{C}$  system at  $E_{\text{lab}} = 637$  MeV and  $^{11}\text{C}+^{12}\text{C}$  system at 620 MeV. The  $^{11}\text{Li}+^{12}\text{C}$  optical potential was added by a (complex) dynamic polarization potential to account for the breakup of  $^{11}\text{Li}$  projectile. Illustration taken from Ref. [127].

states, one usually adds the cross sections of inelastic scattering to the lowest  $2^+$  and  $3^-$  states of  $^{12}\text{C}$  to the elastic scattering cross section for a direct comparison with the data. For example, our DWBA analysis [127] of the elastic and inelastic scattering of  $^{11}\text{Li}$  and  $^{11}\text{C}$  from  $^{12}\text{C}$ , using the semi-microscopic OP added by a realistic DPP to account for the breakup effect, has given a good description of both the quasi-elastic scattering data and total reaction cross section (see Fig. 42). However, most of the OM analyses of the elastic  $^{11}\text{Li}+^{12}\text{C}$  scattering  $E_{\text{lab}} = 637$  MeV predict a deep nearside/farside interference minimum at forward angles (see upper part of Fig. 42) which is absent in the measured angular distribution [125]. Since this interference minimum has been observed in experiment [125] for the  $^{11}\text{C}+^{12}\text{C}$  system (lower part of Fig. 42), a question arises whether the absence of this minimum in the  $^{11}\text{Li}+^{12}\text{C}$  case is an effect due

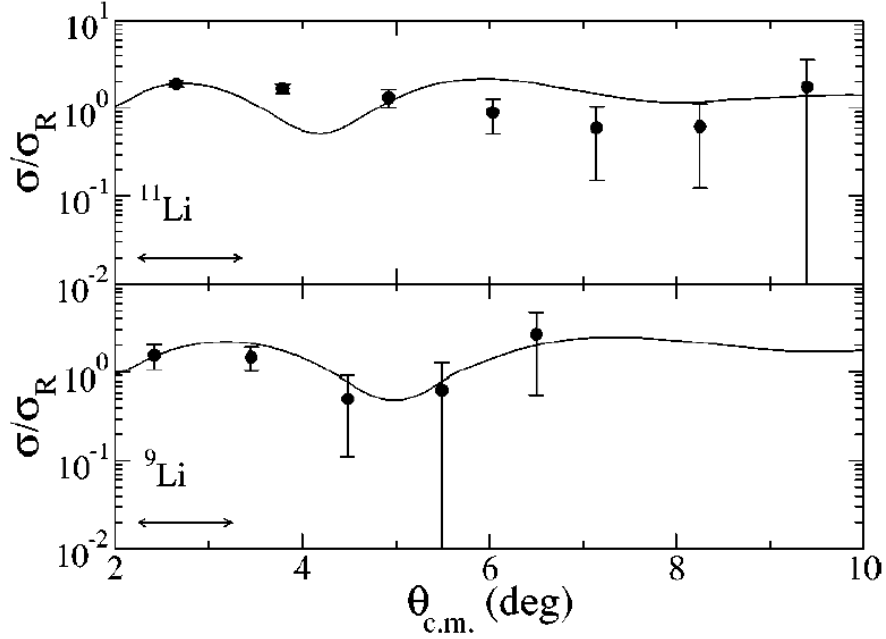


**Figure 43.** Elastic  $^{11}\text{Li}+^{12}\text{C}$  angular distribution measured at 50 MeV/nucleon [134] compared to the Glauber-model calculation folded with the experimental resolution. Illustration taken from Ref. [134].

to the weakly bound nature of  $^{11}\text{Li}$ . To solve this puzzle, a new experiment on the elastic scattering of  $^{9,11}\text{Li}$  from the  $^{12}\text{C}$  target at energy around 50 MeV/nucleon has been performed recently by Peterson *et al.* [134] using the S800 spectrograph at MSU. The improved energy resolution in this experiment was sufficient to exclude the inelastic contributions to the scattering at the forward angles, and the measured elastic  $^{11}\text{Li}+^{12}\text{C}$  cross section shows again no evidence of a nearside/farside interference minimum (see upper part of Fig. 43). Therefore, the interference minimum is either missing or greatly attenuated in this case. Since the deep interference minimum predicted for the  $^{11}\text{Li}+^{12}\text{C}$  system (see dashed curve in upper part of Fig. 42) is associated with the Fraunhofer crossover  $\bar{\Theta}$  (see discussion in Sec. 2), the spacing between this minimum and the nearest maximum should be  $\Delta\Theta_{\text{c.m.}} \simeq 2^\circ$ . However, after averaging over the angular bin, one could obtain only two data points within such  $\Delta\Theta_{\text{c.m.}}$  spacing (see Fig. 43) and it is likely that the interference minimum is so narrow and highly attenuated that could not be determined from the present experiment [134]. It is interesting to note that this interference minimum is still present in the results of the Glauber-model calculation even after the calculated cross section was folded with the experimental angular resolution (see upper part of Fig. 43). Given a strong refractive effect predicted [130] for the elastic  $^{11}\text{Li}$  scattering from Carbon target at energy around 30 MeV/nucleon (see, e.g, Fig. 13 in Ref. [130]), it is highly desirable to have further high-precision measurement for the elastic  $^{11}\text{Li}+^{12}\text{C}$  scattering at 30 - 50 MeV/nucleon, which would not only give a final

answer to this intriguing question but also provide valuable scattering data to further probe the  $2n$ -halo wave function of  $^{11}\text{Li}$ .

We finally note that the refractive pattern predicted by us [130] for the elastic  $^8\text{He}$  scattering around 30 MeV/nucleon has been confirmed in the elastic  $^8\text{He}+^4\text{He}$  scattering data measured at 26 MeV/nucleon by Wolski *et al.* [135], where one observed a broad shoulder-like maximum of the elastic cross section at large angles which is dominated by the farside scattering. These data are, however, not complete and lack the small-angle diffractive part which makes an accurate OM or folding model analysis difficult. It is obvious that more experiments for the elastic scattering of light unstable nuclei, such as the  $\alpha$ -clustered projectiles or unstable p-shell nuclei, are strongly needed to reveal further features of the nuclear rainbow which can then be used to probe their exotic structures in the OM analysis.

## 9. Summary

We have presented an overview of the nuclear rainbow, a fascinating phenomenon observed in the elastic  $\alpha$ - and light HI scattering at medium energies which can well be understood based on the basic concepts of the optical model description of the elastic scattering. Despite the striking similarity in the interference structure between the nuclear rainbow and atmospheric rainbow, the former has proven to be much harder to observe experimentally. It is important to stress that the occurrence of the rainbow pattern in the  $\alpha$ -nucleus and light HI elastic scattering is due to a *strong* mean field caused by the two nuclei overlapping each other. The attractive strength of the nucleon mean field (or nucleon OP) is much weaker and the rainbow pattern is, therefore, never observed in the nucleon-nucleus scattering. Moreover, the following three main physical conditions must be met for a clear nuclear rainbow to be observed.

First, the real optical potential must be strongly attractive to cause the refractive scattering. Such a deep nucleus-nucleus OP has been shown to be due to a strong mean-field attraction at small dinuclear distances or at high overlap densities. Second, the absorption in the nucleus-nucleus system must be weak (which is the case for the tightly bound  $\alpha$ -particle or for some light p-shell nuclei), so that the farside trajectories (passing through small distances or high overlap densities) can survive in the elastic scattering channel. Third, the incident energy should be high enough for these farside trajectories to appear in the elastic scattering cross section at medium and large scattering angles. Note that if the energy is too low, the scattering is dominated by the diffractive Fraunhofer pattern in the whole observable angular range, with the primary rainbow shifted into the unphysical angular region beyond  $\Theta_{\text{c.m.}} = 180^\circ$ . However, if the energy is too high, the refractive part moves to the forward angles and mixes with the diffractive part of the elastic cross section and the rainbow features become difficult to extract.

The semiclassical decomposition of the observed angular distributions into the nearside and farside (or barrier-wave and internal-wave) contributions has proven to be an important and powerful tool to understand the interference structure of the

nuclear rainbow. The same technique also allows us to probe the nucleus-nucleus OP at different interaction distances based on the observed scattering pattern. In particular, the nearside/farside interference at forward angles give information about the OP at the surface. At larger angles, only the farside scattering survives which gives rise to the Airy oscillation pattern of the nuclear rainbow. Since the Airy structure is caused by the nucleus-nucleus interaction at small distances, the rainbow scattering data of high accuracy can be used to determine the nucleus-nucleus OP (and the associated potential family) with much less ambiguity.

Given a weak absorption associated with the rainbow pattern in the elastic  $\alpha$ -nucleus and nucleus-nucleus scattering, the rainbow scattering data can be used to probe the density dependence of the in-medium NN interaction based on the folding model analysis of the elastic scattering. Most of the elastic rainbow scattering data were found to be best described by a *deep* real OP given by the double-folding calculation using a density dependent M3Y interaction which gives a nuclear incompressibility  $K \approx 230 - 260$  MeV in the HF calculation of nuclear matter. This result confirms a rather soft EOS for symmetric nuclear matter and the deduced  $K$ -value agrees very well with that of the latest nuclear structure studies of the isoscalar giant monopole resonances in medium-mass nuclei.

The refractive rainbow-like structures were also observed in other quasi-elastic scattering reactions, as well as in the elastic scattering measured with the loosely bound or unstable nuclei. However, more experiments on the quasi-elastic scattering induced by the light unstable nuclei are needed to learn more on the fascinating features of the nuclear rainbow, which can be used to probe the wave functions of these unstable isotopes.

## Acknowledgments

The authors are indebted to many colleagues for their helpful discussions and correspondences on this interesting topic during the last two decades. In particular, D.T.K. is grateful to Ray Satchler for his numerous discussions during the years of collaboration which have shed light on many issues discussed in this topical review. A clarifying comment by Gianluca Colò on the nuclear structure studies of the giant monopole resonance is also appreciated. The present research has been supported, in part, by the Alexander-von-Humboldt Stiftung of Germany, Hahn-Meitner-Institut Berlin, the German Ministry of Research and Technology BMFT under the contract 06OB472D/4, Vietnam Natural Science Council and Vietnam Atomic Energy Commission (VAEC). S.O. has been supported by the Japan Society for Promotion of Science (JSPS) and the Yukawa Institute for Theoretical Physics.

## References

- [1] Greenler R 1980 *Rainbows, Halos and Glories* (Cambridge: Cambridge University Press).

- [2] Nussenzweig H M 1977 *Scientific American* **236** 116
- [3] Adam J A 2002 *Phys. Rep.* **356** 229; *Notices of the AMS* **49** 1360.
- [4] Brandan M E, Hussein M S, McVoy K W and Satchler G R 1996 *Comments Nucl. Part. Phys.* **22** 77.
- [5] Brandan M E and Satchler G R 1997 *Phys. Rep.* **285** 143
- [6] Airy G B 1838 *Trans. Camb. Phil. Soc.* **6** 379.
- [7] von Oertzen W, Khoa D T, Bohlen H G 2000 *Europhysicsnews* **31** 5; von Oertzen W, Bohlen H G, V. Subotin and Khoa D T 2002 *Acta Physica Polonica B* **33** 93.
- [8] Goldberg D A and Smith S M 1972 *Phys. Rev. Lett.* **29** 500.
- [9] Goldberg D A, Smith S M, Pugh H G, Roos P G and Wall N S 1973 *Phys. Rev.* **C7** 1938.
- [10] Goldberg D A, Smith S M and Burdzik G F 1974 *Phys. Rev.* **C10** 1362.
- [11] Stokstad R G, Wieland R M, Satchler G R, Fulmer C B, Hensley D C, Raman S, Rickertsen L D, Snell A H and Stelson P H 1976 *Phys. Rev.* **C20** 655.
- [12] Bohlen H G, Clover M R, Ingold G, Lettau H and von Oertzen W 1982 *Z. Phys.* **A308** 121.
- [13] Bohlen H G, Chen X S, Cramer J G, Fröbrich P, Gebauer B, Lettau H, Miczaika A, von Oertzen W, Ulrich R and Wilpert T 1985 *Z. Phys.* **A322** 241.
- [14] Stiliaris E, Bohlen H G, Fröbrich P, Gebauer B, Kolbert D, von Oertzen W, Wilpert M and Wilpert T 1989 *Phys. Lett.* **B223** 291.
- [15] Bohlen H G, Stiliaris E, Gebauer B, von Oertzen W, Wilpert M, Wilpert T, Ostrowski A, Khoa D T, Demyanova A S and Ogloblin A A 1993, *Z. Phys.* **A346** 189.
- [16] Bartnitzky G, Blazevic A, Bohlen H G, Casandjian J M, Chartier M, Clement H, Gebauer B, Gillibert A, Kirchner T, Khoa D T, Lepine-Szily A, Mittig W, von Oertzen W, Ostrowski A N, Roussel-Chomaz P, Siegler J, Wilpert M and Wilpert T 1996 *Phys. Lett.* **B365** 23.
- [17] DeVries R M, Goldberg D A, Watson J W, Zisman M S and Clover J G 1977 *Phys. Rev. Lett.* **39** 450.
- [18] Broglia R and Winther A 1991 *Heavy Ion Reactions* (Lecture notes, Addison Wiley Publ. Comp.).
- [19] Roussel P *et al* 1987 *Phys. Lett.* **B185** 29.
- [20] Roussel P, Alamanos N, Auger F, Barrette J, Berthier B, Fernandez B, Papineau L, Doubre H and Mittig W 1988 *Nucl. Phys.* **A477** 345.
- [21] Satchler G R and Love W G 1979 *Phys. Rep.* **55** 183.
- [22] Satchler G R 1983 *Direct Nuclear Reactions* (Oxford: Oxford University Press).
- [23] Kondo Y, Michel F and Reidemeister G 1990 *Phys. Lett.* **B242** 340.
- [24] Khoa D T, von Oertzen W, Bohlen H G and Nuoffer F 2000 *Nucl. Phys.* **A672** 387.
- [25] Satchler G R 1983 *Nucl. Phys.* **A409** 3c.
- [26] Fuller R C 1975 *Phys. Rev.* **C12** 1561.
- [27] Anni R, Connor J N L and Noli C 2002 *Phys. Rev.* **C66** 044610.
- [28] McVoy K W and Satchler G R 1984 *Nucl. Phys.* **A417** 157.
- [29] Sugiyama Y, Tomita Y, Ikezoe H, Yamanouchi Y, Ideno K, Hamada S, Sugimitsu T, Hijiya M and Kondō Y 1993 *Phys. Lett.* **B312** 35.
- [30] Kondō Y, Sugiyama Y, Tomita Y, Yamanouchi Y, Ikezoe H, Ideno K, Hamada S, Sugimitsu T, Hijiya M and Fujita H 1996 *Phys. Lett.* **B365** 17.
- [31] McVoy K W and Brandan M E 1992 *Nucl. Phys.* **A542** 295.
- [32] Hussein M S and McVoy K W 1984 *Prog. Part. Nucl. Phys.* **12** 103.
- [33] Michel F, Brau F, Reidemeister G and Ohkubo S 2000 *Phys. Rev. Lett.* **85** 1823; Michel F, Reidemeister G and Ohkubo S 2001 *Phys. Rev.* **C63** 034620.
- [34] Brink D M and Takigawa N 1977 *Nucl. Phys.* **A279** 159.
- [35] Michel F and Ohkubo S 2004 *Eur. Phys. J.* **A19** 333.
- [36] Nicoli M P, Haas F, Freeman R M, Aissaoui N, Beck C, Elanique A, Nouicer R, Morsad A, Szilner S, Basrak Z, Brandan M E and Satchler G R 1999 *Phys. Rev.* **C60** 064608.
- [37] Nuoffer F *et al.* 1998 *Il Nuovo Cimento* **111A** 971; Nuoffer F 1999 *PhD Thesis* (University of Tübingen).

- [38] von Oertzen W, Bohlen H G, Khoa D T 2003 *Nucl. Phys.* **A722** 202c.
- [39] Put L W and Paans A M J 1977 *Nucl. Phys.* **A291** 93.
- [40] Batty C J, Friedman E, Gils H J and Rebel H 1989 *Adv. Nucl. Phys.* **19** 1.
- [41] Ogloblin A A, Khoa D T, Kondō Y, Glukhov Yu A, Dem'yanova A S, Rozhkov M V, Satchler G R and Goncharov S A 1998 *Phys. Rev.* **C57** 1797.
- [42] Ogloblin A A, Glukhov Yu A, Trzaska W H, Dem'yanova A S, Goncharov S A, Julin R, Khlebnikov S V, Muttterer M, Rozhkov M V, Rudakov V P, Tiorin G P, Khoa D T and Satchler G R 2000 *Phys. Rev.* **C62** 044601.
- [43] Szilner S, Nicoli M P, Basrak Z, Freeman R M, Haas F, Morsad A Brandan M E and Satchler G R 2001 *Phys. Rev.* **C64** 064614.
- [44] Szilner S, von Oertzen W, Basrak Z, Haas F and Milin M 2002 *Eur. Phys. J.* **A13** 273.
- [45] Micek S, Majka Z, Rebel H, Gils H J and Klewe-Nebenius H 1985 *Nucl. Phys.* **A435** 621.
- [46] Nadasen A, Stevens T, Farhat J, Brusoe J, Schwandt P, Winfield J S, Yoo G, Anantaraman N, Becchetti F D, Brown J, Hotz B, Janecke J W, Roberts D and Warner R E 1993 *Phys. Rev.* **C47** 674 and references therein.
- [47] Nadasen A, Brusoe J, Farhat J, Stevens T, Williams J, Nieman L, Winfield J S, Warner R E, Becchetti F D, Janecke J W, Annakkage T, Bajema J, Roberts D and Govinden H S 1995 *Phys. Rev.* **C52** 1894.
- [48] Satchler G R, Fulmer C B, Auble R L, Ball J B, Bertrand F E, Erb K A, Gross E E and Hensley D C 1983 *Phys. Lett.* **B128** 147.
- [49] Sakuragi Y, Yahiro M and Kamimura M 1986 *Prog. Theor. Phys. Suppl.* **89** 136.
- [50] Khoa D T, Satchler G R and von Oertzen W 1995 *Phys. Rev.* **C51** 2069.
- [51] Mahaux C and Sartor R 1991 *Adv. Nucl. Phys.* **20** 1 and references therein.
- [52] Jeukenne J P, Lejeune A and Mahaux C 1977 *Phys. Rev.* **C16** 80.
- [53] Brieda F A and Rook J R 1977 *Nucl. Phys.* **A291** 299; *ibid.* 317.
- [54] Feshbach H 1992 *Theoretical Nuclear Physics* Volume II (Wiley-Interscience: New York).
- [55] Khoa D T and Satchler G R 2000 *Nucl. Phys.* **A668** 3.
- [56] Khoa D T, von Oertzen W and Bohlen H G 1994 *Phys. Rev.* **C49** 1652.
- [57] Khoa D T, von Oertzen W, Bohlen H G, Bartnitzky G, Clement H, Sugiyama Y, Gebauer B, Ostrowski A N, Wilpert T, Wilpert M and Langner C 1995 *Phys. Rev. Lett.* **74** 34.
- [58] Khoa D T, Satchler G R and von Oertzen W 1997 *Phys. Rev.* **C56** 954.
- [59] Satchler G R and Khoa D T 1997 *Phys. Rev.* **C55** 285.
- [60] Brandan M E and McVoy K W 1997 *Phys. Rev.* **C55** 1362.
- [61] Love W G 1978 *Nucl. Phys.* **A312** 160.
- [62] Sinha B 1975 *Phys. Rep.* **20** 1.
- [63] Chaudhuri A K, Basu D N and Sinha B 1985 *Nucl. Phys.* **A439** 415; Chaudhuri A K and Sinha B 1986 *Nucl. Phys.* **A455** 169.
- [64] Khoa D T 1988 *Nucl. Phys.* **A484** 376.
- [65] Campi X and Bouyssy A 1978 *Phys. Lett.* **B73** 263.
- [66] Khoa D T 2001 *Phys. Rev.* **C63** 034007.
- [67] Love W G and Owen L W 1975 *Nucl. Phys.* **A239** 74.
- [68] Hagino K, Takehi T and Takigawa N 2006 *Phys. Rev.* **C74** 037601.
- [69] Trache L, Azhari A, Clark H L, Gagliardi C A, Lui Y W, Mukhamedzhanov A M, Tribble R E and Carstoiu F 2000 *Phys. Rev.* **C61** 024612.
- [70] Chamon L C, Pereira D, Hussein M S, Ribeiro M A C and Galetti D 1997 *Phys. Rev. Lett.* **79** 5218.
- [71] Chamon L C, Carlson B V, Gasques L R, Pereira D, De Conti C, Alvarez M A G, Hussein M S, Ribeiro M A C, Rossi Jr E S and Silva C P 2002 *Phys. Rev.* **C66** 014610.
- [72] Perey F and Buck B 1962 *Nucl. Phys.* **32** 353.
- [73] Buck B, Friedrich H and Wheatley C 1977 *Nucl. Phys.* **A275** 246.
- [74] LeMere M and Tang Y C 1979 *Phys. Rev.* **C19** 391; LeMere M, Stubeda D J, Horiuchi H and



- Tang Y C 1979 *Nucl. Phys.* **A320** 449.
- [75] Horiuchi H 1991 *Nucl. Phys.* **A522** 257c; Horiuchi H 1991 in *Trends in Theoretical Physics* (Eds. Ellis P J and Tang Y C; Addison-Wesley, New York).
- [76] Trefz M, Faessler A and Dickhoff W H 1985 *Nucl. Phys.* **A443** 499; Ohtsuka N *et al* 1987 *Nucl. Phys.* **A465** 550 and references therein.
- [77] Khoa D T, Faessler A and Ohtsuka N 1990 *J. Phys.* **G16** 1253.
- [78] Gils H J 1987 *Nucl. Phys.* **A473** 111.
- [79] Atzrott U, Mohr P, Abele H, Hillenmayer C and Staudt G 1996 *Phys. Rev.* **C53** 1336.
- [80] Kondō Y, Brandan M E and Satchler G R 1998 *Nucl. Phys.* **A637** 175.
- [81] Ohkubo S and Yamashita K 2002 *Phys. Rev.* **C66** 021301(R).
- [82] Soubbotin V B, von Oertzen W, Vinas X, Gridnev K A and Bohlen H G 2001 *Phys. Rev.* **C64** 014601.
- [83] Mütter H 1986 *Prog. Part. Nucl. Phys.* **17** 97; Brockmann R and Machleidt R 1984 *Phys. Lett.* **B149** 283.
- [84] Bertsch G, Borysowicz J, McManus H and Love W G 1977 *Nucl. Phys.* **A284** 399.
- [85] Anantaraman N, Toki H and Bertsch G 1983 *Nucl. Phys.* **A398** 269.
- [86] Kobos A M, Brown B A, Hodgson P E, Satchler G R and Budzanowski A 1982 *Nucl. Phys.* **A384** 65.
- [87] Kobos A M, Brown B A, Lindsay R and Satchler G R 1984 *Nucl. Phys.* **A425** 205.
- [88] Brandan M E and Satchler G R 1988 *Nucl. Phys.* **A487** 477.
- [89] Khoa D T and von Oertzen W 1993 *Phys. Lett.* **B304** 8.
- [90] Fetter A L and Walecka J D 2003 *Quantum Theory of Many-Particle Systems* (Dover: Dover Publications, Inc.).
- [91] Khoa D T and von Oertzen W 1995 *Phys. Lett.* **B342** 6.
- [92] Bethe H A 1971 *Ann. Rev. Nucl. Sci.* **21** 93; Myers W D 1973 *Nucl. Phys.* **A204** 465.
- [93] Baron E D, Cooperstein J and Kahana S 1985 *Phys. Rev. Lett.* **55** 126; *Nucl. Phys.* **A440** 744.
- [94] Swesty F D, Lattimer J M and Myra E S 1994 *Astrophys. J.* **425** 195.
- [95] Glendenning N K 2000 *Compact Stars: Nuclear Physics, Particle Physics and General Relativity* (Springer: Springer-Verlag New York, Inc.).
- [96] Schutz Y and TAPS Collaboration 1996 *Nucl. Phys.* **A599** 97c.
- [97] Sick I, McCarthy J S and Whitney R R 1976 *Phys. Lett.* **B64** 33.
- [98] Gils H J, Friedman E, Rebel H, Buschmann J, Zagromski S, Klewe-Nebenius H, Neumann B, Pesl P and Bechtold G 1980 *Phys. Rev.* **C12** 1239.
- [99] Furumoto T and Sakuragi Y 2006 *Phys. Rev.* **C74** 034606.
- [100] Youngblood D H, Lui Y W, Clark H L, John B, Tokimoto Y and Chen X 2004 *Phys. Rev.* **C69** 034315.
- [101] Colò G and Van Giai N 2004 *Nucl. Phys.* **A731** 15c.
- [102] Blaizot J P 1980 *Phys. Rep.* **64** 171.
- [103] Vretenar D, Nikšić T and Ring P 2003 *Phys. Rev.* **C68** 024310.
- [104] Piekarewicz J 2002 *Phys. Rev.* **C66** 034305.
- [105] Agrawal B K, Shlomo S and Au V K 2003 *Phys. Rev.* **C68** 031304(R).
- [106] Colò G, Van Giai N, Meyer J, Bennaceur K, Bonche P 2004 *Phys. Rev.* **C70** 024307.
- [107] Satchler G R 1989 *Nucl. Phys.* **A505** 103.
- [108] Bohlen H G, Khoa D T, von Oertzen W, Gebauer B, Nuoffer F, Bartnitzky G, Blazevic A, Mittag W and Roussel-Chomaz P 2002 *Nucl. Phys.* **A703** 573.
- [109] Khoa D T, Bohlen H G, von Oertzen W, Bartnitzky G, Blazevic A, Nuoffer F, Gebauer B, Mittag W and Roussel-Chomaz P 2005 *Nucl. Phys.* **A759** 3.
- [110] Khoa D T and Knyazkov O M 1987 *Z. Phys.* **A328** 67.
- [111] Michel F and Ohkubo S 2004 *Phys. Rev.* **C70** 044609.
- [112] Michel F and Ohkubo S 2004 *Nucl. Phys.* **A738** 231.
- [113] Tohsaki A, Horiuchi H, Schuck P and Röpke G 2001 *Phys. Rev. Lett.* **87** 192501.

- [114] Kokalova Tz, Itagaki N, von Oertzen W and Wheldon C 2006 *Phys. Rev. Lett.* **96** 192502.
- [115] Ohkubo S and Hirabayashi Y 2004 *Phys. Rev.* **C70** 041602(R).
- [116] Demiyanova A C, Bragin V N, Ogloblin A A, Lebedev A L, Bang J M, Goncharov S A, Ershov S N, Gareev F A and Korovin P P 1987 *Phys. Lett.* **184** 129.
- [117] Burjan V, Cejpek J, Fojtu J, Kroha V, Pecina I, Mukhamedzhanov A M and Timofejuk N K 1994 *Phys. Rev.* **C49** 977.
- [118] Burtebaev N, Duisebaev A and Sakuta S B 2003 *Yadern. Fizika* **66** 51.
- [119] Michel F and Ohkubo S 2005 *Phys. Rev.* **C72** 054601.
- [120] Carstoiu F, Trache L, Tribble R E and Gagliardi C A 2004 *Phys. Rev.* **C70** 054610.
- [121] Milin M, Cherubini S, Davinson T, Di Pietro A, Figuera P, Miljanić D, Musumarra A, Ninane A, Ostrowski A N, Pellegriti M G, Shotter A C, Soić N, Spitaleri C and Zadro M 2004 *Nucl. Phys.* **A730** 285.
- [122] Lapoux V, Alamanos N, Auger F, Fékou-Youmbi V, Gillibert A, Marie F, Ottini-Hustache S, Sida J L, Khoa D T, Blumenfeld Y, Maréchal F, Scarpaci J-A, Suomijärvi T, Kelley J H, Casandjian J M, Chartier M, Cortina-Gil M D, Mac Cormick M, Mittag W, de Oliveira Santos F, Ostrowski A N, Roussel-Chomaz P, Kemper K W, Orr N and Winfield J S 2002 *Phys. Rev.* **C66** 034608.
- [123] Satchler G R, McVoy K W and Hussein M S 1991 *Nucl. Phys.* **A522** 621.
- [124] Yabana K, Ogawa Y and Suzuki Y 1992 *Phys. Rev.* **C45** 2909; *Nucl. Phys.* **A539** 295.
- [125] Kolata J J, Zahar M, Smith R, Lamkin K, Belbot M, Tighe R, Sherrill B M, Orr N A, Winfield J S, Winger J A, Yennello S J, Satchler G R and Wuosmaa A H 1992 *Phys. Rev. Lett.* **69** 2631.
- [126] Mermaz M C 1993 *Phys. Rev.* **C47** 2213.
- [127] Khoa D T, Satchler G R and von Oertzen W 1995 *Phys. Lett.* **B358** 14.
- [128] Cooper S G and Mackintosh R S 1995 *Nucl. Phys.* **A582** 283.
- [129] Carstoiu F and Lassaut M 1996 *Nucl. Phys.* **A597** 269.
- [130] Khoa D T, von Oertzen W and Ogloblin A A 1996 *Nucl. Phys.* **A602** 98.
- [131] Thompson I J, Al-Khalili J S, Tostevin J A and Bang J M 1993 *Phys. Rev.* **C47** R1364.
- [132] Al-Khalili J S 1995 *Nucl. Phys.* **A581** 315; Al-Khalili J S, Thompson I J and Tostevin J A 1995 *Nucl. Phys.* **A581** 331.
- [133] Hussein M S and Satchler G R 1994 *Nucl. Phys.* **A567** 165; Satchler G R and Hussein M S 1994 *Phys. Rev.* **C49** 3350.
- [134] Peterson D, Kolata J J, Santi P, von Schwarzenberg J, Bazin D and Sherrill B M 2003 *Phys. Rev.* **C67** 014601.
- [135] Wolski R, Sidorchuk S I, Ter-Akopian G M, Fomichev A S, Rodin A M, Stepantsov S V, Mittag W, Roussel-Chomaz P, Savajols H, Alamanos N, Auger F, Lapoux V, Raabe R, Tchuvil'sky Yu M and Rusek K 2002 *Nucl. Phys.* **A722** 55c.